1-1-2016

Design of an American Football Helmet Liner for Concussion Mitigation

Gustavus Alston Rush

Design of an American football helmet liner for concussion mitigation

By

Gustavus Alston Rush

A Dissertation
Submitted to the Faculty of
Mississippi State University
in Partial Fulfillment of the Requirements
for the Degree of Doctor of Philosophy
in Biomedical Engineering
in the Department of Agricultural and Biological Engineering

Mississippi State, Mississippi

August 2016

Design of an American football helmet liner for concussion mitigation

By

Gustavus Alston Rush

Approved:

_____

Lakiesha N. Williams
(Major Professor)

_____

Mark F. Horstemeyer
(Co-Major Professor)

_____

Rajkumar Prabhu
(Committee Member)

_____

Hongjoo Rhee
(Committee Member)

_____

Robert K. Collins
(Committee Member)

_____

Steven H. Elder
(Graduate Coordinator)

_____

Jason M. Keith
Dean
Bagley College of Engineering

Name: Gustavus Alston Rush

Date of Degree: August 12, 2016

Institution: Mississippi State University

Major Field: Biomedical Engineering

Major Professor: Dr. Lakiesha Williams

Title of Study: Design of an American football helmet liner for concussion mitigation

Pages in Study 179

Candidate for Degree of Doctor of Philosophy

The objective of this research was to develop an optimal design for a polymeric American football helmet liner for concussion prevention utilizing experiments and high performance. Along with well-established injury criteria (HIC, SI, and Peak acceleration), localized brain injury mechanisms were explored by employing Finite Element simulations and experimental validation. Varying strain rate experiments (monotonic and hysteresis) were conducted on modern football helmet (Rush, Rawlings, Riddell, Schutt, and Xenith) liners and new possible polymeric foam liner materials. These experiments were used to characterize each material at low strain rates (0.1/sec; Instron), intermediate strain rates (100-120/sec; NOCSAE drop tower) and high strain rates (600-1000/sec; Split Hopkinson Pressure Bar). Experimental design optimization was performed on a football helmet liner by utilizing an exploratory Design of Experiments by National Operating Committee on Standards for Athletic Equipment (NOCSAE) drop tests. FEA simulations of drop impact tests were conducted on a helmeted NOCSAE headform model and a helmeted human head model. Correlations were made between both models to relate localized brain response to the global acceleration and the dynamic-based injury criteria HIC, SI, and Peak acceleration). FEA

simulations were experimentally validated by twin-wire drop tests of the NOCSAE headform using correlations for validation of the human head model. The helmeted human head simulations were used to explore a Mild Traumatic Brain Injury (MTBI) limits based localized brain response (e.g. pressure and impulse). Based on these limits, future FEA simulations will be used to explore these limits as helmet liner design criteria.

DEDICATION

I dedicate this work to my wife, Jena, who stood by me and made countless sacrifices to make this possible.

ACKNOWLEDGEMENTS

I would like to acknowledge Rush Sports Medical of Meridian, Mississippi for their monetary support and the Center for Advanced Vehicular Systems (CAVS) at Mississippi State University for providing testing facilities. I thank my father, Dr. Sonny Rush for guiding and providing me through life and this research.

My most sincere gratitude goes to my advisors Dr. Lakiesha Williams and Dr. Mark Horstemeyer for the gift of their time and guidance through the course of this research. I appreciate the guidance of Dr. Raj Prahbu in life and in the fields of Finite Element Analysis and mechanical testing. I thank Dr. Hongjoo Rhee for providing me knowledge and insight into polymeric materials and a view of the macroscale applications. I would like to thank Dr. Robert Collins for providing me on-field insight into head injury during collegiate football.

I appreciate the help and support from the graduate students, faculty, and staff at CAVS. I appreciate the help of Stevin Horstemeyer, Robert Malley, for helping me build and maintain the NOCSAE drop tower. Mrs. Melissa Mott taught me how to become an expert in quasi-static material testing. I owe great appreciation to Dr. Ric Carino, who has helped me in many ways including the development of a MATLAB program for drop tower data analysis.

I would like to thank the entire Injury Biomechanics Division at the U.S. Army Aeromedical Research Lab (USAARL) for providing me an excellent learning

opportunity during my fellowship. Joe McEntire, Fred Brozoski, and Dr. Carol Chancey gave me expert mentorship and enhanced experimental skill set.

My special thanks goes out to Lindley Bark who has served as an excellent friend and mentor in the arena of practical engineering applications and testing methodologies amongst other things.

TABLE OF CONTENTS

LIST OF TABLES

LIST OF FIGURES

CHAPTER I

INTRODUCTION AND BACKGROUND

1.1 Intellectual Merit

The scientific contribution of this research was to develop a design process for a polymeric foam helmet liner utilizing a systems approach and correlating the localized brain response to dynamic head injury metrics by employing experimentally validated Finite Element Analysis (FEA) simulations. This research will increase the knowledge of mild traumatic brain injury predictors and the effectiveness of helmet testing standards. Varying strain rate effects will also be taken into account using high-rate (600-1000/sec), intermediate rate (100-120/sec) and low rate (0.1 /s) mechanical testing. In future studies, a strain-rate dependent injury metric should be created based on predicted (local) brain damage and correlated to (global) dynamic response. This future injury metric, being non-biased, may bring cohesion to the biomedical community, in respect to historical brain injury metrics. This research will also aid in expanding the definition of concussion by the development of quantitative probabilistic concussive thresholds.

1.2 Broader Impacts

This research will provide a much needed advancement in helmet design for reducing the occurrence of Mild Traumatic Brain Injury. Current helmet designs are based upon linear acceleration injury tolerances that were derived from cadaveric skull fracture tests over 50 years ago. It has been well established that these injury tolerances

and resulting helmet designs need advancement. This study specifically aims for the development of an American football helmet liner. While there is ample of room for advancement of protective headgear, physical limitations are acknowledged, thus the proposed study is part of a three-step long-term process to effectively eliminate MTBI and its cumulative effects. This process includes; 1) advanced protective headgear, 2) accurate impact exposure quantification (inertial measurement devices), and 3) knowledge of and obedience to impact exposure limits (thresholds). The present work will contribute to this long-term vison by employing innovative technology, novel design methodology, and the use of Finite Element Analysis for the development of advanced protective headgear.

1.3 Motivation

Sport related brain injuries have been estimated to occur 1.6 to 3.8 million times every year, in the United States [1]. Football players can receive up to 1500 head impacts per season [2, 3]. Although every impact may not result in a concussion, numerous impacts can result in long-term brain damage through an impact induced neurodegenerative disease known as chronic traumatic encephalopathy (CTE) [4]. CTE is linked to a buildup of tau protein in the brain, leading to memory loss, behavior and personality change, Parkinsonism, and speech and gait abnormalities that has sometimes led to suicide [5]. Recent publicity [5] of CTE in former professional football players has spurred many researchers to find ways to reduce concussion and increase player safety.

Historically helmet design and test standards have been based on fundamental engineering concepts, such as energy absorption and impulse, and not on the biomechanics of head injury. We believe the lack of significant advancement in helmet

technology is due to adherence to old test methods, disagreement of injury metrics in the biomedical community and slow implementation of technology such as computer based predictive modeling. While technologies and materials have been available for the development of a safer football helmet, the expense of such may have also hindered helmet manufacturers from the creation of meaningful helmet innovations.

1.4 Football Helmet History

American football began around 1890 but it wasn't until the 1920's that players started using protective head gear [6]. These primitive football helmets, commonly known was "leatherheads", were made of leather with no facial protection. The first suspension helmets emerged in 1940. The US government used the design for the GI helmet during World War II [7]. The suspension straps were within the hard plastic shell, which offered impact absorption but little comfort. Padded suspension systems began to emerge but were only used for a short time due to the advent of better helmet pads. The current padded helmet system finally evolved. These systems work by absorbing impact energy through compression. Foam pads were first used, which were then modified by the addition of air or water reservoirs. The evolution of football helmets and liner system types is portrayed in Figure 1.1.

Figure 1.1 History of the American Football helmet showing the evolution of helmet liner systems, shells, and facemasks [6].

In football today, there are a variety of padded systems in use. For the context of this work, padded helmet systems are characterized as either a foam-based liner or an engineered chamber. The majority of football helmets have used foam-based liner systems with pads typically consisting of closed cell flexible polymeric foam [8]. There has recently been some success in non-foam football helmet systems that rely on engineered chambers to mitigate impact. The Schutt ION 4D and the Xenith X2 helmets are some examples that use of these engineered chamber systems. A variety of padded systems are explored for this research. Modern football helmet shells are normally made from polycarbonate plastic. The modern football helmet "control group" used in this

study are the Rawlings Quantum Plus, Riddell 360, Schutt Ion 4D, and Xenith X2 helmets since they are widely used and represent some of the newest innovations in football helmet technology on the market. The existing novel football helmet to be used for optimization in this study is a helmet design developed by Rush Sport Medical (Meridian, MS). This helmet is unique from other football helmets since its design incorporates a composite shell with an integrated flush-profile facemask and an open cell polymeric foam based liner.

1.5 Head Injury Metrics

Early head injury research focused on external observations of head impacts and trying to relate these observations to the severity of the resulting brain injury. Beginning in the 1940's, several attempts were made to relate external loading to brain injury, Gurdjian, Webster, and Lissner at Wayne State University conducted in vivo animal studies on canines. These early animal studies consisted of head impact tests and air blast test to the exposed brain. Rudimentary brain damage correlations were made for impact magnitude and blast pressure. In 1949, Lissner et al. began cadaveric skull fracture tests in attempt to find brain injury limits [9, 10]. In these tests, cadavers were dropped down an elevator shaft onto their heads at different heights until a skull fracture was produced [11]. Rough brain damage probabilities were made based on the assumption that if there was a skull fracture then there was also a concussion.

Data from these cadaveric tests led Lissner et al. (1960) to the development of the first known tolerance criterion known as the Wayne State Tolerance Curve (WSTC) [12-14]. The Wayne State Tolerance Curve (WSTC) was developed to predict skull fracture for automotive crashes during a frontal impact by defining a threshold curve boundary for

linear acceleration versus impact duration [13-15]. The WSTC defines a linear impulse-based human tolerance to injury, given in terms of average head acceleration versus impact duration. Patrick et al. (1965) modified this curve by the addition of animal and human volunteer sub-concussive data [15]. The modified WSTC curve, as shown in Figure 1.2, portrays that any exposure above the curve is dangerous and that a human head can withstand higher accelerations for shorter impact durations.

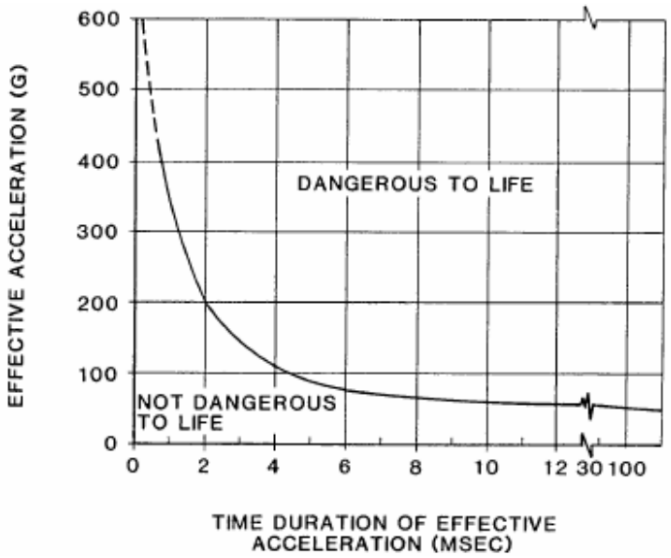

Figure 1.2 Wayne State Tolerance Curve for the human brain in forehead impacts against plane, unyielding surfaces [13, 15].

The Wayne State Tolerance Curve has been used to develop many of the head injury metrics still in use today. When plotted logarithmically, the WSTC becomes a straight line with a slope of -2.5. With this observation, Gadd et al. (1966) used a logarithmic scale to linearly fit the WSTC with a 2.5 power-weighing factor and

proposed an injury criterion known as the Gadd Severity Index, more commonly known as the Severity Index (SI) [16]. The SI is based on the following equation,

$$SI = \int_0^T a(t)^{2.5}\, dt \tag{1.1}$$

where *a(t)* is the translational acceleration (G's) of the Center of Gravity (CG) of the head, and *T* is the acceleration duration (seconds) [18, 12]. A severe injury will result if the Severity Index exceeds a value of 1000 [16, 17]. The Severity Index was limited to an acceleration pulse with similar shape and duration to what was used in the Wayne State University cadaveric tests [18]. More specifically, the Severity Index was found to be unsuitable for longer duration, lower acceleration impacts nor impacts with complex acceleration pulses [19, 20]. Versace et al. (1971) proposed a modified version of the Severity Index, known as the Head Injury Criterion (HIC), in order to accommodate more complex acceleration pulses [18, 19]. The Head Injury Criterion identifies the most damaging part of the acceleration pulse by taking maximum value of the following equation,

$$HIC = \left[(t_2 - t_1)\left\{\frac{1}{(t_2 - t_1)}\int_{t_1}^{t_2} a(t)dt\right\}^{2.5}\right]_{max} \tag{1.2}$$

where *a(t)* is the translational acceleration (G's) of the CG of the head, and t_1 and t_2 are the initial and final times (seconds), respectively, of the interval at which HIC attains a maximum value [19]. It is common for the pulse duration of the HIC calculation to be limited to 15 or 36 milliseconds, known as HIC_{15} or HIC_{36}, respectively [21]. A severe but not life threatening injury would occur if HIC exceeds a value of 1000. HIC and SI are both weighted impulse criterion with units of s $G^{2.5}$ which are typically omitted and expressed unitless numbers [22].

While the development of the WSTC has been some of the most impactful research in regards to current brain injury criterion, it has also led to much controversy. This controversy arises from the facts that the WSTC was developed to predict skull fracture for automotive crashes (non-helmeted) during a frontal impact by defining a threshold curve boundary for linear acceleration versus impact duration [13-15]. The WSTC is specifically limited to severe brain injury; it is based on the onset of skull fracture, rather than brain injury. The WSTC is also based on only frontal impacts, defined by linear acceleration, many researchers suggests that impact location and angular acceleration are both key factors in determining concussion [23].

While HIC and SI are based upon linear (translational) acceleration, there is another school of thought that angular acceleration can cause severe brain injury. In 1971 Ommaya published rotational head injury risk data from primate tests during whiplash [24-27]. Using scaled data from these chimpanzee tests, Ommaya proposed a concussive angular acceleration threshold in man to be 1800 rad/s^2. Lowenhielm (1974) proposed a limit for angular acceleration of 4500 rad/s^2 based on a mathematical viscoelastic model [28].

Other studies suggest that impact location is a key factor in evaluating susceptibility to head injury. Many researchers have hypothesized on which impact location would be the most susceptible to a concussion but the answer remains controversial. Early studies of concussion have involved animal and cadaveric experiments. In 1983, Hodgson suggested that lateral impacts were the most likely to lead to a concussion [29]. By impact tests on primates at front, side, rear and top locations, it was observed that higher linear and angular accelerations produced longer

periods of unconsciousness (more than 3 times) on the side than other locations. Hodgson hypothesized that this decrease in concussion tolerance may be the result of lower mechanical impedance due to the oval shape of the head (geometry effect). More recently, real time studies have been conducted in an attempt for on-field inertial measurement of head injury. Several other studies have suggested that a lower impact tolerance for lateral translational impacts as compared to anterior-posterior and axial impacts [23]. Delaney et al. (2014) determined that the side/temporal region of the head was the most common area to be struck resulting in a concussion in university football, ice hockey and soccer [30]. Some researchers [31, 32] have shown that the brain is more susceptible to sustain a concussion due to top of the head impacts during football. Mihalik et al. [31] found that four of seven recorded concussion cases were impacts that occurred to the top of the head. Similarly, Guskiewicz et al. [32] found that six out of thirteen concussion cases were due to impacts at the top location. In contrast, other researchers [23, 33-36] have shown the front of the head as being more susceptible to concussion. Greenwald et al. [23] recorded seventeen concussion cases of which eight were frontal impacts, five were to the sides, three were to the top, and one was to the back of the helmet. Broglio et al. [33] found that eight of thirteen concussion cases occurred due to impacts to the front of the helmet. Pellman et al. [35, 37] recorded twenty-five concussion cases, fourteen of which involved impacts to the frontal facemask region of the helmet. Rowson et al. [36] recorded thirty-three out of fifty-seven concussion cases occurred by impacts at the front and rear of the helmet. However, Rowson showed the highest number of concussion cases per impact was found for impacts to the top of the head.

Probability methods have been proposed as metrics for determining concussive thresholds using various injury criteria. In 1985, Prasad and Mertz proposed a probability method of assessing head injury for HIC, whereas a HIC of 1000 would result in approximately 16% of the population to sustain a serve injury [12]. Rowson and Duma (2011) proposed a probabilistic football helmet rating criteria, known as the Virginia Tech Summation of Tests for the Analysis of Risk (STAR) rating system. The STAR system rates a helmets performance by a theoretical calculation of a probabilistic analysis of impact exposure based on an impacts location and injury risk [38, 39]. The STAR system applies a weighted fraction to an impact location based on probability.

Newman et al. (2000) proposed the Head Impact Power index (HIP), an injury criterion that would account for angular acceleration as well as linear acceleration [40]. The development of this criterion was derived from indirect measures of head acceleration via laboratory tests with Hybrid III anthropomorphic test dummies [23, 40].

1.5.1 Helmet Test Standards

Today's helmet testing standards either use an injury criterion based upon the Wayne State Tolerance Curve (namely HIC or SI) or use peak acceleration criterion, or in some cases both. While some modifications are in order to add angular acceleration to standard performance criterion, linear impulse criteria remain dominant.

The first helmet standards were developed by the British Standards Institute (BSI) in 1952 [41, 42] . This standard was developed to determine the energy dissipation capability for motorcycle racing helmets by means of rudimentary drop tests using a wooden headform. These drop tests specified measuring the force of a wood block dropped at a specific height upon of a helmeted headform. In this standard (BS

1869:1952) better helmets were simply determined to be those that produced the lowest force upon impact [11]. A 5000 N threshold was set for all helmets under the BSI standard. If the inertial loading of a 5kg free fall headform is considered, this failure criterion would be set at 400G's. In the United States, Snively and Chester (1962) pioneered the sports helmet test standards. In 1966 the American Standards Association (ASA) published the first American helmet standard. The test procedures were essentially those devised by Snively, which used a 400 G threshold, similar to the BSI 1952 standard, except a maximum time duration was set. At the time the WSTC had been proposed and already receiving criticism, thus the Severity Index was not set into the ASA standard. This standard used a rather non-anthropomorphic headform that was constructed of magnesium alloy [11].

Compared to the previous standards, football helmet standards took different approach by employing biofidelity and the Gadd Severity Index. In 1969 the National Operating Committee on Standards for Athletic Equipment (NOCSAE) was formed to develop performance standards for American football helmets as well as other sporting equipment [17]. Dr. Voigt Hodgson, of Wayne State University, tasked with the development of the NOCSAE test method [11]. Hodgson developed and implemented a biofidelic headform and employed the Severity Index as an injury criterion [43].

Various other helmet standards were developed and except for the adoption of HIC by the Economic Community of Europe (ECE) and the National Highway Traffic Safety Administration (NHTSA), the majority of the helmet standards still use the same injury criterion as originally devised. Global acceleration (Peak G) of the impacted head is typically used as impact severity measures [44]. NOCSAE is the only organization to

adopt the Severity Index, while NHTSA is the only organization to use HIC with a reasonable limit. The amount of disagreement in the biomedical community regarding injury metrics suggests to us that better non-biased injury metric is warranted.

1.5.2 Dissertation Structure

Chapter I describes the motivation and background of this thesis. The work disclosed here expands motivation, brain injury mechanisms, brain injury metrics, protective headgear, and helmet tests standards. Chapter II provides structure property quantification of an open-cell polyurethane foam with background into the mechanics of foams. A literature review is first presented on polymer foams showing general mechanisms of energy absorption. Concepts of open-cell polymeric foam energy absorption is proposed and explained. Structure-property quantification of liner mater materials is presented at varying strain rates.

Chapter III presents an investigation of the energy dissipation characteristics of football helmets and football helmet liners. The implications of these results are presented with a novel helmet liner design criteria. Chapter IV establishes baseline dynamic responses for four current helmet systems and explores advancing helmet test standards to include the facemask. In Chapter V, an experimental design optimization was performed on a novel football helmet liner for concussion prevention. A Design of Experiments was performed via NOCSAE drop tests utilizing peak acceleration, HIC, and SI as design criterion. Chapter VI investigates the dynamics response of the NOCSAE headform versus a human head during football helmet standard impact tests. Here, experimentally validated Finite Element simulations are conducted to create a

linkage between helmet test standards, brain injury metrics, and the mechanical response of the human brain.

Finally, Chapter VII summarizes the results of this work and Chapter VIII provides recommendations for future work with special considerations for continuation of head injury protection and concussion limits.

The goals of this work were to:

1. Study energy dissipation characteristics of football helmet liners.
2. Perform experimental design optimization on a football helmet liner.
3. To perform Finite Element Analysis of NOCSAE headform and human head models.

CHAPTER II

STRUCTURE-PROPERTY QUANTIFICATION OF AN OPEN-CELL POLYURETHANE FOAM

2.1 Introduction

The purpose of this chapter is to evaluate structure-property quantification of an open-cell polyurethane (PU) foam for use as an energy absorbing helmet liner. In this study, the baseline foam for analysis is an open-celled polyurethane foam used in the Rush Football helmet. This foam was selected was based unpublished work by Zimmerman et al. (2006). Drop tower impact tests of over 50 foams, each differing in material, cellular structure and/or density, showed the baseline foam to have to lowest peak acceleration and Head Injury Criterion (HIC) values. In the present study, an amalgamation of a literature review and experimental methods was employed to examine the relationship of this foam's structure and mechanical properties. Implications of performance for football helmet liner applications are briefly discussed, however, the performance characteristics are the focus of Chapter III. Physical properties of flexible polyurethane foams depend on the cellular structure and the solid polymer comprising the struts of the foam. In this study, the cellular structure of a viscoelastic foam is quantified by image analysis using optical and scanning electron microscopy methods while the uniaxial compressive response to loading of the material is analyzed by high strain-rate (Hopkinson bar) and low strain-rate (Instron) mechanical testing devices.

2.1.1 Open-Cell and Closed-Cell Foams

Closed-cell foam is a type of foam that consists of multitude of individual non-interconnecting, gas-tight cells [45]. These cells resemble inflated balloons or soccer balls, piled together in a compact configuration. Closed-cell foam is typically rigid because the pressure inside the cells and bending of solid material making up the cell walls both resist deformation during an applied load. Pressure inside the cells are primarily responsible for the load-bearing capability of closed-cell foam, similarly to the inflated tires that hold up an automobile. The elastomer content of closed-cell foam is predominantly Polyvinyl Chloride (PVC) or its copolymers [46]. Closed-cell foam is typically characteristic of high resilience due to intercellular air-pressure increase during an impact event, allowing a high rebound coefficient.

Open-cell foam is one that consist of interconnecting cells in which air can flow between cells [45]. The structure of open-cell foam creates a three-dimensional interconnected lattice supported by struts in the cell walls. There are two types of open-cell foam: reticulated foam, and slow-recovery foam, both differing in the degree of cell openness and inherently the recovery time [45]. Manufacturing of reticulated foam entails exploding a gas-air mixture to remove the face and leave only the cell struts [47]. Reticulated foam has a very high degree of cell openness and has a very high resilience or fast recovery after compression. This is because upon compression and unloading air is allowed to escape and infiltrate the cell with little or no resistance by the cell opening allowing the solid material in the cell struts to quickly rebound the foam to its original shape. Slow-recovery foam is a flexible open-cell polyurethane foam with cellular anisotropy characterized by its low degree of cell openness and its slow recovery, or low

resilience, after compression [45, 48]. Upon compression viscous dissipation occurs by frictional forces between the escaping air and the relatively small cell opening compared to the size of the cell. Upon unloading, the same frictional forces slow the cell struts from quickly rebounding to the foams original shape, negating its resilience. This viscous dissipation results in a higher hysteresis (energy loss) for slow-recovery foam compared to a similar reticulated foam. Normally, slow-recovery foam shows anisotropy, having elongated ellipsoidal cells in the foaming direction. Figure 2.1 comprises the Scanning Electron Microscopy (SEM) images showing the cellular structure for closed-cell foam (Figure 2.1a), reticulated open-cell foam (Figure 2.1b), and viscoelastic open-cell foam (Figure 2.1c).

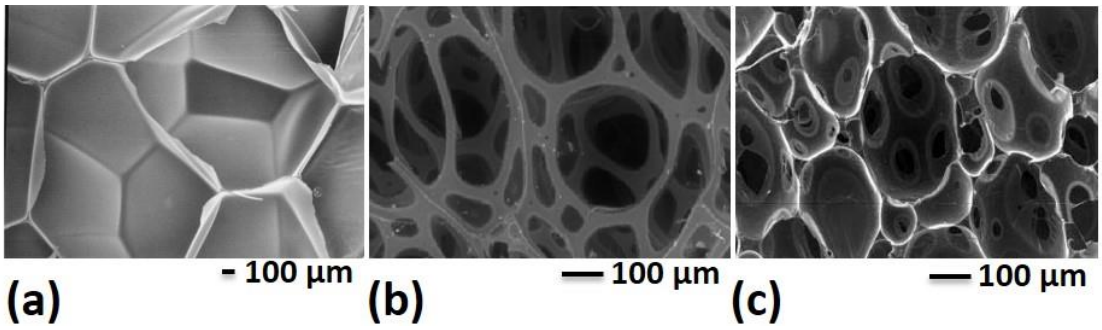

Figure 2.1 Scanning Electron Microscopy (SEM) images of (a) a closed-cell foam, (b) an open-celled reticulated foam, (c) and open-cell viscoelastic foam [48].

The baseline liner material for this research is a viscoelastic (slow recovery open-cell) polyether-based polyurethane foam, SunMate Firm manufactured by Dynamic Systems (Leicester, NC, USA) [49-51]. This foam is produced from a slab stock process where the foam components are mixed, placed in a container and allowed to rise vertically. This process typically produces foam with anisotropic cells, having elongated

cells in the rise direction and near circular cell faces in the transverse direction. In this study, viscous dissipation was analyzed in the baseline foam by quantifying the features that affect air-flow. These features include the size of the cells, the orientation of the cells, and number and spacing of the holes in the cell faces [48]. The mechanical response of an open-cell foam is dependent on the cellular structure and solid state polymer morphology of the foam, which are both a function of temperature and humidity [52]. The effects of temperature and humidity were not quantified and are considered outside the scope of the present study. We hypothesize that this open-cell foam can be an excellent candidate for a football helmet liner, if it can be optimized with an increase in resilience while maintaining its energy absorption capabilities.

2.1.2 Polyurethane Foam Chemistry

Polyurethane foams are the most versatile of foams, having a number of forms and uses. Polyurethane is considered a crystalline polymer. Polyurethane foam is available in two types; polyether and polyester [53]. Polyurethane foams can be produced by slab, bonding, and molding processes [46]. The cellular structure of polyurethane foams can either be open-cell, closed-cell or semi-open cell. This research specifically focuses on the analysis of a flexible polyurethane foam, which are typically open-cell. More specifically, this section will examine the chemistry of the baseline viscoelastic foam this is produced from a slab molding process.

Urethane foams are an expanded cellular product produced by the interaction of active hydrogen compounds, water and isocyanates. Polyurethanes are made by a step-growth addition reaction of a di-isocyanate and a diol which produces a urethane linkage but no by-products [48]. If a diol is used that is mixed with some triols this reaction

produces a rigid part of the PU molecule and a flexible part of the PU molecule, also known as hard-segments and soft-segments, respectively. The hard-segment of the PU molecule is produced from the R_1 group of the di-isocyanate, which is typically diphenylmethane. The soft-segment is produced from the R_2 group of the diol, which is typically a low molecular weight polyethylene oxide. The difference between making solid polyurethane and polyurethane foam is that gas has to be incorporated by a reaction of the isocyanate group with water (chemical blowing agent) forming an amine and CO_2 gas. Some urea-linkages will be produced in the polyurethane foam by reaction of the amine with other di-isocyanates. This urea is a by-product that is necessary to expand the polyurethane into a foam [54]. Polyurethane foams can be produced with a range of mechanical properties by varying the polyol and isocyanate components. The chemical reactions for polyurethane and polyurea are depicted in Figure 2.2.

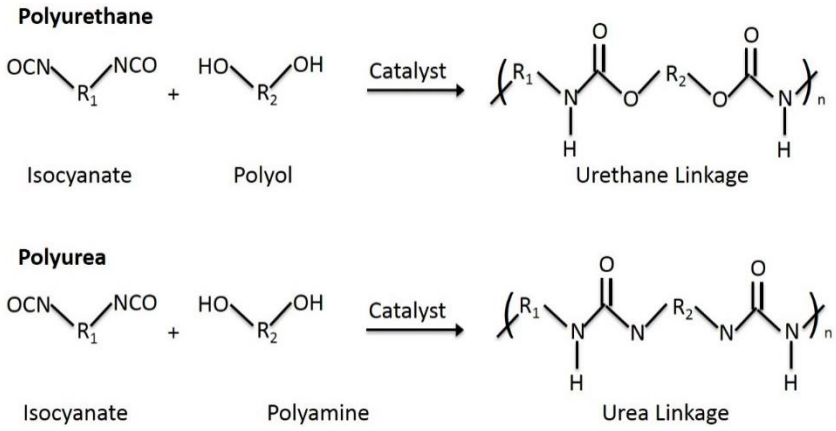

Figure 2.2 The chemical reactions of polyurethane and polyurea.

For polyurethane, the isocyanate and polyol reactants form the urethane linkage in this step-growth reaction. The polyamine is a by-product of the foaming and it reacts with the isocyanate to form polyurea [3, 6].

Physical blowing agents and a variety of additives are often used in production of polyurethane foam. Physical blowing agents are used to enhance the expansion of PU foam. These agents are typically volatile liquids, including liquid CO_2, chlorofluorocarbons, and Hydrochlorofluorocarbons, that evaporate and make the foam expand [54]. A variety of additives can be used to cosmetically enhance PU foam or improve performance. These additives include coloring, UV stabilizers, bacteriostats, flame retardants and reduction of static electrical charges. Other additives include non-reactive plasticizers to reduce viscosity, cell-openers to prevent shrinkage during the cooling process, compatibilizers to enhance the emulsification of the reactants [46].

2.1.3 Physical Properties of Foams

Various physical properties are used to characterize foam and their mechanical response; these properties are introduced in the following. One of these most commonly used physical properties for characterizing foam is the *relative density* (RD) defined as follows,

$$RD = (\rho^*/\rho_s) \tag{2.1}$$

where the density of the cellular material (ρ^*) is divided by the density of the solid material (ρ_s) that the cellular walls are made from. Relative densities for foams typically range from as low as 0.001 to 0.3. While some structural foams have relative densities above 0.4, they are not considered for our application as a helmet liner. This work specifically focuses on low densities foams, which have relative densities of less than 0.1. Relative density is related to *porosity* (ϕ) the fraction of pore space in the foam, by the following equation [45].

$$\phi = (1- \rho^*/\rho_s) \tag{2.2}$$

Poisson's ratio, the ratio of transverse strain to axial stain during uniaxial loading is another parameter that is necessary for characterization of foams that is often debated with respect to material modeling of foams. Many material models assume a zero Poisson's ratio for foam during compression while other material models account for Poisson's ratio of foam as an average over a range of strain. Widdle et al. [55] studied the effects of a zero Poisson's ratio assumption for use of flexible polyurethane foam in a hyperelastic model. They experimentally measured Poisson's ratio at high compression levels, ranging from 0.5 at 5% compressive strain to -0.05 at 66% compressive strain. This data and outsourced results were combined into a nonlinear viscoelastic model for uniaxial compression behavior, using a Taylor series. They find that the accuracy of the model decreases with an assumed zero Poisson's ratio [55]. In the present study, Poisson's ratio was measured as a single average over a range of strain.

Characterization of a foams mechanical response includes a few important differences as compared to that of other materials. While tensile tests are commonly used for characterization of other materials, they are rarely used for foams. This is partially due to the difficulty of gripping foam during tensile test, and because foams are rarely loaded in tension [48]. Engineering stress and strain are used to characterize a foam's response to loading while other materials are typically characterized using True stress and True strain. The reasons of this difference relate back to the low Poisson's ratio of foam.

2.1.4 The Mechanics of Foams: Compression

Most applications of foams cause them to be loaded in compression. Generally flexible polyurethane foam exhibits a nonlinear function of compressive strain, during quasi-static loading. Gibson et al. analyzes the stress-strain diagrams for elastomeric,

elastic-plastic and brittle foam and show that they have three characteristic regions characterized by different slopes as depicted in Figure 2.3. The typical stress-strain curve of these foams show a linear elastic region (Region I) followed by a plateau region (Region II) and then a densification region (Region III). The linear elastic region takes place at low strain levels ($0 < \varepsilon < 0.05$) and is controlled by elastic bending. For open cells, the linear elasticity is controlled by cell wall bending, and for closed cells it is controlled by cell face stretching. The plateau is a long region controlled by cell wall buckling and bubble collapse and is defined by intermediate deformations ($0.1 < \varepsilon < 0.6$). The densification region is where the opposing faces of the cells touch each other and further deformation of the foam requires solid phase deformation. This region is defined by the highest deformations ($\varepsilon > 0.6$) [45]. Increasing the relative density of the foam increases the slope of the linear elastic region (Young's Modulus), raises the plateau stress, and reduces the strain at which the densification region begins [54].

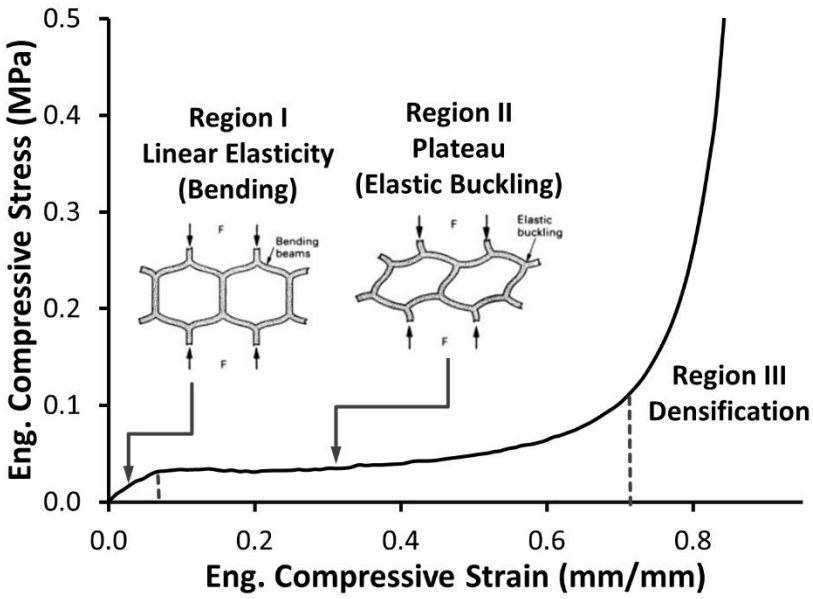

Figure 2.3 Typical compressive stress-strain curves for polymeric foam shows three regions each controlled by different mechanisms.

Note: Region I, the linear elastic region, is controlled by elastic bending of cell walls ($0 < \varepsilon < 0.05$). Region II, the plateau region, is controlled by cell wall buckling ($0.1 < \varepsilon < 0.6$).Region III, the densification region, is where the opposing faces of the cells touch each other and further deformation of the foam requires solid phase deformation ($\varepsilon > 0.6$) [45].

For polymeric foam the unload curve does not follow the load curve because stress not only depends on the actual strain level but also the strain history of the foam. A typical polymeric foam stress strain curve is shown in Figure 2.4. The solid line (loading curve) represents the materials response to an application of compressive load (loading curve), while the dashed line represents the material response when the load is reduced (unloading curve). The total area below the loading curve represents the specific energy absorbed by the material during loading (areas A plus B). The area below the unloading curve (area B) represents the materials rebound specific energy or the energy that is stored in the material by compressive loading and released upon unloading. Area A is the hysteresis which represents the amount of specific energy dissipated by the material.

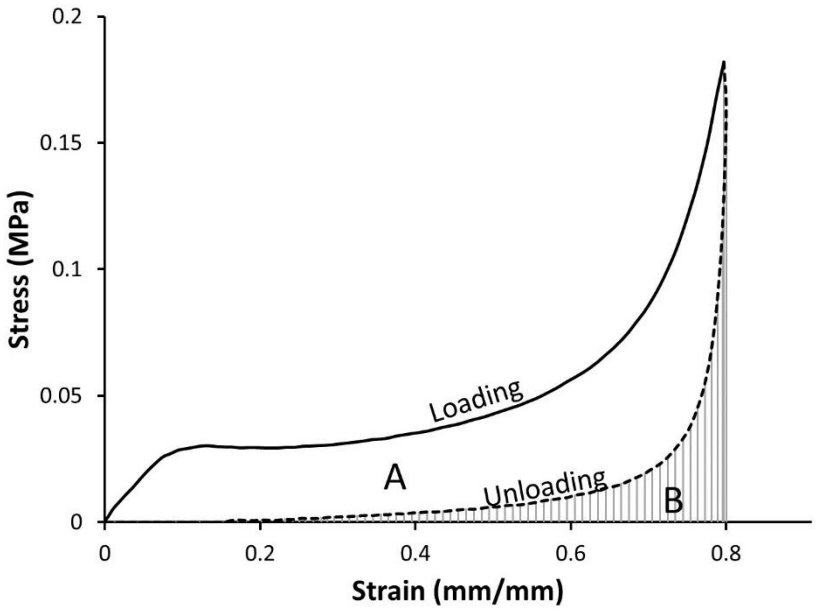

Figure 2.4 Typical response of polymeric foam to compressive loading and unloading showing hysteresis (area A), specific rebound energy (area B) and the specific energy absorbed by the material during loading (area A plus area B).

Zhu et al. [56] showed mesoscale structure property relationships for open-cell polyurethane foam. In this writing we focus on the macroscale structure-property relationships for open-cell polyurethane foam. In particular, we focus on global porosity effects on the stress-strain behavior at different strain-rates, the elastic moduli and hysteresis effects and energy absorption.

2.2 Methods

The structure of the baseline viscoelastic foam was analyzed by microscopy methods and compared to literature. Mechanical properties were obtained via high-rate (1200-600/s) and quasi-static (0.1-0.001/s) compression testing.

2.2.1 Optical Microscopy

Optical Microscopy (OM) was conducted at the Center for Advanced Vehicular Systems (CAVS) using a Zeiss Axiovert 200 optical microscope (Carl Zeiss Microscopy, Jena, Germany). Optical Microscopy was used to determine average cell size, distribution as well as to quantify anisotropy. Image J software was used for image analysis. Specimens were imaged in three directions; foam rise direction, transverse direction and orthogonal direction. Three specimens were measured per direction for a total of 9 imaged specimens. OM specimens were cut into their respective orientations by a guided blade system. A thin coat of Krylon Paint for Plastic was applied to the surface of the specimen to be imaged. Images were recorded at a magnification of 25x. Figure 2.5 depicts the painted Optical Microscopy specimens and their cellular orientations in the foam rise direction (Figure 2.5a), transverse direction (Figure 2.5b) and orthogonal direction (Figure 2.5c).

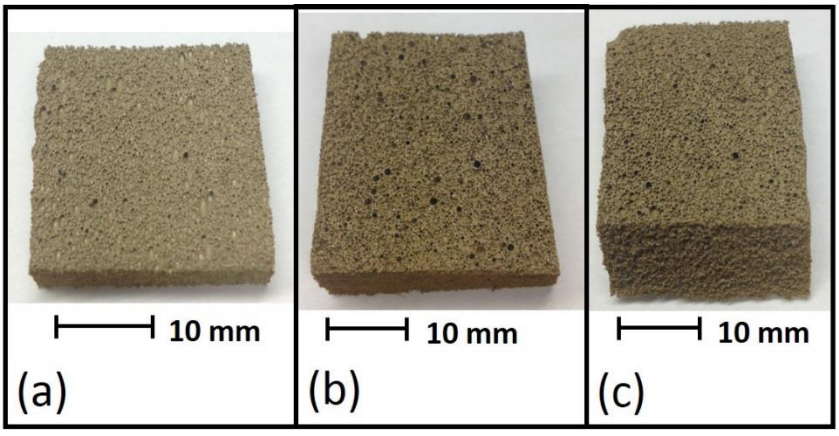

Figure 2.5 Painted Optical Microscopy specimens of SunMate Firm showing (a) foam rise direction, (b) transverse direction and (c) orthogonal direction sections.

2.2.2 Scanning Electron Microscopy

Scanning Electron Microscopy (SEM) was conducted at CAVS by use of a ZEISS EVO 50 environmental SEM (Carl Zeiss Microscopy, Jena, Germany). All foam specimen material was non-magnetic plastic, hence the samples were first sputter coated with a gold-palladium mixture. By inspection the sputter coat of all SEM foam samples appeared to be well distributed. Precautions were taken to prevent burns from the SEM in the non-metallic foam specimens. The SEM specimen geometry consisted of one inch cubes for quantification of anisotropy. SEM was used to examine cellular structure, and to quantify cell opening size and distributions.

2.2.3 Quasi-static Compression Testing

Figure 2.6 Quasi-static compression test set-up of the Instron 5869.

Quasi-static compression tests were conducted on an Instron 5869 (Instron Engineering Corporation, Norwood, MA, USA) equipped with a 25.4 mm extensometer and 2" diameter platens, as depicted in Figure 2.6. Materials were subjected to five consecutive series of cyclic compression up to 80% strain without time delay between cycles. Tests were conducted at strain-rates of 0.1, 0.01 and 0.001 per second on three samples per strain-rate. Recovery times were measured for each specimen during cyclic compression up to 80% strain at a strain-rate of 0.1 per second. These recovery times were recorded from the onset of unloading ($\varepsilon = 0.8$) to the time of full strain recovery ($\varepsilon = 0$). In order to get a bulk material response, cylindrical specimens were used for compression testing. Compressive foam specimens were cut by means of a drill press using a LENOX 18L 29 mm outer-diameter hole-saw bit. The specimens shape was a cylinder with dimensions of 25.4 mm, 25.4 mm (length, diameter).

2.2.4 High-rate Compression Testing

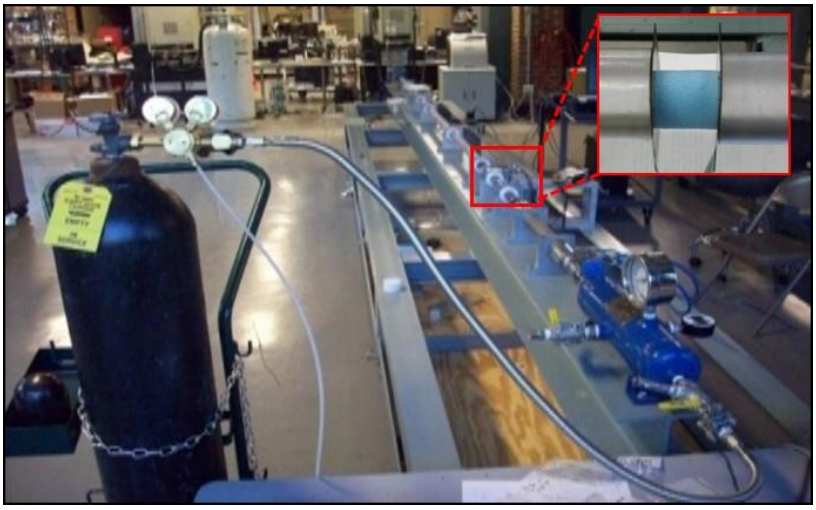

Figure 2.7 High-rate compression test set-up of Split Hopkinson Pressure Bar.

The 2" diameter polycarbonate Hopkinson Bar test device is shown with a zoomed region depicting the placement of the foam specimens.

High-rate compressive test were conducted using a Split Hopkinson Pressure Bar (Center for Advanced Vehicular Systems, Starkville, MS, USA) capable of producing strain-rates of 600-1200 per second, as depicted in Figure 2.7. The dynamic test set-up consisted of a 2 inch diameter polycarbonate bar equipped with strain gauges. Three samples were tested for each material at a strain-rate of 600 per second. Dynamic calibration entailed running a compressive test without the foam specimen and calibrating for the response of the material accordingly. Data was acquired using a Vishay Micro Measurements (Vishay Americas Inc., Wendell, NC, USA) Model Number 2310A Signal Conditioning Amplifier at a sample rate of 1MHz. Post processing employed a MATLAB routine for calculating stress and strain from the strain gauge results. High speed imaging was used to validate stress-strain data. High-rate data was filtered post testing using a Butterworth anti-alias filter by inputting a pseudo-sample frequency of 1000 Hz and a cutoff frequency at 10 Hz.

2.3 Results and Discussion

Results of the viscoelastic foams material properties are summarized in Table 2.1. Here, the compressive stress at 20 % strain ($\varepsilon = 0.2$) is given for a nominal strain-rate of 0.1 /s at 20° C. The compressive stress-strain curve is non-linear but this stress indicates the foam's relative compressive stiffness.

Table 2.1 General properties of SunMate foam showing density, relative density, stress at 20% compression (0.1/s), recovery time with standard deviation, and Poison's Ratio for SunMate Extra-Firm, Firm, Medium, and Soft foams.

Manufacturer	Brand Name	Symbol	Density (kg/m^3)	Relative Density	Stress at 20% comp. (kPa)	Recovery Time (Seconds)	Poison's Ratio (v)
Dynamic Systems	SunMate Extra-Firm	SM-XF	85.6	0.071	45.78	39.5 ± 4.5	-
	SunMate Firm	SM-F	84.3	0.070	33.50	31.2 ± 4.4	0.15
	SunMate Med-Firm	SM-MF	82.8	0.069	27.27	28.6 ± 2.6	-
	SunMate Medium	SM-M	79.9	0.067	17.15	21 ± 3.6	-
	SunMate Soft	SM-S	87.0	0.073	5.60	-	-

While the stress-strain curves for these foams are non-linear, the low strain-rate stress at 20% compression gives an idea of the materials stiffness. The recovery time provides a measure of resilience from 80% compression to full strain recovery ($\varepsilon = 0.8$ to $\varepsilon = 0$) at a strain-rate of 0.1/s.

2.3.1 Structure of an Open-Cell Polyurethane Foam

In cell structure of an open-cell polyurethane foam, a geometrical anisotropy has been observed in which the cells perpendicular to the rise direction appear circular, while the cells parallel appear elliptical. Figure 2.8 shows the anisotropy of SunMate Firm foam with ellipsoidal cells and example measurements as seen from SEM images. Figure 2.8a shows the geometry of the cells are an elliptical shape in the foam rise direction (indicated by the arrow). Figure 2.8b shows the circular geometry of the cells in the transverse direction. All other densities for this type of SunMate foam show similar anisotropy. This anisotropy has been shown to affect the bulk foam properties, such as load bearing. For optimal energy absorption these foams are recommended to be loaded in the rise direction.

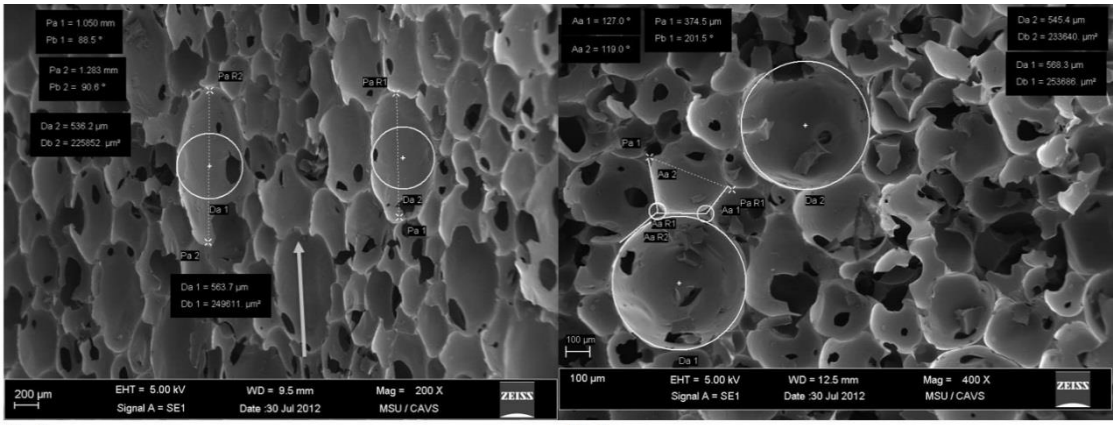

Figure 2.8 Scanning Electron Microscopy (SEM) images of SunMate Firm foam showing anisotropy with measurements of cell geometry.

(a) Ellipsoidal cells are in the foam rise direction as indicated by the arrow while (b) circular cells are in the transverse direction of the foam.

A very low degree of interconnecting cells was observed in SunMate Firm foam via microscopy, as depicted in Figure 2.9. SEM further verifies that SunMate firm is in fact a viscoelastic foam by the low degree of cell openness. This low degree of cell openness affects the foams resilience, or ability to return to form after a compressive impact. The low resilience, of this foam type is due to the restricted airflow by the limited degree of interconnected cells. Furthermore, this same mechanism makes viscoelastic materials very efficient in respect to impact energy absorption due to viscous dissipation of the air escaping foam.

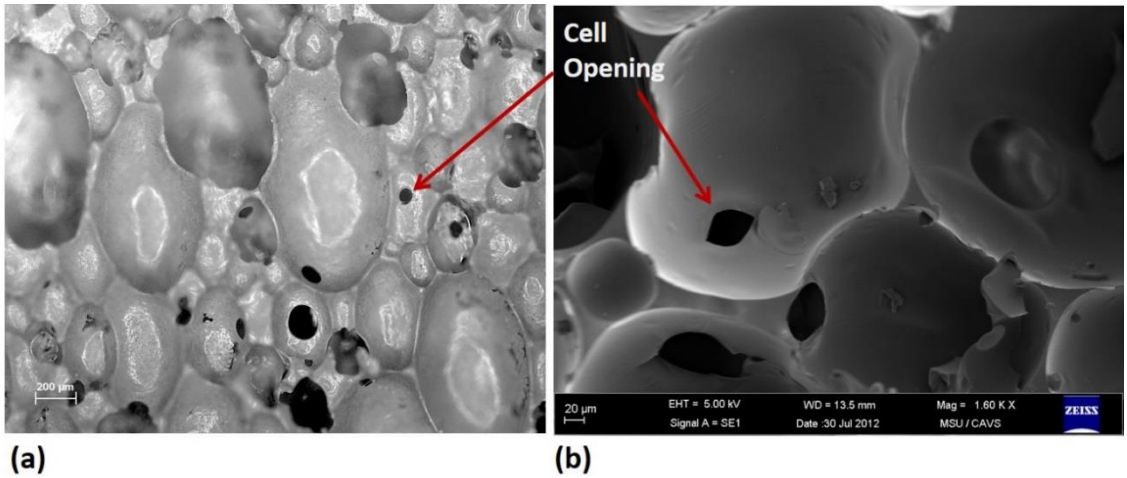

Figure 2.9 Microscopy images of SunMate foam showing degree of interconnecting cells and the cell opening as indicated by the arrows.

(a) Optical microscopy image of open-cell polyurethane foam in the cell rise direction and (b) scanning electron microscopy image of the same foam cut in the transverse direction.

The average cell diameter in SunMate Firm foam was calculated as 268.09±2.93 µm in the foam rise samples, 260.51±2.90 µm in the orthogonal foam samples, and 269.60±2.50 µm in the transverse foam samples. Microscopy results including this average cell diameter correlated well the microstructural analysis found in literature [47] for the same foam. Table 2.2 shows the cell and hole areas and diameters, the percentage of solid material, and a ratio of the hole and cell diameters for three different densities of SunMate foam. As one may assume, the cell area increases proportionally to the cell diameter, both of which are inversely proportional to the solid area fraction. For SunMate Firm and Medium foams, as the cell area and diameters increase, the hole area and hole diameters decrease. The SunMate Firm foam has larger cell areas and smaller hole areas than the Medium density foam. The cell diameter and hole area results of Table 2.2 were used for analysis of the air effects during compression. Fitzgerald et al. [47] studied the

effects of airflow in foams and shows a positive correlation between K and the mean face hole area for SunMate foams.

Table 2.2 Parameters from image analysis of microstructure entities of SunMate Firm, Medium, and Soft open-cell polyurethane foams [47].

	Cell Area (10^4 µm^2)	Cell Diameter (10^2 µm)	Hole Area (10^4 µm^2)	Hole Diameter (10^2 µm)	Solid Area (R_v)%	D_H/D_C
SunMate Firm[47]	7.3 ± 4.2	2.9 ± 0.9	0.085 ± 0.08	0.29 ± 0.15	1.1 ± 0.4	0.10
SunMate Medium[47]	6.8 ± 4.5	2.8 ± 1.0	0.15 ± 0.24	0.34 ± 0.27	1.7 ± 0.6	0.12
SunMate Soft[47]	8.9 ± 16.3	2.9 ± 1.8	0.34 ± 0.69	0.51 ± 0.0041	1.7 ± 0.7	0.18
SunMate Firm (Exp.)	5.64 ± 2.3	2.68 ± 0.5	-	-	1.7 ± 0.3	-

2.3.2 Compressive Stress-strain response of an Open-Cell Polyurethane Foam

The compressive stress-strain response of an open-cell polyurethane foam shows non-linearity with three characteristic regions in its curve profile (Figure 2.10), which is consistent with literature for this material type. Region I shows linear elasticity due to bending of cell walls up to a strain of about 0.5. Region II, also known as the plateau, shows elastic buckling of the cell walls up to a strain 0.6-0.7. Region III is defined as the densification region, initiating at strains of 0.6 to 0.7 until full compression. As shown in Figure 2.10, the SunMate foam shows an increase in plateau stress and an earlier onset of the densification region with an increase in relative density of the foam.

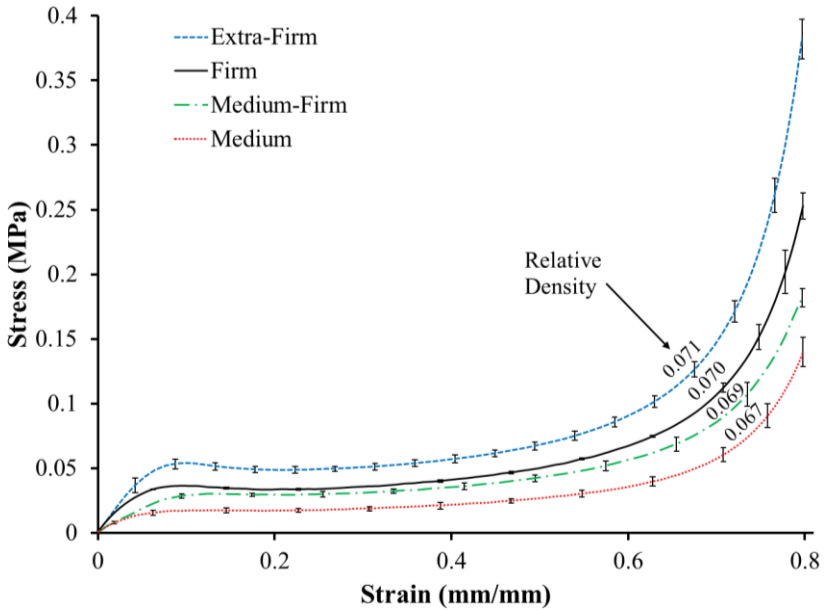

Figure 2.10 Stress-strain response of SunMate open-cell polyurethane foam at varying densities during quasi-static compression at a strain-rate of 0.1/s.

Note: An increase in plateau stress and an earlier onset of the densification region is seen an increase in relative density.

2.3.3 The Effect of Strain History on an Open-Celled Foam

The mechanical response of open-cell polyurethane foam is dependent on its strain history. When subject to five consecutive cycles of quasi-static compression, slow-recovery foams show low resilience and high dependence on strain-history. Some examples of this strain-history dependence are portrayed in Figure 2.11 when SM-XF (Figure 2.11a), SM-F (Figure 2.11b), SM-MF (Figure 2.11c), and SM-M (Figure 2.11d) foams are cyclically loaded and unloaded with five consecutive cycles. Here, the area below the loading curve represents the amount specific energy absorbed by the material during application of load while the area between the load and unload curves represent the amount of energy dissipated in each cycle. For each foam in Figure 2.11, the energy absorption and energy dissipation decrease with each cycle due to the lack of full strain

recovery between intervals. Figure 2.12 further illustrates the effect of strain-history due to cyclic loading on these foams. Here, the magnitudes of specific energy dissipated per load-unload cycle (Figure 2.12a) and specific energy absorbed per cycle are quantified and compared. SM-XF foam shows the highest energy absorption and energy dissipation for each cycle. For SM-XF, SM-F, SM-MF, and SM-M foams, the largest difference in energy absorption is seen between cycles 1 and 2 with fractional differences between cycles 3 through 5. In Figure 2.12, it is observed that the energy dissipated by SM-XF foam was greater than the energy absorbed by SM-F foam. Similarly, the energy dissipated by SM-F foam was greater than the energy absorbed by the SM-M foam.

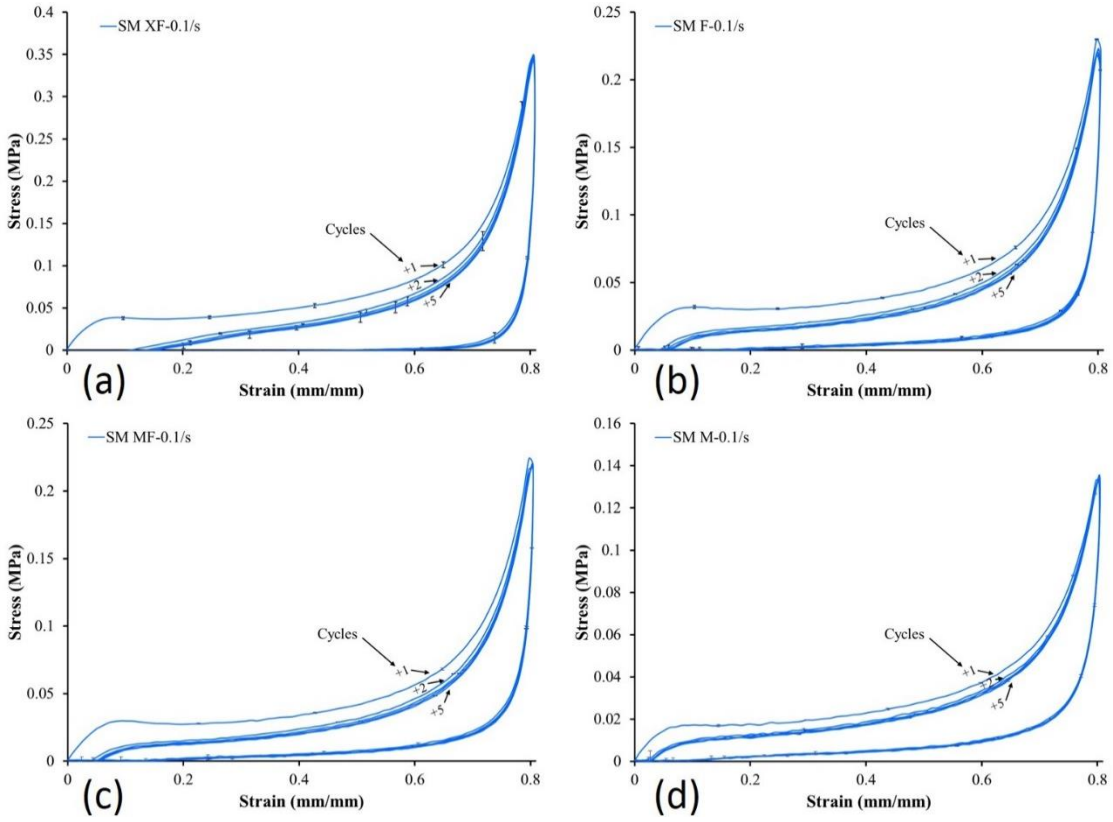

Figure 2.11 The stress-strain response of SunMate Extra-Firm (a), Firm (b), Medium-Firm (c), and Medium (d) open-cell polyurethane foams under cyclic loading shows a strain-history dependence.

Note: Quasi-static compression tests were conducted at a strain-rate of 0.1 /s with five consecutive load-unload cycles. Stress-strain results for SM-XF (a) and SM-M (d) are depicted on different scales than SM-F (b), and SM-MF (c) foams.

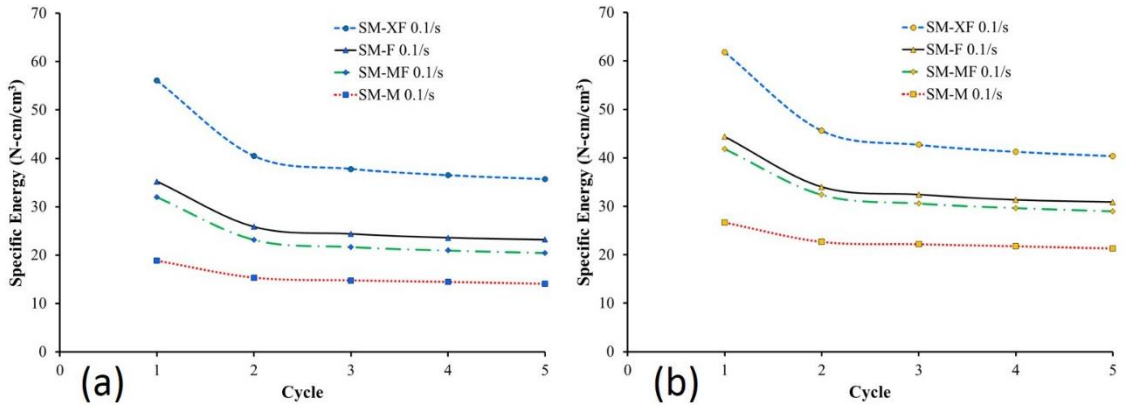

Figure 2.12 Specific energy versus load-unload cycle for SM-XF, SM-F, SM-MF, and SM-M open-cell polyurethane foams showing (a) Specific energy dissipated (hysteresis) per cycle of compression and (b) specific energy absorbed per cycle of compression.

Note: Quasi-static compression tests were conducted at a strain-rate of 0.1 /s with five consecutive load-unload cycles.

2.3.4 The Effect of Strain-rate on an Open-Cell Polyurethane Foam

Varying strain-rate compression tests for SunMate polyurethane foam shows strain-rate dependence with an increase in the increase in stress for higher strain-rates. An example of this strain-rate dependence is shown in Figure 2.13 for the baseline foam, SunMate Firm. Here, the stresses for the linear elastic region, plateau region, and densification region increase with increasing strain-rate. A shortening in the plateau region and an earlier onset of the densification region is also seen with an increase in strain-rate.

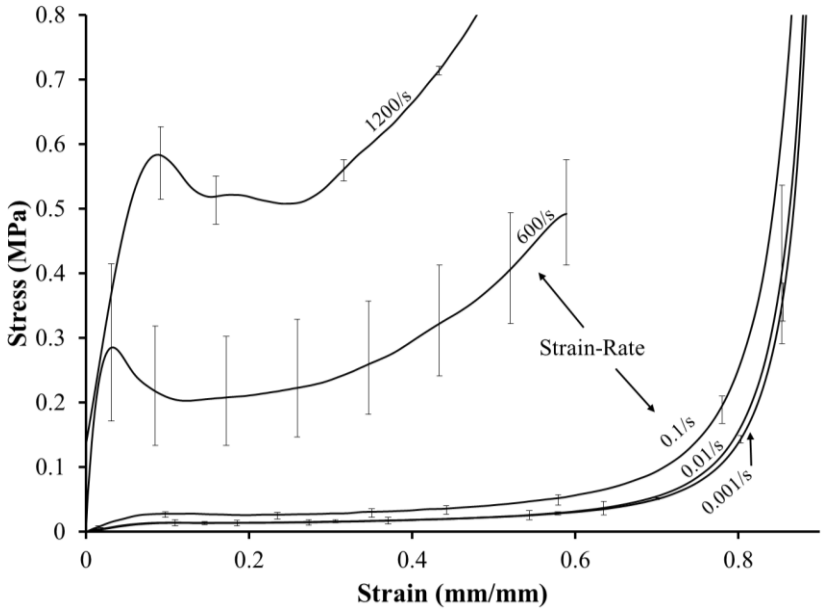

Figure 2.13 Strain-rate dependence of the baseline polyurethane foam, SunMate Firm (relative density = 0.07).

Note: The stress-strain curves at strain rates 0.001, 0.01, 0.1, 600, and 1200/s show an increase in stress with increasing strain-rate.

The strain-rate dependence for this particular foam was quantified in Figure 2.14. Here, three points of stress along the stress-strain curve are plotted on a log-log curve of strain-rate for quasi-static strain-rate (0.001, 0.01, and 0.1/s) and high strain-rate (600 and 1200/s) compressive tests. Each of these stress points correspond to a region in the typical compressive stress-strain curve for a polymeric foam (Refer to Figure 2.3). Strain levels of $\varepsilon = 0.05$ correspond the linear elastic region, $\varepsilon = 0.3$ corresponds to the plateau region, and $\varepsilon = 0.6$ corresponds to the onset of the densification region. The results for each of these stress points plotted on a log-log curve were best fit with a power function, as shown in Figure 2.14. The closest fitting group was $\varepsilon = 0.05$ with an exponent of 0.27, having an R^2 value closest to unity. The most important of these three points may be the plateau stress ($\varepsilon = 0.3$) since it is used as an energy absorbing design criterion for where

an upper stress limit (crush stress) can be set [45, 48]. The stresses at strains of ε = 0.6 showed a comparatively higher slope for the high strain-rate tests. This is indicative of an earlier onset of the densification region for the higher strain rates which is typically seen in polymeric foams. It should be noted that the strain-rate range for football helmet applications is approximately 50/s to 200/s, which lies between the strain-rate ranges for the quasi-static Instron and high-rate Hopkinson bar test devices. While intermediate strain-rate Hopkinson bars are currently under development, strain-controlled mechanical testing at these strain-rates remains unavailable. Instead, impact testing (see Chapter 3 and the Appendix) via material and NOCSAE drop towers was used for performance quantification of polymeric foams at strain rates of 50/s to 200/s.

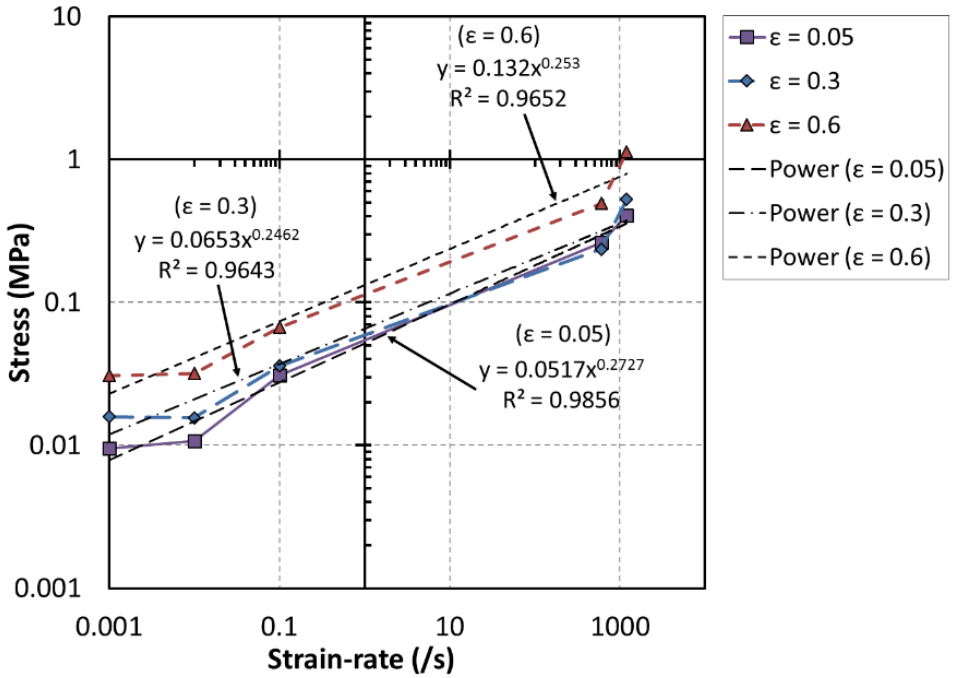

Figure 2.14 Log-Log plot of the strain-rate dependence of the plateau strength of SunMate Firm.

Note: The stress for strain levels of ε = 0.05, ε = 0.3, and ε = 0.6 are plotted and fit with power function trend lines showing equations and R^2 values.

In general, the higher density foam showed greater strain-rate dependence compared to the lower density foams. The mechanisms for strain-rate dependence of the baseline foam were examined by comparison between a similar foam with differing density at strain-rates closest to that of the application, in this case 0.1/s and 600/s. Figure 2.15 shows the differences in the compressive stress-strain response of SunMate Firm and SunMate Medium density foams. The stress-strain response of these foams are shown with uncertainty bands representing experimental uncertainty with a 95% confidence. When subjected to high-rate testing at a strain-rate of 600/s, both densities show a large increase in strength as compared to the quasi-static compressive tests at 0.1/s. The Firm density foam in Figure 2.15 shows greater increase in strength, higher stresses, at the higher strain rate tests, as compared to the medium density foam.

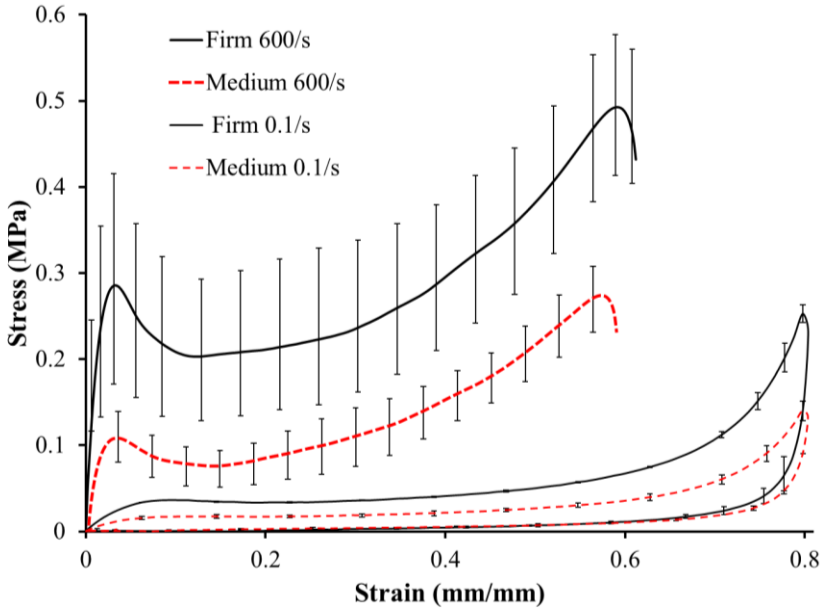

Figure 2.15 Compressive Stress-strain response of SunMate Firm and Medium densities at strain rates of 600 per second and 0.1 per second show high strain-rate dependence.

Note: Stress-stain curves are shown with uncertainty bands representing the random uncertainty of the test results with a 95% confidence level (n = 3).

2.4 Summary and Conclusions

The structure-property relations of a slow-recovery open-cell polyurethane foam were quantified in this study. The cellular structure of this foam was examined using optical and scanning electron microscopy methods and image analysis. Various parameters including Poisson's ratio, density, porosity, and stiffness were determined experimentally. The compressive mechanical response of this open-cell foam was characterized by monotonic and hysteretic experiments at low strain-rates (0.001, 0.01 and 0.1/s), and monotonic high strain-rate experiments (600 and 1200/s). The following conclusions can be drawn from this study:

1) the microstructure of the baseline open-cell foam shows anisotropy, cell size irregularity, random distribution and a very low degree of interconnecting cells
2) The strain-rate dependence of an open-cell polyurethane foam was quantified at high strain-rates (1200-600/s) and low strain-rates (0.1-0.001/s).
3) Generally, the higher density foams showed greater strain-rate dependence than the lower density foams.

CHAPTER III

THE ENERGY DISSIPATION CHARACTERISTICS OF FOOTBALL HELMET LINERS

3.1 Introduction

The purpose of this chapter is to establish the impact performance characteristics of liner materials and determine which material attributes would be most advantageous for use as a football helmet liner. The localized compressive stress-strain response liner materials was examined by quasi-static (Instron), high-rate (Split-Hopkinson bar), and drop tower impact testing. The global impact response of liner materials was examined by conducting NOCSAE drop tests of select materials inside the baseline helmet and comparing them to four commonly used football helmets.

Concussion is one of the most common injuries in football today, even with the most advanced football helmets. Previous studies by Viano et al. [57] and Bartsch et al. [58] have shown minimal advancement in helmet technology over the past 25 years. Bartsch et al. [58] showed that in many cases the head impact doses and head injury risks while wearing vintage leatherhead helmets were comparable to those wearing the widely used 21st century helmets, illustrating the need for better football helmet liners. The present study entails a quantitative method to examine modern football helmet liners and a novel liner design for concussion mitigation.

There are a variety of padded liner systems currently used in modern football helmets. Traditionally football helmets have consisted of closed cell foam liners with polycarbonate shells [8]. Recently, some non-foam based liner systems have taken the field. These systems rely on engineered chambers to mitigate impact. A variety of padded liner systems are explored in the present study. In this work, the modern football helmet "control group" consists of the Rawlings Quantum Plus, Riddell 360, Schutt Ion 4D, and Xenith X2 helmets. These helmets represent some of the most recent "advancements" in helmet technology. All of these "control group" helmets have polycarbonate shells while their liners and facemask systems vary. The Riddell 360 has a closed cell foam-based liner system (vinyl nitrile). The Schutt Ion 4D and the Xenith X2 helmets primarily employ engineered chambers as their energy absorbing liners. The Rawlings Quantum Plus liner is a hybrid-type that consists of a foam component and an engineered chamber component. An additional description of the "control group" helmets and their facemask attachment systems is presented in Chapter 5. The baseline football helmet of this study, the Rush helmet, is unique from other football helmets since its design incorporates a composite shell with an integrated flush-profile facemask design and an open cell foam based liner. The aforementioned helmets examined in this study are shown in Figure 3.1.

Figure 3.1 Modern football helmets tested showing the (a) Rush (Baseline), (b) Rawlings Quantum Plus, (c) Riddell 360, (d) Schutt Ion 4D, and (e) Xenith X2 helmets.

Note: Helmet (a) has a composite shell while helmets (b), (c), (d), and (e) have polycarbonate shells. Helmet scales may not be relative.

3.1.1 The Mechanical Response of Polymeric Foams

Foams are typically loaded in compression and exhibit a non-linear function of stress and strain upon loading. For polymeric foam the unload curve does not follow the load curve because stress not only depends on the actual strain level but also the strain history of the foam. Figure 3.2 shows the typical response of a polymeric foam to an application of load and removal of that load at a constant strain rate. In response to loading, a polymeric foam typically shows three regions in its stress-strain curve [45]. Region I, the linear elastic region, is defined the linear region compressive stress-strain response up to around 7% strain. Region II, the plateau region, is identified by a near constant stress, typically up to 60-70% stain. Region III, the densification region, is defined for strains generally greater than 70% and is indicative of a sharp increase in the slope of the stress strain curve. In Figure 3.2, the solid line (loading curve) represents the

materials response to an application of compressive load (loading curve), while the dashed line represents the material response when the load is reduced (unloading curve). The total area below the loading curve represents the specific energy absorbed by the material during loading (areas A plus B). The amount of specific energy dissipated by the material, also known as hysteresis, is represented by Area A. The area below the unloading curve (area B) represents the materials rebound specific energy or the energy that is stored in the material by compressive loading and released upon unloading.

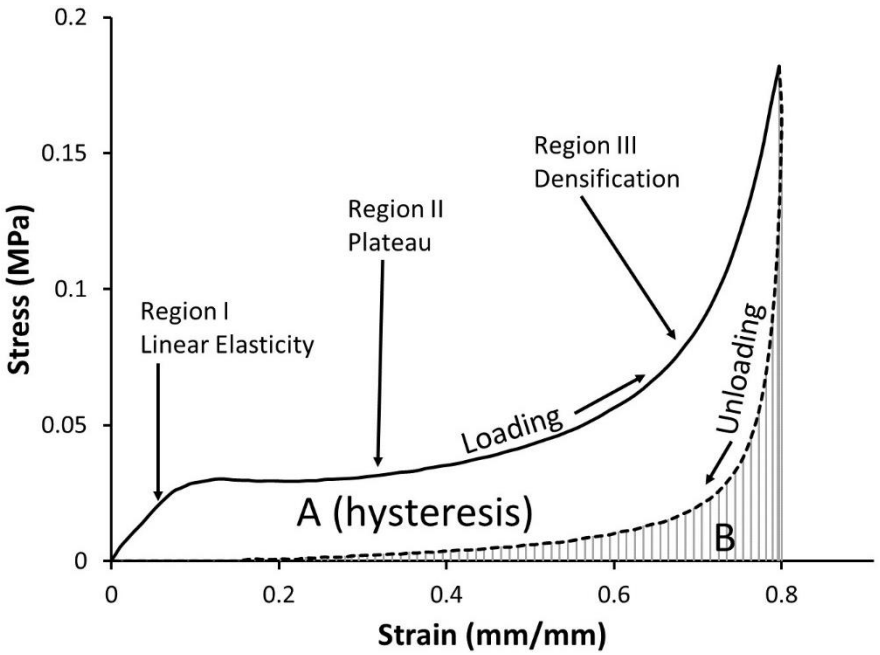

Figure 3.2 Typical load-unload compressive stress-strain response of polymeric foam showing; the three characteristic regions of the loading curve, and the energy absorbed by the material during loading (area A plus area B), the energy dissipated in area A (hysteresis), and the specific rebound energy (area B).

3.2 Methods

A materials list is defined in Table 3.1 describing the liner and shell for each helmet tested in this study. Each of these helmets were tested under NOCSAE drop test for characterization of their global impact response at a Top impact location. Well after completion of drop tests, liner samples were extracted from the top section of each helmet for compression testing.

Table 3.1 Helmets under evaluation with their liner types, liner materials and shell materials.

Helmet	Liner Type	Liner Material	Shell Material
Rush Baseline	Foam	OC PU	GRPP Composite
Rush V2	Encapsulated Foam	OC PU + TPU	GRPP Composite
Rawlings Quantum Plus	Foam + Engineered Chamber	OC PU + TPU	Polycarbonate
Riddell 360	Foam	CC Vinyl Nitrile	Polycarbonate
Schutt Ion 4D	Engineered Chamber	TPU	Polycarbonate
Xenith X2	Engineered Chamber	TPU	Polycarbonate

3.2.1 Quasi-static Compression Testing

Compressive testing of helmet liner specimens includes quasi-static as well as high-rate tests. Quasi-static compression tests were conducted on an Instron 5869 (Instron Engineering Corporation, Norwood, MA, USA) with a 25.4 mm extensometer at the Center for Advanced Vehicular Systems (CAVS). Quasi-static compressive test were conducted on a 3 specimens per foam type at a strain-rate of 0.1/s.

3.2.2 High-rate Compression Testing

High-rate compressive test were conducted at CAVS using a 2 inch diameter polycarbonate Split Hopkinson Pressure Bar (Center for Advanced Vehicular Systems, Starkville, MS, USA) at strain-rates of 500-600 per second. The Hopkinson bar was

equipped with strain-gauges to and data was acquired at a sample rate of 1MHz using a Vishay Micro Measurements, Model Number 2310A Signal Conditioning Amplifier (Vishay Americas Inc., Wendell, NC, USA). Three samples of each liner material were tested. Calibrations and post-processing routines were the same as defined in section 2.2.4. Since thicknesses of current helmet liners ranged and the samples were tested "in whole" strain-rates for high rate compression tests of these samples slightly varied, 500 ± 50 per second. Strain rates were calculated based on a three test average.

3.2.3 Impact Testing

Impact testing was performed via two methods employing a NOCSAE twin-wire drop tower (Southern Impact Research Center, Rockford, TN, USA). The first method was to test the local impact response of the liner materials alone. The second method was to test selected liner materials inside of the baseline helmet, thus taking into account the global geometry of the helmet including the shell and facemask. Helmet impact testing was also performed on a control group of currently used helmets including the Rawlings Quantum Plus, Riddell 360, Schutt Ion 4D, and Xenith X2.

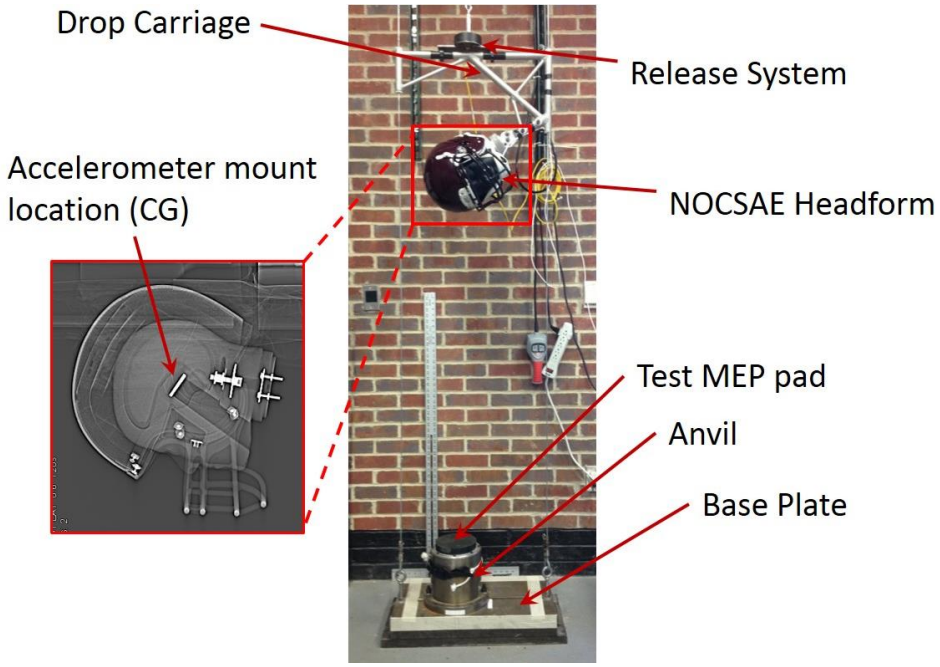

Figure 3.3 The NOCSAE Twin-wire drop tower used for helmet impact testing.

Helmet impact testing was conducted by means of a NOCSAE drop tower with modified test methods. The NOCSAE twin-wire drop tower and its components are shown in Figure 3.3. Drop test were performed on the different liner materials at 4.88 and 5.46 m/s impact velocities. This impact testing procedure required proper fitting of the helmet onto the large NOCSAE headform and dropping it in free fall onto a one-half inch Modular Elastomer Programmer (MEP) test pad attached to the anvil. Three consecutive drops were performed with a time interval of 90 ± 15 seconds for each helmet configuration in the NOCSAE standard top impact location. The results were compared to the previously tested results of the Rawlings Quantum Plus, Riddell 360, Schutt Ion 4D, and Xenith X2 helmets. The strain-history dependence of the baseline, control

group, and revised helmet were explored by as set of seven consecutive drop tests. Additional NOCSAE drop tests procedural information can be found in Chapter 5.

3.3 Results and Discussion

3.3.1 Impact Response of Football Helmets

Figure 3.4 displays resultant acceleration-time plots for the Riddell 360, Rawlings Quantum Plus, Xenith X2, and Schutt Ion 4D helmets as compared the response of the novel helmet at study, Rush V2, at a Top impact location for two impact velocities. In Figure 3.4, the Rush V2 helmet shows much lower acceleration values as compared to the other helmets. Also displayed in Figure 3.4 are 75%, 50% and 25% concussion probability thresholds proposed by King et al. [59]. In Figure 3.4.a, The Rawlings Quantum Plus, Riddell 360, Schutt Ion 4D, and Xenith X2 helmets all exceed the 75% concussion probability threshold while the Rush V2 helmet breaches the 25% concussion probability threshold. In Figure 3.4.b the Rush V2 helmet stays well below the 25% acceleration threshold for concussion while the Schutt Ion 4D and Xenith X2 helmets breach the 75% threshold and the Riddell 360 and Rawlings Quantum Plus breach the 50% threshold. The rest of this study will focus on examining the mechanisms that allow this Rush V2 football helmet to keep acceleration levels, and forces to the head, much lower than these other commonly used football helmets.

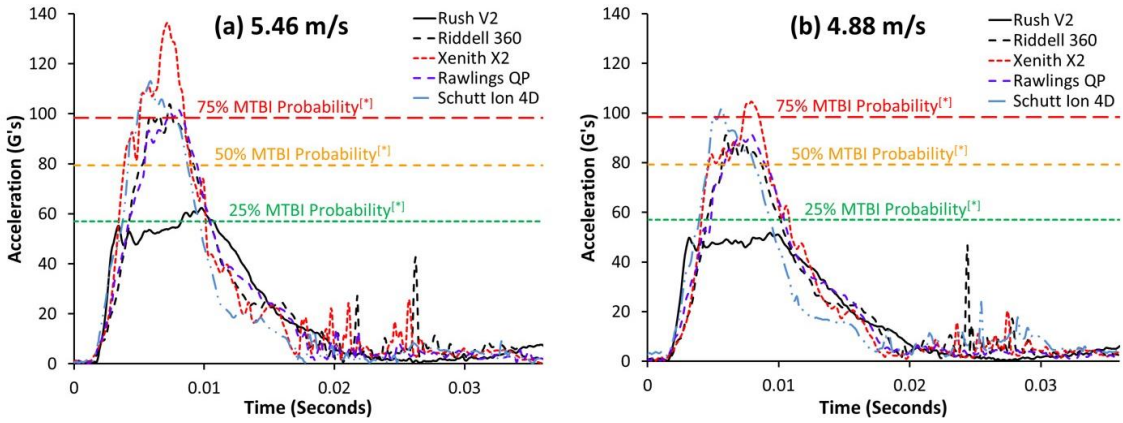

Figure 3.4 Resultant Acceleration-time plots for 5.46 meters per second (a) 4.88 meters per second (b) impacts for Rush V2, Rawlings Quantum Plus, Riddell 360, Schutt Ion, and Xenith X2 Helmets with Facemasks attached at a Top impact location.

Note: * 75%, 50% and 25% Mild Traumatic Brain Injury (MTBI) probabilities from King et al. [59] are depicted.

Table 3.2 shows results of HIC, SI, and peak acceleration for the same impact scenarios as previously depicted with an addition of the baseline Rush helmet, from which Rush V2 originated. Shown in Table 3.2 are mean Peak G, HIC, and SI values with standard deviations for three consecutive impacts (90 ± 15 seconds) with maximum and minimum values. Here, the Rush V2 helmet shows HIC and SI values that are approximately half of that of the other helmets. While an examination of the strain-history of these helmets will follow, the standard deviations in Table 3.2 can be indicative of the helmets ability to recover after impact. A helmet having a higher standard deviation would have a wider range in recorded HIC, SI, or Peak G values for these consecutive impacts, indicating that the helmets liners are not absorbing as much energy for the second and third impacts and that their recovery time is longer than the drop interval.

Table 3.2 NOCSAE Drop test results of the Rawlings Quantum Plus, Riddell 360, Schutt Ion 4D, Xenith X2, Baseline Rush, and revised Rush V2 Helmets at a Top impact location with the facemasks attached.

		Peak G				HIC				SI			
Velocity	Helmet	Mean	SD	Min	Max	Mean	SD	Min	Max	Mean	SD	Min	Max
5.46m/s	Rawlings QP	99.85	6.38	92.76	105.15	403.10	33.23	367.00	432.40	478.80	37.41	439.07	513.35
	Riddell 360	101.47	4.31	96.49	104.06	408.50	17.74	388.20	421.00	472.41	23.81	445.17	489.25
	Schutt Ion 4D	112.42	0.59	111.96	113.08	470.50	25.38	441.20	485.40	534.98	27.97	502.71	552.26
	Xenith X2	134.36	2.28	131.87	136.34	616.87	33.64	585.50	652.40	720.51	25.79	703.04	750.13
	Rush (Base)	127.17	4.51	121.99	130.23	458.27	25.72	428.70	475.50	561.62	31.88	524.99	583.08
	Rush V2	62.74	0.92	62.09	63.79	216.47	2.71	213.50	218.80	235.03	2.87	231.93	237.59
4.88m/s	Rawlings QP	89.32	3.60	85.16	91.47	321.60	19.52	299.50	336.50	381.32	24.33	353.78	399.88
	Riddell 360	89.25	3.53	85.18	91.51	296.33	18.54	275.70	311.60	346.36	21.66	321.94	363.24
	Schutt Ion 4D	103.08	1.37	101.83	104.55	362.70	16.51	349.80	381.30	418.80	18.05	403.43	438.68
	Xenith X2	104.33	2.04	102.16	106.22	404.43	10.72	397.70	416.80	466.56	11.88	456.55	479.69
	Rush (Base)	84.05	8.40	74.95	91.52	253.13	27.77	222.70	277.10	291.21	36.93	250.74	323.09
	Rush V2	52.17	1.36	51.00	53.66	153.60	1.97	151.40	155.21	167.46	1.94	165.38	169.21

Note: NOCSAE Drop test results of the Rawlings Quantum Plus, Riddell 360, Schutt Ion 4D, Xenith X2, Baseline Rush, and revised Rush V2 Helmets at a Top impact location with the facemasks attached.

3.3.2 Strain-History Dependence of Football Helmets

Resilience, or the ability to recover after an applied load, is an important parameter for football helmet liner design. The mechanical response of a typical polymeric foam is strain-history dependent, meaning the mechanical response of a foam depends on the history of its loading. A liner must be able to recover its strain energy after impact in a manner that is timely enough to sufficiently protect the player from a second impact. In this study, the strain-time history of each helmet was monitored for seven consecutive drops of each helmet with the facemasks attached at a Top impact location for 5.46 and 4.88 m/s impact velocities. An example of HIC results for multiple consecutive impacts of the Baseline Rush, Rush Version 2, Rawlings Quantum Plus, Riddell 360, Schutt Ion, and Xenith X2 helmets at 4.88 m/s are depicted in Figure 3.5.

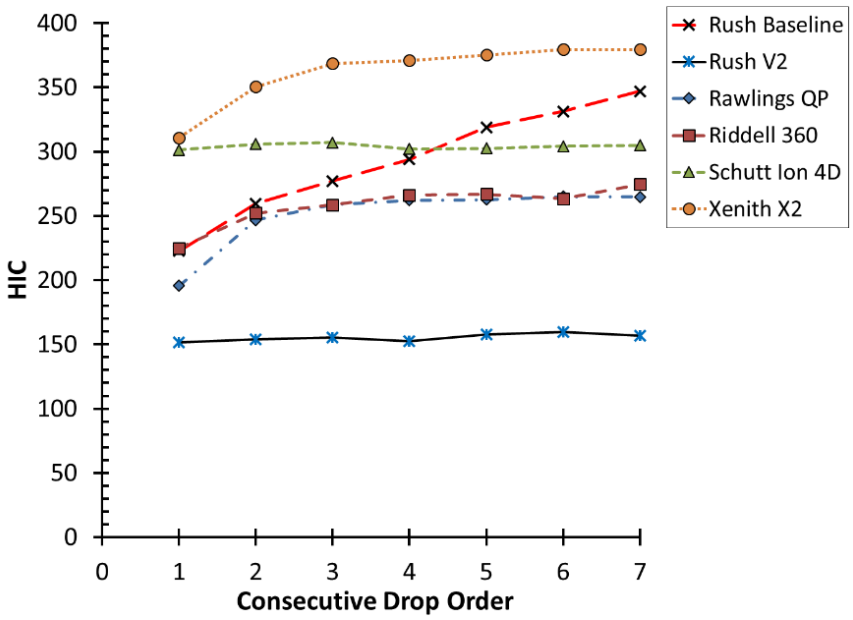

Figure 3.5 HIC results for multiple consecutive impacts of the Rush Baseline, revised Rush V2, Rawlings Quantum Plus, Riddell 360, Schutt Ion 4D, and Xenith X2 football helmets.

Note: The revised Rush helmet (V2) shows better recovery of the foam liner after impact as compared to the Baseline Rush liner for this 4.88 m/s Top impact.

Here, each drop was conducted within a time interval of 90 ± 15 seconds, which was the fastest time interval possible for the given test set-up. Each helmet shows strain-time history dependence when subjected to these consecutive impacts. In Figure 3.5, the Rawlings Quantum Plus, Riddell 360, and Xenith X2 helmets show a similar strain-time history profile for the 4.88 m/s multiple consecutive drops, having an increase in HIC between the first and third impacts but a more consistent HIC value between the fourth and seventh impacts. The Schutt Ion 4D helmet shows a different response, showing a near horizontal response. As shown in Figure 3.5, the Rush V2 helmet shows the lowest strain-history dependence showing a near horizontal line when HIC is plotted against consecutive drop order (HIC was the nearly the same for all impacts). This indicates that

the Rush V2 liner was able to fully recover within the impact time interval and that it is possible to achieve a delayed rebound in the liner component. In contrast the Rush Baseline helmet shows the highest strain history dependence. The Rush baseline is seen having a near constant increase in HIC for each consecutive impact. This response in the Rush baseline helmet indicates that the liner is not fully recovering in the time span allotted between impacts. Thus, the liner is pre-loaded further and further after each impact and its energy absorption is adversely effected. Similar trends were seen for SI and peak G for both 5.46 and 4.88 m/s impact velocities for all helmets.

3.3.3 Stress-Strain Response of Helmet Liners

Quasi-static stress-strain curves were generated for the liner materials listed in Table 3.1. Figure 3.6 depicts the response of the Rush V2 compared to the Rawlings Quantum Plus, Riddell 360, Schutt Ion 4D and Xenith X2 helmet liners. The quasi-static stress strain response of these current football helmet liners show unique response to uniaxial loading and unloading.

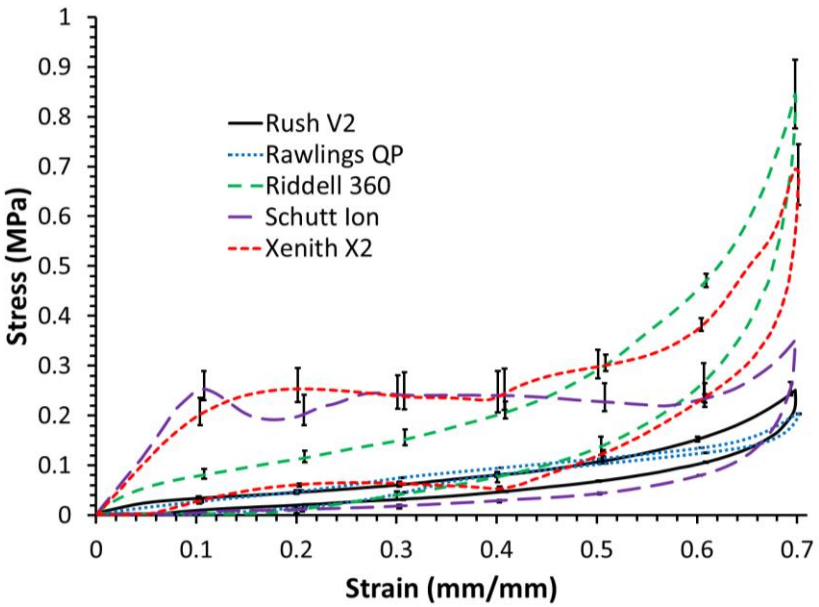

Figure 3.6 Quasi-static hysteretic compressive stress-strain response of the Rush V2 liner compared to the Rawlings Quantum Plus, Riddell 360, Schutt Ion 4D and Xenith X2 helmet liners.

Note: Test were conducted at a strain rate of 0.1 per second.

The two helmet systems with engineered chamber-based liners, the Schutt Ion 4D and the Xenith X2, show very non-uniform stress-strain responses due to the geometry of each pad. The stress-strain response of the Schutt Ion pad (Figure 3.6) shows distinct regions of compression, similar to that of a typical polymer foam. A linear region is seen a low strain levels ($0 < \varepsilon < 0.1$) which is dominated by bending of the solid TPU material in the walls of its engineered chamber. A dip is seen in the stress-strain curve profile at around ($0.1 < \varepsilon < 0.25$) that is indicative of non-uniform buckling of the TPU followed by further more-uniform buckling ($0.25 < \varepsilon < 0.6$). Finally a densification region is seen where the walls of the engineered chamber begin to impinge on each other. The stress strain response of the Xenith X2 pad also shows uniqueness with distinct regions of compression. The compressive response of the Xenith X2 pad shows a linear region at

low strain levels ($0 < \varepsilon < 0.1$) due to bending in the cylindrical wall of its engineered chamber. A plateau region follows ($0.1 < \varepsilon < 0.4$) that is presumably dominated by bending and viscous dissipation. The Xenith's plateau region is shorter and more uniform than that of the Schutt pad. Finally, an elongated densification region is seen starting at 40% strain for the Xenith X2 pad. This shortened plateau region and elongated densification region is possibly owed to an increase in internal pressure exacerbated by impingement of the air channels and overly stiff chamber walls.

Figure 3.7 shows the specific energy absorbed for the quasi-static compression tests of the liner materials listed in Table 3.1. The quasi-static stress strain responses of the Rush V2, Rawlings Quantum Plus, Riddell 360, Schutt Ion 4D and Xenith X2 helmet liners showed unique stress-strain curve profiles and a wide range of stress magnitudes. When specific energy was plotted as a function of strain (Figure 3.7), the Schutt Ion 4D and Xenith X2 helmets had the highest initial slopes which were nearly identical up to about 40 percent strain where the slope of the Xenith liner increased and the slope of the Schutt liner remained linear. The Riddell 360 helmet liner shows a convex specific energy to strain profile with comparatively the highest slope at near the end, indicating higher stress values. Both the Rawlings Quantum Plus and Rush V2 helmet liners show very similar specific energy-strain relationships, indicating that they absorb about the same energy for the same rate upon (quasi-static) loading.

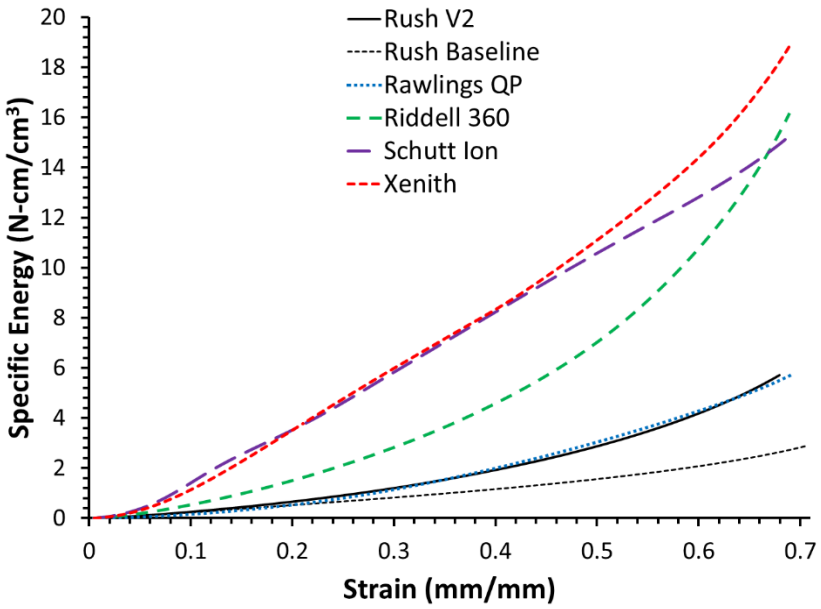

Figure 3.7 Specific energy absorbed as a function of compressive strain for the Rush V2, Rush Baseline, Rawlings Quantum Plus, Riddell 360, Schutt Ion 4D and Xenith X2 helmet liners.

Note: Test were conducted at a strain rate of 0.1 per second.

The helmet control group with foam-based liners, the Rush (baseline), Rush V2 the Rawlings Quantum Plus, and the Riddell 360, showed to have a high strain-rate dependence. Figure 3.8 shows the stress-strain response of these liner materials when subjected compression at high strain rates of 600/s. The shape of the stress-strain curve for the Riddell liner is very different than for these high-rate test as compared to its quasi-static response.

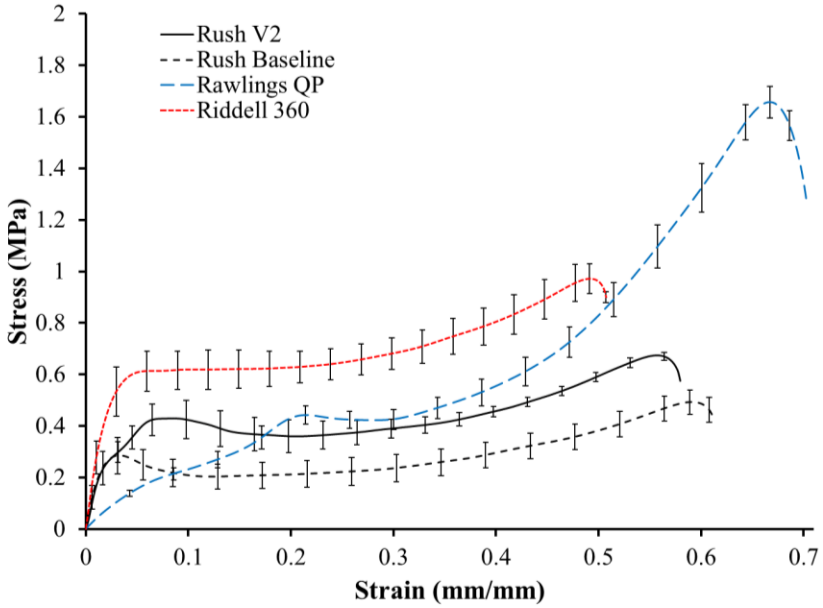

Figure 3.8 High-rate compressive stress-strain response for the foam-based helmet liner groups including; the Rush V2, Rush Baseline, the Rawlings Quantum Plus, and the Riddell 360 helmet liners.

Note: Tests were conducted at a strain rate of 600 per second and results are shown with standard error with a 95% confidence level (n = 3).

3.3.4 Helmet Impact Mitigation Mechanisms

The helmet shell and facemask prevent direct contact loading to the head. Rapid contact loading induces a stress wave that propagates through the helmet shell, liner, scalp, cerebrospinal fluid, skull and finally to the brain. Each component of the helmet serves various impact mitigating functions. The helmet shell acts to distribute a localized force over a large area while some energy absorbed through bending. A rigid helmet shell permits less bending of the helmet shell and allows more liner material to do work by providing added contact area between the skull and the liner. An impact to a more flexible helmet shell would result in higher deformation and consequentially less area of the liner would remain in contact with the head. Additionally, a more flexible helmet shell would allow higher stress concentrations at the site of impact. For these reason more

flexible helmet shells typically require stiffer liners. The faceguard provides rigidity to the helmet shell while also protecting to face from direct impact. Rush et al [60] has shown that the faceguard can have up to a 50% difference in average impulsive forces during impact.

The helmet liner mitigates impact by redistributing a localized force over a larger area, therefore reducing the local stress on the skull, and it sets an upper limit determined by the plateau-stress of the foam to the magnitude of this distributed force [45]. This upper limit of the foam determines how much acceleration is transmitted to the brain during impact, as long as the liner does not reach densification. The key to minimizing acceleration and average impulsive force to the head is to provide the maximum amount of deformation possible up to the onset of the foams densification region (typically 70% strain). Using all of this plateau region of a foams characteristic stress-strain response curve maximizes the amount of strain energy stored while it minimizes the reaction force by setting a stress limit. In an open-cell foam energy is also lost by viscous dissipation due to frictional forces of the air escaping the cell openings of the foam. Force is reduced by a liner of a helmet by energy dissipation upon compression, by extending the duration of the impulse, and by dispersing the contact force of the impact over a larger area, thus reducing the localized stress. The force of the head is equal to the compressive stress of the foam times the area of contact between the head and the foam.

Uniaxial impact testing of a polymeric foams (Table 3.3 and Figure 3.9) indicates that there is an optimal density that should be selected based on force thresholds for a given energy range. The varying responses of peak linear acceleration, rebound velocity, maximum strain, and strain energy should all be taken into account when selecting a liner

material or a certain density for a given foam type. When a foam is impacted by a falling mass of specific weight and velocity, the impact energy (kinetic energy), would be the same for all similar tests but the impulse (at least in the first acceleration pulse) would be different. This is because there is a resulting rebound velocity that is dependent on the material density and type, impact velocity and impacting mass. This rebound velocity is related to the hysteretic response of the materials stress-strain curve.

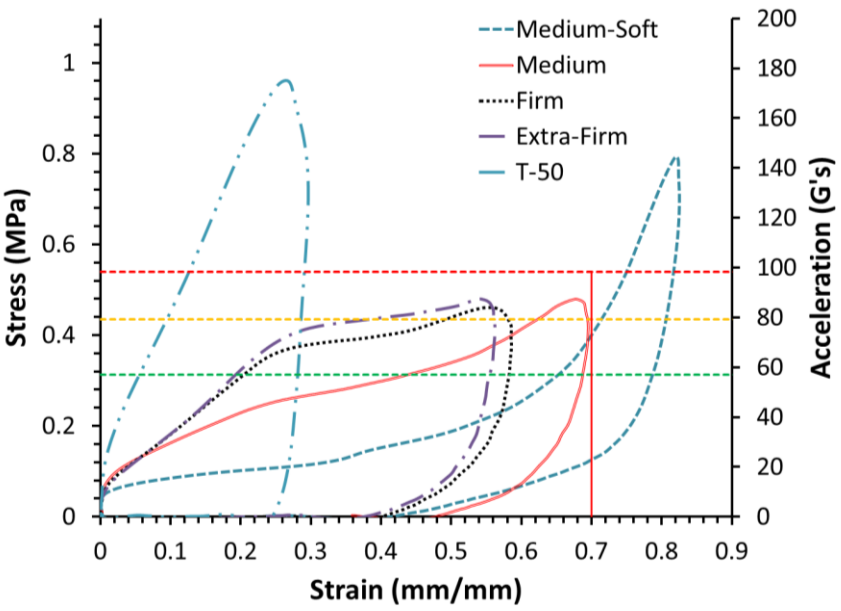

Figure 3.9 Stress-strain versus acceleration plot showing material drop tower results of an example foam at an impact velocity of 4.88 m/s.

Peak stress and the corresponding acceleration values are illustrated for T-50 (XX-Firm), Extra-Firm, Firm, Medium, and Medium-Soft densities of an open-cell foam of the same area and thickness subjected to an impact of a 5 kg mass.

By examination of the results for the 4.88 m/s impacts in Figure 3.9 and Table 3.3, one can see that the XX-Firm density, followed by the Medium-Soft density materials had the highest peak acceleration values for opposing reasons. The XX-Firm material had the highest density and the highest plateau (crush) stress and would be too

"stiff" to be a good material for reducing acceleration for this given impact mass and velocity. On the other hand, the Medium-Soft material was not "stiff enough" and bottomed out by compressing well into the densification region of its stress-strain curve. The densification region is defined by having a sharp increase in stress and is typically initiated at approximately 70% strain depending on the material density and strain-rate. In order avoid this sharp increase in force, it is good practice select a material that will extend to this densification region for your maximum design impact energy, as indicated in the vertical red line in Figure 3.9. The Medium density material would be the optimal material in Figure 3.9 if the 4.88 m/s impact velocity was the maximum design limit. This Medium density foam uses all of the strain-energy up to the densification region and has low acceleration at the 4.88 m/s velocity but it meets the same fate as the Medium-Soft for the 5.46 m/s impacts. Table 3.3 indicates that an energy-only design criteria will not be suitable for selecting an optimal liner material. The 5.46 m/s impact velocity results for the Medium density foam has the highest energy absorption but it is not optimal since it also has the second highest acceleration.

Table 3.3 Material drop tower results showing the relationship of foam density to impulse and energy absorption for an open-cell polyurethane foam for two initial impact velocities of a 5 kg mass.

Density	v_i (m/s)	KE (J)	I (N*s)	v_f (m/s)	LA (G's)	ε_{max}	SR_{max} (s^{-1})	U_o (N-cm/cm^3)	E_{foam} (J)	E_{foam}/KE	COR
T-50	4.89	54.23	24.35	-0.48	175.06	0.30	206.91	16.63	34.24	0.63	0.10
X-Firm	4.89	54.23	25.99	-0.84	87.44	0.56	203.16	13.59	36.15	0.67	0.17
Firm	**4.89**	**54.23**	**26.00**	**-0.84**	**84.04**	**0.59**	**192.35**	**17.56**	**35.91**	**0.66**	**0.17**
Medium	4.89	54.23	27.07	-1.08	87.33	0.70	203.76	16.83	36.44	0.67	0.22
Medium-Soft	4.89	54.23	29.49	-1.61	144.59	0.83	216.11	17.44	27.99	0.52	0.33
X-Firm	5.47	67.79	35.25	-2.31	112.53	0.68	235.23	26.16	53.87	0.79	0.42
Firm	**5.47**	**67.79**	**29.62**	**-1.06**	**105.60**	**0.72**	**224.98**	**21.61**	**44.51**	**0.66**	**0.19**
Medium	5.47	67.79	32.70	-1.74	176.85	0.85	230.41	26.24	40.56	0.60	0.32

The impulse (I), rebound velocity (vf), peak linear acceleration (LA), maximum strain, maximum strain-rate, energy absorbed by the foam (Efoam), energy absorption fraction, and the Coefficient of Restitution (COR) are shown.

Drop tower testing revealed that the local quasi-static compression response of a liner material does not truly represent its global impact performance. Foams are typically characterized by their quasi-static mechanical response to loading, which can either be a force-controlled or, as conducted in this study (Instron), a strain-controlled test. In a strain-controlled test, strain is applied at a constant rate (strain-rate) while in a force controlled test, force is applied at a constant rate. Impact testing of foam is neither a force-controlled nor a strain-controlled environment. Instead the system is a dynamic environment governed by the conservation of energy and the principle of impulse and momentum. During an impact test, there is no additional energy input, as it would be for force-controlled or strain-controlled mechanical testing. For example, a strain controlled mechanical testing the XX-Firm foam would have the highest stress with the most amount of energy absorption. In contrast, impact testing (Figure 3.9 and Table 3.3)

revealed that the XX-Firm foam resulted in the highest acceleration and second lowest energy absorption.

A materials ability to perform as a helmet liner depends on its strain-rate sensitive mechanical response to load (namely plateau stress), its contact area and the kinetic energy of the impact. In this two-dimensional case for the material drop tower, the force is reduced because energy is being absorbed and dissipated by the foam. In a three dimensional environment, such as the NOCSAE drop tests, the local stress is further reduced by an increase in surface area due to the curvature of the helmet shell. As the foam deforms, the contact area of the foam with the head increases, further reducing the local stresses.

3.4 Summary and Conclusions

In this chapter, the impact performance of liner materials was analyzed and insight into an optimal liner design was presented. The Rush Baseline, Rush V2, and four commonly used football helmets; the Rawlings Quantum Plus, Riddell 360, Schutt Ion 4D, and Xenith X2 were examined. The global helmet response was examined by NOCSAE drop tower impact testing and comparison of HIC, SI, and peak acceleration values. The localized compressive stress-strain response of liner materials was examined by quasi-static (Instron), high-rate (Split-Hopkinson Pressure Bar), and drop tower impact testing. The following conclusions can be made from this study:

1) The coupling between the helmet liner and the helmet shell may be as important as the liner properties themselves.
2) Analysis of a liners local quasi-static compression response does not represent the global impact performance.

3) Comparisons of a liner materials energy absorption is not a sufficient means for liner material selection
4) An optimal liner material should maximizing deformation of the liner upon impact up to the densification region. Maximize the amount of strain energy while minimizing stress.

CHAPTER IV

EXPERIMENTAL DESIGN OPTIMIZATION OF A FOOTBALL HELMET LINER

4.1 Introduction

The goal of this chapter is to perform experimental design optimization on a novel football helmet liner to verify its suitability for concussion prevention. This novel helmet liner consists of an encapsulated viscoelastic foam design that has been modified to increase resiliency for multiple-impact head protection. Exploratory designs were developed and tested by an exploratory design of experiments that examined ten parameters with two different levels using modified NOCSAE drop tests. The gas inside the foam, the number of foam layers, density of the foam (for each layer), the length of the pads, surface area ratio of the liner, the diameter of the pads, the configuration of the pads within the helmet, the number of dampeners, and the encapsulate thickness were selected as design factors. The baseline helmet shell, facemask, and chinstrap components remained fixed throughout the experiments. The liner parameters were optimized based on peak acceleration, Head Injury Criterion (HIC), and Severity Index (SI) results from multiple consecutive impacts using the guided twin-wire test device. An optimal football helmet design was experimentally quantified by NOCSAE drop tests.

An optimal football helmet liner must have high energy absorption, sufficient resilience and operability over various environmental conditions. The balance of energy absorbance and resilience is a key aspect to a football helmet liner's performance. A

helmet liner for contact sports, such as football, must be able to withstand multiple impacts without permanent deformation. Upon an impact, the liner must be able to return to form in a sufficient time increment in order to absorb the next impact. This resilience requirement is what differs between helmets for contact sports from those of single-use applications, such as bicycle helmets. Bicycle helmets normally take use of a crushable foam liner while helmet liners for contact sports must be flexible and resilient.

In this study, experimental design optimization was performed on the liner for a specific football helmet. This baseline helmet was developed by Rush Sport Medical (Meridian, MS) and is unique from other football helmets since it incorporates a composite shell with an integrated flush-profile facemask and an open-cell polymeric foam based liner. This baseline helmet liner proven to have very efficient at impact attenuation but shows poor resilience with a slow recovery time. Exploratory designs were developed as method of increasing the resilience of the baseline liner material.

4.2 Methods

4.2.1 Development of Exploratory Liner Designs

The helmet liner exploratory designs consist of a novel composite consisting of an open-cell viscoelastic foam component encapsulated in a Thermoplastic Elastomer (TPE) component [61]. Foam selection was based on intermediate strain-rate drop tower impact tests results of over 50 foams, each differing in material, cellular structure and/or density (see Appendix). Rankings of HIC and peak acceleration results were used for candidate foam selection. Three densities of SunMate brand open-cell viscoelastic foam (Medium, Firm, and Extra-Firm) were selected based on rankings, as these foams were shown to have minimal peak acceleration values over three consecutive (90 ± 15 seconds) impact

tests . Results of these tests showed that the selected foams had a slow recovery time and thus could be improved by increasing the resilience (rebound) of the material. A method of encapsulation was selected to increase the candidate foams resilience. Preliminary impact tests were conducted and have shown this method to effectively reduce average HIC and peak acceleration by increasing recovery time, thus minimizing preload during consecutive impacts. Using the selected foams and encapsulation method, exploratory designs were produced by variations of the following parameters. Cylindrical shapes differing in diameter were used for the foam component. The foam component consisted of one to two layers differing in density. The TPE encapsulate was constructed from Thermoplastic Urethane (TPU), which differed in thickness. The number of cylinders in the impacted section of the helmet varied by two area fractions. All of these varying parameters were explored by using a L12 Taguchi Design of Experiments during NOCSAE drop tests. A schematic of the novel exploratory helmet liner design is shown in Figure 4.1.

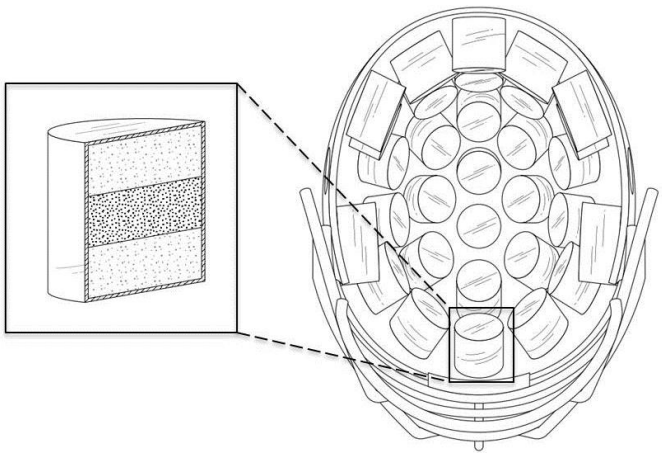

Figure 4.1 Schematic showing the novel exploratory helmet liner design [61].

4.2.2 Design of Experiments by NOCSAE Drop Tests

In this work, a Design of Experiments (DOE) methodology was based on a Taguchi orthogonal array which was used to explore the helmet liner design space and conduct a sensitivity analysis the design parameters. The Taguchi method [62, 63] is a structured approach for determining the best combination of inputs to produce a product from a robust design perspective. This design perspective approach was used to investigate the mean responses and variations in the liner design parameters and determine their significance.

The Design of Experiments employed examination of ten parameters with two different levels (1, 2). The parameters include the following: gas inside the foam (air, helium), the number of foam layers in the cylinder (1, 2), density of the base foam layer 1 (Extra firm, Firm), the density of foam layer 2 (Medium, Firm), the number of dampeners inside of the helmet (0, 6), the total length of the foam cylinder (1", 1.5"), surface area ratio of the liner (number of cylinders) (0.75, 0.45), the diameter of the cylinder (1.6", 1.85"), the configuration of the cylinders within the helmet (Direct, Indirect) (e.g. if the impact point is directly aligned with the axis of a cylinder), and the TPU thickness that covers the cylinders (35 mils, 15 mils). The results examined were the HIC, SI, and acceleration values recorded from NOCSAE drop tests. Results from the DOE were used to determine the most influential parameters on the HIC, SI, and acceleration. The most influential parameters were applied to a reduced test matrix that was used for design optimization. Table 4.1 and Table 4.2 show the L12 DOE matrix used for sensitivity analysis.

Table 4.1 An L12 Design of Experiments (DOE) matrix illustrating the different experiments highlighting the variations in the two parameter levels.

Expt.No.	Col.1	Col.2	Col.3	Col.4	Col.5	Col.6	Col.7	Col.8	Col.9	Col.10
1	1	1	1	1	1	1	1	1	1	1
2	1	1	1	1	1	2	2	2	2	2
3	1	1	2	2	2	1	1	1	2	2
4	1	2	1	2	2	1	2	2	1	1
5	1	2	2	1	2	2	1	2	1	2
6	1	2	2	2	1	2	2	1	2	1
7	2	1	2	2	1	1	2	2	1	2
8	2	1	2	1	2	2	2	1	1	1
9	2	1	1	2	2	2	1	2	2	1
10	2	2	2	1	1	1	1	2	2	1
11	2	2	1	2	1	2	1	1	1	2
12	2	2	1	1	2	1	2	1	2	2

Table 4.2 The L12 Design of Experiments (DOE) matrix illustrating the different experiments with the varying parameter definitions included.

	Col. 1	Col. 2	Col. 3	Col. 4	Col. 5	Col. 6	Col. 7	Col. 8	Col. 9	Col. 10
Expt. No.	Gas	Density Layer 1	Density Layer 2	Number of Layers	Number Dampeners	Total Length	Area Ratio	Diameter	Impacted Location	TPU Thickness
1	Air	XF	M	1	N=0	1"	0.75	1.6"	Direct	15 mil
2	Air	XF	M	1	N=0	1.5"	0.45	1.85"	Indirect	35 mil
3	Air	XF	F	2	N=6	1"	0.75	1.6"	Indirect	35 mil
4	Air	F	M	2	N=6	1"	0.45	1.85"	Direct	15 mil
5	Air	F	F	1	N=6	1.5"	0.75	1.85"	Direct	35 mil
6	Air	F	F	2	N=0	1.5"	0.45	1.6"	Indirect	15 mil
7	Helium	XF	F	2	N=0	1"	0.45	1.85"	Direct	35 mil
8	Helium	XF	F	1	N=6	1.5"	0.45	1.6"	Direct	15 mil
9	Helium	XF	M	2	N=6	1.5"	0.75	1.85"	Indirect	15 mil
10	Helium	F	F	1	N=0	1"	0.75	1.85"	Indirect	15 mil
11	Helium	F	M	2	N=0	1.5"	0.75	1.6"	Direct	35 mil
12	Helium	F	M	1	N=6	1"	0.45	1.6"	Indirect	35 mil

4.2.3 Sample Preparation

Precut sheets of slab stock open-cell polyurethane foam were obtained from the manufacturer in specified densities. Cylindrical specimens were then cut by means of a drill press and hole-saw bit. Samples requiring two layers of foam were held together by tacking their interphase with a single dab of superglue adhesive. Two layers of TPU was then vacuum formed onto the samples on the top and bottom sides to obtain an

encapsulated specimen. The samples requiring helium were then inserted into a pressurized helium-filled chamber for at least four hours. Helium was then injected into the required specimens using a needle tipped hose attached to the regulator of a helium tank. A hypodermic needle was inserted in specimen to allow air to escape and the pressure to equilibrate to 1 atmosphere. Specimens were then sealed by means of a heat-gun and stored in a helium rich environment until testing. Selected samples were weighed before and after helium injection to ensure that the methodology was allotting the helium to be retained in the specimens.

4.2.4 Pad Placement

For each of the 12 tests, the configuration of liner pad placement was obtained by equally spacing the number of foam specimens to cover the top section of the helmet in a manner that would sufficiently protect the players head from other directions of impact. In general the samples were dispersed in a configuration that would prevent head-shell contact in all impact directions on the top side of the helmet. The inner-shell surface area of this top section of the helmet was determined to be approximately 60 square inches. The area of the headform corresponding this top section (liner-head contact area) was approximately 36 square inches. The difference in these two areas is due to the curvature of the helmet shell. One parameter tested in the experimental design was whether or not the impact occurred directly on a pad. For a “direct impact” liner configuration a cylindrical pad was centered directly at the impacted location, or first site of the helmet shell contact with the MEP test pad. For an “indirect impact” liner configuration, the pads were placed in a manner where the site of impact would be between two or more cylinders. The contact area of the foam with the head would be equal to the area summed

surface area of all the pads in the experiment. Due to the curvature of the helmet shell, this contact area is always less than the inner-shell surface area.

4.2.5 Impact Testing

Impact testing was performed by NOCSAE twin-wire drop test at a top impact location at a 5.46 m/s impact velocity. The top impact location was selected since it induces the least amount of rotation in the twin-wire test device. Hence, the highest linear acceleration per angular acceleration is achieved in the top impact location. The 5.46 m/s impact velocity was selected as it is the highest velocity tested by NOCSAE standards and maximum impact velocity allotted by height restrictions of the twin-wire test device at the top impact location. The twelve sets of liner sections were inserted into the top section of the prototype helmet with facemask attached and impacted onto a 1" MEP seven times. Each experiment was performed by seven consecutive impacts (90 ± 15 seconds).

4.2.6 Instrumentation

A PCB Piezotronics Model 353B17 triaxial accelerometer was securely attached at the headform's CG. The accelerometer was connected to Diversified Technical Systems, Inc. Tiny Data Acquisition Systems 2 (TDAS2) data acquisition (DAQ) module through a current source controller. Data from the DAQ module was processed by a Windows PC using TDAS software. The headform frame was attached to an electromagnetic release, controlled by a toggle switch. The mechanical release switch was connected to the hardware trigger for the DAQ module. Upon testing, the switch was activated, simultaneously releasing the electromagnet and triggering a timed data

acquisition of 0.040 seconds before activation and 1.15 seconds after activation. Calibration routines were conducted according to NOCSAE test standards. Instrument calibration was performed before any tests were conducted. The sample rate was taken at a frequency of 16,512 Hz with a 3300 Hz anti-alias filter and a 1650 SAE Class 1000 filter. Calibration required drops of the desired test height onto a 76.2 mm thick Calibration MEP Pad. Three calibrations were consecutively performed and a fourth drop with the prior calibration data was conducted to check for consistency. Recalibration routines were conducted prior to change in impact velocity or impact orientation.

4.2.7 Data Analysis

Data analysis was conducted by comparing HIC, SI, and acceleration (G's) values between parameter groups and experimental configurations. A sensitivity analysis was piloted by signal to noise ratios for examining the influence of each parameter. Once the parameter influences were quantified, an Analysis of Variance (ANOVA) method was used to compare difference in means between experimental configurations.

A signal to noise ratio was calculated for each experiment conducted to determine the effect each parameter had on the resulting HIC, SI, and acceleration values. Since we want to minimize these results, Taguchi's smaller-is-better signal to noise ratio was used [64]. The signal to noise ratio was calculated using the following equation,

$$SN_i = -10 \log_{10} \frac{1}{n} \sum {y_i}^2 \tag{4.1}$$

where N_i is the number of trials, y_i is the respective characteristic values (G's, HIC, or SI) and n is the number of observations for each experiment [62, 63, 65]. Average signal to noise ratios were calculated for each level (air, helium, etc.) and the difference between

these SN ratios were calculated for each parameter (gas, density, etc.) and ranked. For example, the SN ratio of G's was calculated for air (level 1 of parameter gas) according to Equation 4.1 using the values of G's (y_i) for the six experiments (n = 6) that contained air. In the same manner, the SN ratio of G's was calculated for helium. The difference between these two SN ratios represented the effect that the parameter gas had on the values of G's. Rankings were used to show which parameters had the largest effects on HIC, SI, and acceleration values.

Mean differences were calculated for comparison of HIC, SI, and acceleration values between experiments. ANOVA was computed using, HIC, SI and Acceleration (G's) as dependent variables and mean squared error. The ANOVA employed a difference in least squares means procedure and type III sum of squares F-tests. These F-tests were used to evaluate the significance of interactions between classes and for determining p-values. A 0.05 level of significance ($\alpha = 0.05$), an equal means null hypothesis ($\mu 1 = \mu 2$), and a difference between means alternative hypothesis ($\mu 1 \neq \mu 2$) were used for all statistical analysis. The significance of mean differences by ANOVA F-tests, can be found in Table A3 of the Appendix. All statistical analysis was performed using SAS 9.4 (SAS Institute, Cary, NC, USA).

4.3 Results and Discussion

Experimental NOCSAE drop tests indicate a high dependence on the liner parameters, showing large differences in peak acceleration (G's), HIC, an SI, for the twelve experiments in the DOE, as shown in Table 4.3. Here, mean G's, HIC, and SI results are presented with standard deviations for seven consecutive drop tests. Resulting G's, HIC, and SI values ranged considerably between these experiments showing a high

dependence on the varied parameters. Preliminary examination of these results yields that experiment number five has the lowest peak acceleration, HIC, and SI values, indicating that it would be the safest configuration of this experiment set. Experiment number four shows to be the worst configuration tested thus far, having the highest of these measured values. The peak acceleration, HIC, and SI results for experiment four are more than double that of experiment number five. The effect that each parameter has on this large variance in results are quantified next.

Table 4.3 Experimental NOCSAE drop test results showing peak acceleration (G's), HIC, and SI for each seven consecutive drop tests for each of the twelve experiments.

Expt. No.	Gas	Layup	Total Length	Area Ratio	Dia-meter	Impacted Location	TPU Thick-ness	G's	HIC	SI
1	air	XF	1"	0.75	1.6"	direct	15 mils	113.14 ± 7.96	471.99 ± 35.99	528.98 ± 45.72
2	air	XF	1.5"	0.45	1.85"	indirect	35 mils	75.21 ± 4.55	254.21 ± 13.05	287.82 ± 17.31
3	air	XF-F	1"	0.75	1.6"	indirect	35 mils	103.03 ± 6.14	454.2 ± 24.00	503.48 ± 37.45
4	air	F-M	1"	0.45	1.85"	direct	15 mils	160.34 ± 5.71	671.64 ± 51.56	822.39 ± 56.27
5	air	F	1.5"	0.75	1.85"	direct	35 mils	68.58 ± 1.82	257.73 ± 5.03	281.31 ± 5.26
6	air	F-F	1.5"	0.45	1.6"	indirect	15 mils	87.78 ± 6.04	275.17 ± 16.94	340.03 ± 25.09
7	helium	XF-F	1"	0.45	1.85"	direct	35 mils	132.59 ± 9.13	515.16 ± 52.59	621.73 ± 71.06
8	helium	XF	1.5"	0.45	1.6"	direct	15 mils	86.14 ± 7.23	277.24 ± 21.46	328.87 ± 29.44
9	helium	XF-M	1.5"	0.75	1.85"	indirect	15 mils	76.16 ± 4.84	268.67 ± 20.77	299.55 ± 24.09
10	helium	F	1"	0.75	1.85"	indirect	15 mils	120.56 ± 9.72	472.01 ± 46.53	550.95 ± 61.29
11	helium	F-M	1.5"	0.75	1.6"	direct	35 mils	70.1 ± 3.41	260.09 ± 18.07	280.89 ± 18.05
12	helium	F	1"	0.45	1.6"	indirect	35 mils	135.46 ± 11.32	515.8 ± 50.70	631.27 ± 73.85

In Table 4.4, total rankings of the differences in signal-to-noise ratios show that Length, followed by area ratio, and density 1 were the most influential parameters. Here, results from the sensitivity analysis show the influences of the ten liner parameters on HIC, SI, and peak acceleration (G's) values. The calculated signal-to-noise ratios for a "smaller-is-best" situation is shown for the following ten parameters with two levels (1,

2): gas (air, helium), density 1 (extra firm, firm), density 2 (medium, firm), number of layers (1, 2), number of dampeners (0, 6), total length (1", 1.5"), area ratio (0.75, 0.45), diameter (1.6", 1.85"), pod configuration (direct, indirect), and TPU thickness (35 mils, 15 mils). Rankings of the differences in these signal-to-noise ratios show the degree of influence that each of these parameters had on G's, HIC, and SI. Comparisons of signal-to-noise ratios within a parameter can be used to infer which level is better but the degree of influence is most important. The level with the highest (least negative) signal-to-noise ratio for each parameter would represent the best outcome, having the lower G's, SI, or HIC value. For example, the signal-to-noise ratios for air are higher than that of helium in all cases. Thus, liners with air had lower acceleration, HIC, and SI, values than liners with helium. Though more importantly is the degree of influence of the parameter on acceleration, HIC, and SI values. By examination of the total rankings, gas had a rank of 10, being the least influential parameter.

Table 4.4 Sensitivity analysis results showing signal-to-noise ratio responses and rankings for the liner design parameters in a smaller-is-best situation.

	Level	Gas	Density 1	Density 2	#Layers	# Damp	Length	Area Ratio	Diameter	Pod Config	t_{TPU}
G's	1	-238.62	-121.04	-121.63	-238.40	-238.55	-252.24	-234.31	-238.56	-240.04	-236.59
	2	-240.08	-117.36	-118.68	-240.30	-240.15	-226.45	-244.39	-240.14	-238.66	-242.11
	|Diff|	1.46	3.68	2.95	1.91	1.59	25.79	10.08	1.58	1.39	5.52
	Rank	9	4	5	6	7	1	2	8	10	3
HIC	1	-308.36	-156.03	-156.24	-306.52	-306.53	-325.30	-305.32	-306.95	-309.77	-306.38
	2	-307.88	-150.49	-153.49	-309.73	-309.72	-290.95	-310.93	-309.30	-306.48	-309.87
	|Diff|	0.48	5.53	2.75	3.21	3.18	34.35	5.60	2.36	3.28	3.50
	Rank	10	3	8	6	7	1	2	9	5	4
SI	1	-315.71	-159.91	-160.63	-313.97	-314.12	-333.72	-310.95	-314.62	-317.08	-313.20
	2	-315.75	-154.06	-156.86	-317.49	-317.34	-297.74	-320.51	-316.84	-314.38	-318.26
	|Diff|	0.05	5.85	3.77	3.52	3.22	35.98	9.56	2.22	2.69	5.06
	Rank	10	3	5	6	7	1	2	9	8	4
	Score	29	10	18	18	21	3	6	26	23	11
	Total Rank	10	3	5	6	7	1	2	9	8	4

Note: Rankings are presented in decreasing order, as the lowest rank corresponds with the parameter that most effects the Acceleration (G's), HIC, and SI response variables.

Normalization of the sensitivity analysis results by the most influential parameter, total length, provides a comparison of next most influential parameters, as depicted in Figure 4.2. Even with this normalization, it evident that the length parameter is the most important but it is also the most limited in terms of helmet design. While obviously a thicker liner component would result in a safer helmet, as far as linear acceleration is concerned, there are practical limitations to the liners thickness. Increased angular acceleration and additional torque on the neck by an excessively thick helmet could result in injury to the player. For these reasons and for the fact that we are using a predefined shell geometry, we are limited with a maximum liner thickness of 1.5".

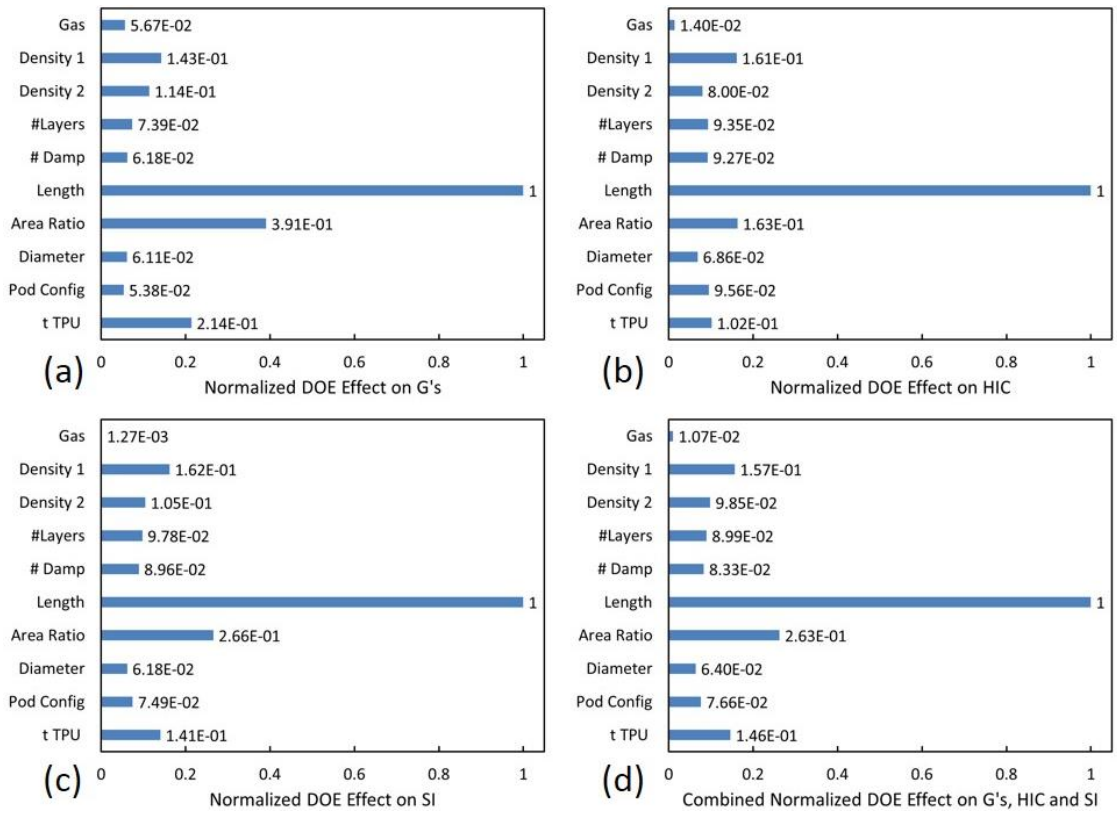

Figure 4.2 Normalized sensitivity analysis results showing influences of the ten liner parameters during drop tests.

(a) Peak acceleration (G's), (b) Head Injury Criterion (HIC), (c) Severity Index (SI) and (d) the combined effect of G's, HIC, and SI, are normalized by total length.

By omitting total length, the reduced sensitivity analysis results were normalized by the second most influential parameter, the area ratio. The relationship of the next most influential parameters is amplified showing a unique trend, as depicted in Figure 4.3. Here, the third and fourth most influential parameters are density 1 and TPU thickness, respectively, for Acceleration (G's), HIC, and SI. The parameter fractions for G's (Figure 4.3a) and SI (Figure 4.3c) show striking similarity with magnitudes differing from the parameter fractions for HIC (Figure 4.3c). This implies that area fraction may be relatively less influential for HIC, as it would be for G's and SI. By referring back to

Table 4.4, examination of the differences in signal-to-noise ratios (|Diff|) shows that the area ratio is less influential for HIC, comparted to G's and SI but the influence of density 1, diameter and pod configuration increase. The enhanced influence for these factors for HIC presumably indicates that they may affect the time duration of the impact (as would length) consequentially leading to a greater difference in HIC values.

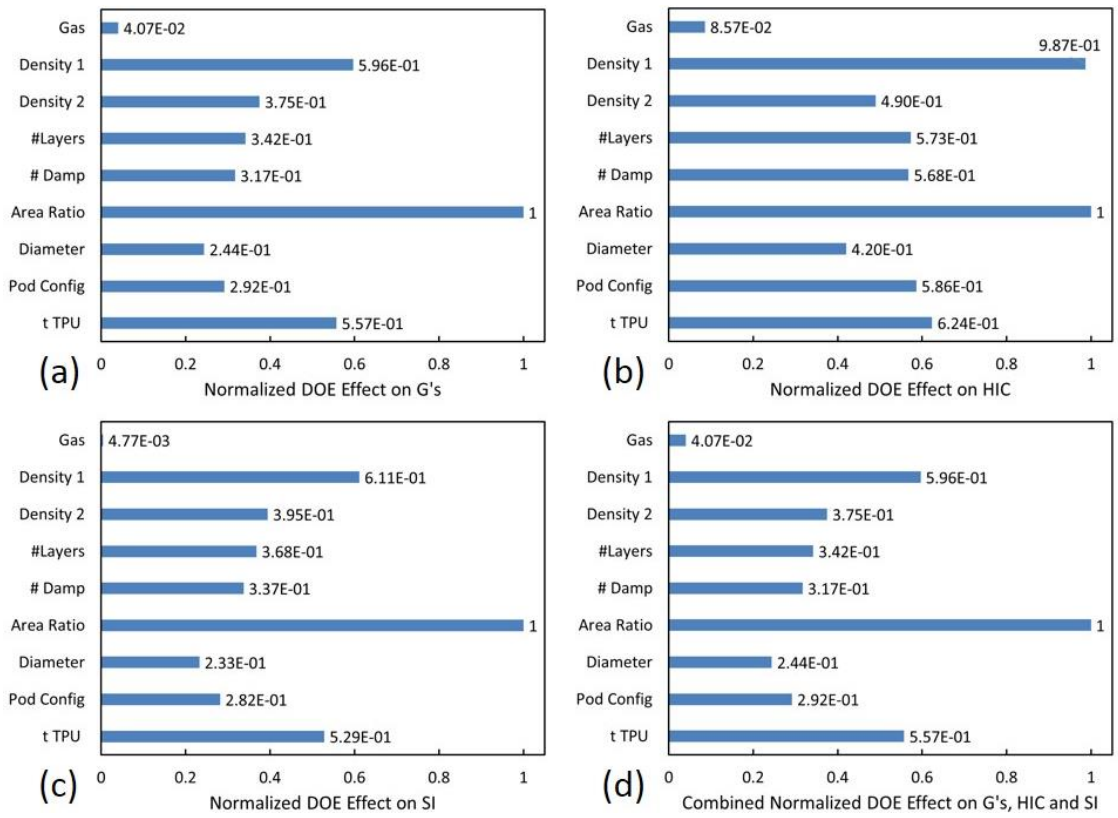

Figure 4.3 Reduced normalized sensitivity analysis results showing influences of nine liner parameters during drop tests.

(a) Peak acceleration (G's), (b) Head Injury Criterion (HIC), (c) Severity Index (SI) and (d) the combined effect of G's, HIC, and SI, are normalized by area ratio. Note: The effect of total length is not shown.

The area ratio, density 1, and TPU thickness were used as parameters for design optimization. Further experiments were conducted to examine the design space and

adjust these parameters while fixing the total length to 1.5 inches. The optimal liner design was procured by first independently adjusting area ratio and then exploring the interactions of area ratio, density 1 and TPU thickness. First, area ratio was examined independently by fixing all other parameters and conducting tests on a wider range of area ratios. Figure 4.4 shows the exaggerated effect of area ratio for Firm density foam. Here, six different area ratios were examined incrementally from an extremum 97% (3% free space) to 45%. An optimal area ratio of 75% is found for this specific density, having the lowest G's, HIC, and SI values. The rationale for this is inherently straight-forward; there can either be too much foam or not enough foam, where the optimum is between. The specific mechanisms for this relate back to the foam's non-linear characteristic stress-strain response. The characteristic stress-strain curve of a polymeric foam shows a short linear elastic region, long plateau region (near constant stress) and a densification region (sharp increase in stress). An optimal liner absorbs the most amount of energy per the lowest stress by using all of the strain energy in the plateau region without reaching densification. In a global sense this is accomplished by designing a force limit that is set by the crush stress in the plateau region of the materials stress-strain curve. Too much foam area results in a global increase in crush stress threshold, or global stiffness, as such that the stress would be high and the strain energy would be low. Too little foam area lowers the global stress thresholds as such that the material would crush into the densification region.

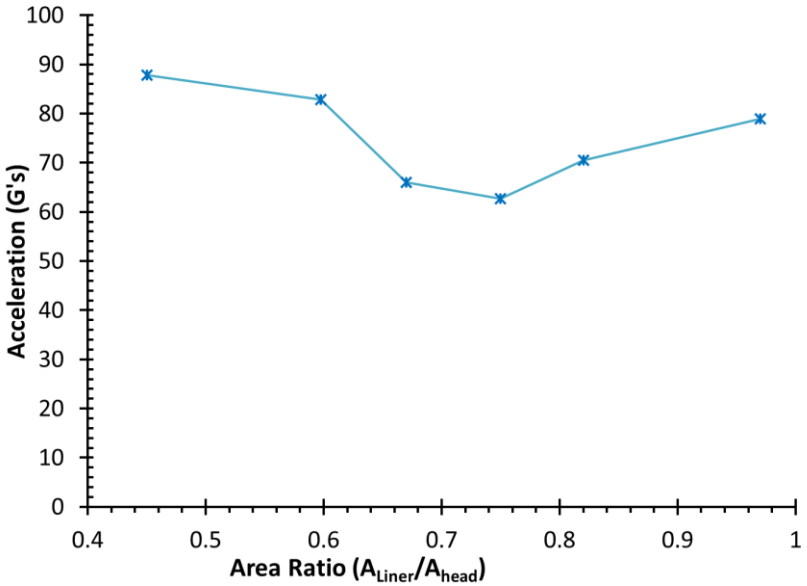

Figure 4.4 Area ratio versus acceleration (G's) for Firm density, 1.5" length liner specimens.

Note: An optimal area ratio of 0.75 is found for this specific liner configuration.

Finally, the interactions of area ratio with density and TPU thickness were examined for various experiments using a method of normalization, the global density. Along with area ratio, the global stiffness of the liner is also dependent on the foam density and TPU thickness. For example, an increase in TPU thickness for a given area ratio and foam density, would result in an increased global stiffness of the liner. For a fixed pad length (1.5 inches), the area ratio, foam density and TPU thickness are related to the global liner stiffness by the amount of solid material between the head and the helmet shell. Using this idea, the combined effects of these parameters were explored by normalizing using the mass of solid material for the given effective cross-sectional area (A_{head}). Table 4.5 depicts the relationship between the global density and Peak G, HIC, and SI results. A local density (pad density) was calculated for each trial according to the following equation,

$$\rho_{Local} = (1 - V_{TPU})\rho_{foam} + (\rho_{TPU} V_{TPU}) \quad (4.2)$$

where ρ_{foam} is the number density of the foam, ρ_{TPU} is the TPU density (1200 kg/m3), and V_{TPU} is the TPU volume fraction of the cylinder. Multiplying the local pad density by the area ratio equates to the global density of the liner configuration, which serves a method of normalization across the area ratio, density and TPU thickness parameters. Global density is defined by the following equation,

$$\rho_{Global} = \rho_{Local} A_R \quad (4.3)$$

where ρ_{Local} is the local pad density an A_R is the area ratio. A plot of global density versus acceleration response, Figure 4.5, shows a concave shape with a location where acceleration is minimized to 63 g's at a global density value of 106 kg/m^3. This unique response is indicative that there is optimal convergence between the local density and area ratio at the minimized value. Similar responses were seen for global density in respect to HIC and SI.

Table 4.5 Liner design optimization results showing the relationship between global density, local density, foam density and TPU thickness.

Density/ Layup	ρ_{foam} (kg/m^3)	t_{TPU} (mil)	% TPU	ρ_{Local} (kg/m^3)	A_R	ρ_{Global} ($\rho_{Local} * A_R$)	Peak G	HIC	SI
F	84.3	15	3.27	120.78	0.45	54.35	82.62 ± 6.04	262.2 ± 16.87	319.85 ± 25.10
XF (He)	85.6	15	3.27	122.04	0.45	54.92	79.84 ± 6.39	258.47 ± 19.24	303.87 ± 27.73
XF-M (He)	82.75	15	3.27	140.29	0.45	63.13	72.14 ± 5.14	253.0 ± 25.46	280.77 ± 28.49
XF	85.6	35	7.11	164.83	0.45	74.18	71.47 ± 4.86	245.3 ± 16.6	275.77 ± 21.65
F-XF (1"-0.5")	84.73	25	5.15	121.20	0.75	90.90	70.25 ± 2.01	258.17 ± 7.33	279.261 ± 8.50
F	84.3	25	5.15	141.76	0.67	94.98	66.02 ± 2.56	235.9 ± 12.01	257.33 ± 12.17
F	84.3	25	5.15	141.76	0.75	106.32	62.74 ± 0.75	216.47 ± 2.21	235.34 ± 2.11
F-M (He)	82.1	35	7.11	161.58	0.75	121.19	67.41 ± 2.7	248.23 ± 24.13	272.10 ± 5.97
F	84.3	35	7.11	163.63	0.75	122.72	68.0 ± 2.7	254.33 ± 5.67	278.01 ± 5.97
F	84.3	25	5.15	141.76	0.82	134.17	70.48 ± 0.84	257.83 ± 4.41	285.12 ± 5.36
F	84.3	25	5.15	141.76	0.97	137.51	78.91 ± 2.02	295.43 ± 12.42	328.78 ± 14.43

Note: The optimal liner design is shown in the shaded region.

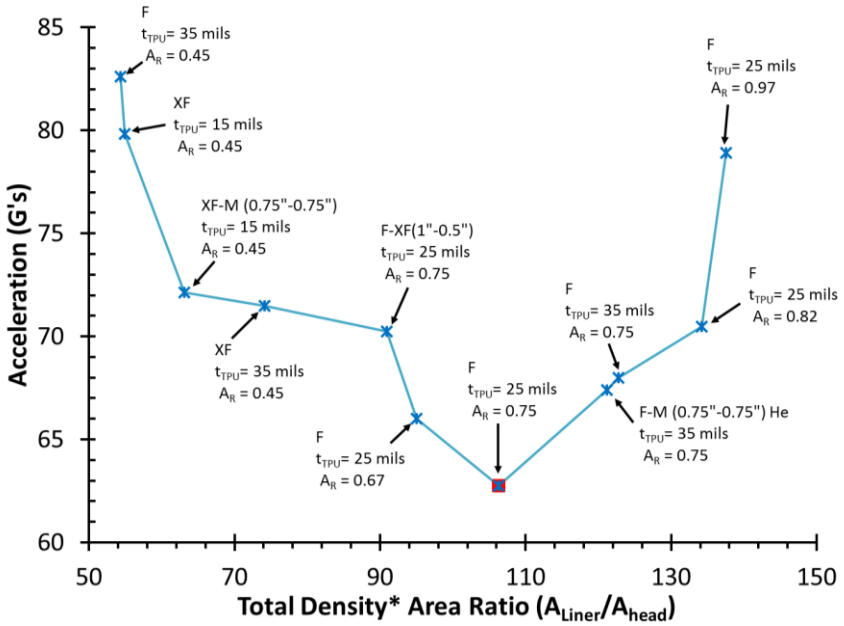

Figure 4.5 Global density (total density* area ratio) versus acceleration (G's) for 1.5" liner experiments.

According to the normalization of area ratio, density, and TPU thickness, an optimal liner design for the experiments conducted in this study was found to have a 1.5" pad thickness, a 75% area ratio, a foam density of 84.5 kg/m^3 (Firm), and a 25 mil encapsulate thickness. The optimal total length of the cylindrical pads was found to be 1.5 inches. Total length was the most influential parameter on HIC, SI, and peak acceleration values but was limited by a maximum liner thickness of 1.5 inches due to the predefined helmet shell geometry. The foam density, TPU thickness and area ratio were determined to be dependent parameters that relate to the global stiffness of the liner component by their global density value. An optimal global density value of 106 kg/m^3 was determined for a set of area ratio, density 1, and TPU thickness parameters, though the solution may be non-unique. The optimal foam density was found to be a single layer

of SunMate Firm foam (84.5 kg/m^3). The optimal TPU thickness for this density foam was found to be 25 mils. The optimal area ratio for Firm density foam and the 25 mil TPU thickness was found to be 75%. This combination of foam density, TPU thickness and area ratio proved to result in the lowest average peak acceleration, HIC, and SI values over seven consecutive impacts and was selected as the Rush V2 helmet liner.

The optimized helmet liner, the Rush V2, resulted in the lowest Peak Acceleration, HIC, and SI, values during drop tests, as compared to the current helmet control group. Figure 4.6 depicts NOCSAE drop test results showing the Rush V2 helmet having the lowest Peak Acceleration (G's) (Figure 4.6a), HIC (Figure 4.6b), and SI values (Figure 4.6c), as compared to the Rawlings Quantum Plus, Riddell 360, Schutt Ion 4D, Xenith X2, and Rush (Baseline) helmets for 5.46 and 4.88 m/s impact velocities at a Top impact location. Here, the Rush V2 helmet (with optimized helmet liner) shows Peak G, HIC and SI values that are approximately half of that of the other helmets for three consecutive impacts (90 ± 15 seconds). In Figure 4.6, all helmets would have passed the NOCSAE certification limit for these impacts since Severity Index values were below 1200. Compared to these commonly used football helmets, the Rush V2 helmet resulted in the lowest probability of concussion according to peak acceleration, HIC, and SI values.

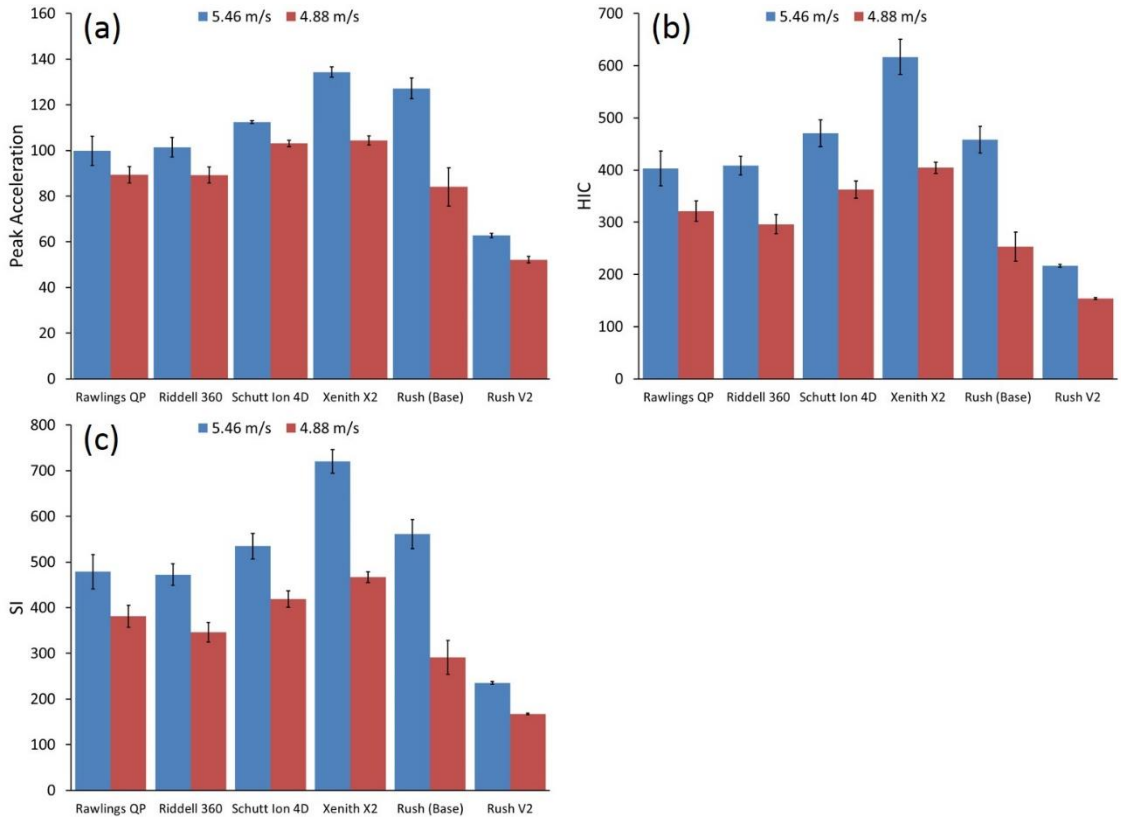

Figure 4.6 NOCSAE Drop test results of the Rawlings Quantum Plus, Riddell 360, Schutt Ion 4D, Xenith X2, Baseline Rush, and Rush V2 helmets shows the optimized Rush V2 helmet has the lowest (a) Peak Acceleration (G's), (b) Head Injury Criterion (HIC), and (c) Severity Index (SI) values at a 5.46 m/s Top impact with facemasks attached.

4.4 Summary and Conclusions

In this study, an experimental design optimization was performed on a novel football helmet liner for concussion prevention. A Design of Experiments methodology was based on an L12 Taguchi orthogonal array which was used to explore the design space and perform sensitivity analysis on ten helmet liner parameters at two levels. NOCSAE drop tests were performed for all experiments and peak acceleration, HIC, and SI values were used as design criterion. The most influential parameters were determined

and were applied to a reduced test matrix for design optimization. The following conclusions can be drawn from the present study:

1) Based on DOE results, the total length, followed area fraction, density, and encapsulate thickness were found to be the most contributing factors for the liner on peak acceleration, HIC, and SI values.
2) Number of foam layers, number of dampeners, and the gas inside the foam were not significantly contributing factors. The gas inside the foam, whether it was air or helium, made little contribution in peak G, HIC, or SI as compared to the other factors.
3) The optimum liner design for the baseline helmet is found to have a foam density of 84.5 kg/m^3, a 1.5" pad thickness, a 75% area ratio, and a 25 mil encapsulate thickness.

CHAPTER V

COMPARISON OF SHELL-FACEMASK RESPONSES IN AMERICAN FOOTBALL HELMETS DURING NOCSAE DROP TESTS

5.1 Introduction

Mild Traumatic Brain Injury (MTBI), more commonly known as a concussion, is one of the most common injuries in contact sports such as football. Sport related brain injuries have been estimated to occur 1.6 to 3.8 million times every year [1]. Football players in particular can receive up to 1500 head impacts per season [2, 3]. Although every impact may not result in a concussion, numerous impacts can result in long-term brain damage through an impact induced neurodegenerative disease known as chronic traumatic encephalopathy (CTE)[4]. Recent publicity [5] of CTE in former professional football players has spurred researchers to find ways to reduce concussion and increase player safety.

Football helmets have made some technological advancement in the past 25 years, but even today's most advanced helmets do not completely mitigate all of the incident forces on the helmet and hence, athletes still incur concussions. A study conducted by Viano et al. [57] showed that of 17 modern helmet models tested, only four provided a significant reduction in head responses compared to the 1990s helmets. Bartsch et al. [58] showed that in many cases the head impact doses and head injury risks while wearing vintage leatherhead helmets were comparable to those wearing the widely used 21st

century helmets, illustrating the need for improvement in the design and testing standards of football helmets. In particular, football helmet certification does not require the facemask to be included in the drop tests for the helmet. The use of a facemask is an essential requirement in football, yet there is no data in published literature on how the addition of the facemask alters the performance of football helmets during certification tests. Theoretically, the added stiffness from the facemask connected to the helmet would dramatically stiffen the overall mechanical response. The present study entails a quantitative method to provide more robust helmet safety standards that would serve as a driving force to promote safer helmet designs.

5.1.1 Head Injury Metrics

The exact biological mechanisms related to MTBI are currently unknown. These injury mechanisms are proposed to relate to several entities: peak linear acceleration, peak rotational acceleration, impact duration, and impulse [23]. Several Injury tolerance criteria have been used in attempt to define MTBI as a measure of linear acceleration. The Wayne State Tolerance Curve (WSTC) [13-15] was developed to predict skull fracture for automotive crashes during a frontal impact by defining a threshold curve boundary for linear acceleration versus impact duration. WSTC has served as the bases for other injury criteria, the Gadd Severity Index [16] (referred to simply as the Severity Index (SI), and the Head Injury Criterion (HIC) [19], which are the two most commonly used criteria. The SI and HIC both measure impact severity based on weighted integrals of the linear acceleration-time profiles. While these criteria define thresholds for linear acceleration, other criteria have been proposed to account for rotational acceleration, such as the Head Impact Power index [23, 40]. Football helmet rating criteria has also been

proposed, such as the Virginia Tech Summation of Tests for the Analysis of Risk (STAR) rating system. The STAR system rates a helmet's performance by a theoretical calculation of a probabilistic analysis of impact exposure based on an impact's location and injury risk [38, 39]. The STAR system applies a weighted fraction to an impact location based on probability. In the current study, the injury metrics considered for the NOCSAE drop tests were peak acceleration, SI, and HIC.

5.1.2 NOCSAE Overview

American football helmets are regulated by the National Operating Committee on Standards for Athletic Equipment (NOCSAE). NOCSAE is an independent and nonprofit standard-setting body formed in 1969 with a goal of reducing sports-related injuries. NOCSAE efforts include the development of performance and test standards to reduce head injuries by establishing requirements of impact attenuation for football helmets/facemasks [66]. These standards are adopted by various regulatory bodies for sports, including the NCAA and the National Federation of State High School Associations.

5.1.3 NOCSAE Test Method

The NOCSAE Football Helmet Standard does not include the testing of helmets with facemasks as it calls for the removal of facemasks before helmet drops are conducted. The NOCSAE helmet testing standards [17] utilize a twin-wire drop impactor that relies on gravity to accelerate the headform and helmet combination to the required impact speeds. The headform is a biofidelic and variable mass headform instrumented with triaxial accelerometers at the center of gravity. The NOCSAE headform is a

synthetic head model designed to mimic the human head at various tissue levels. The NOCSAE headform consists of an elastic outer layer, dense polymer layer and a glycerin filled inner layer, which simulates the skin, bone and brain cavity, respectively [67]. The test involves mounting a football helmet on an appropriately sized and mass specific headform. The headform and helmet combination is then dropped at specific speeds onto a steel anvil covered with a hard rubber Modular Elastomer Programmer (MEP) pad. Two of the most deleterious velocities in the NOCSAE standard are 4.88 m/s and 5.46 m/s, and each impact measurement must be below 1200 SI [68]. We employed these two velocities in our study.

A separate standard test method is used for football facemask certification. The NOCSAE football facemask standard includes structural integrity analysis as well as assessing the impact attenuation performance of the faceguard, chinstrap, and their attachment systems. Each impact measurement must be below 1200 SI, with no facial contact and no mechanical failure of any component, as defined by the NOCSAE Standard [69].

There is a proposed additional NOCSAE test (Linear Impactor (LI)) [68] that includes the helmet with the facemask, but it is not appropriate for football helmet certification because it cannot admit a crown impact. The LI uses a pneumatic ram to impact a helmet positioned on a NOCSAE headform equipped with a hybrid III dummy neck mounted on a linear bearing table in order to induce angular acceleration. While the LI test method should allow pass/fail criteria for rotational acceleration in addition to Severity Index, Gwin et al. [67] found that headform linear accelerations generated by the Linear Impactor were less similar to the game-time head accelerations compared to the

current twin-wire NOCSAE drop test method. Instead of the LI tests, we employed the twin-wire drop test apparatus in the present study.

The NOCSAE standard test method for protective headgear includes six prescribed impact locations and one random impact location. The prescribed impact locations include; Front (F), Front Boss (FB), Side (S), Rear (R), Rear Boss (RB), and Top (T). The random impact location may be selected from any point within the defined acceptable impact area of the helmet. In addition to the six prescribed impact locations, we add two more drop locations defined as the Front Top (FT) and the Front Top Boss (FTB), and we add the facemask to the helmet. Our Front Top and Front Top Boss impact locations are identical to the Front and Right Front Boss impact locations of the NOCSAE standard for Lacrosse Helmets, which also include the faceguard for drop tests [70]. The eight tested impact locations are depicted in Figure 5.1.

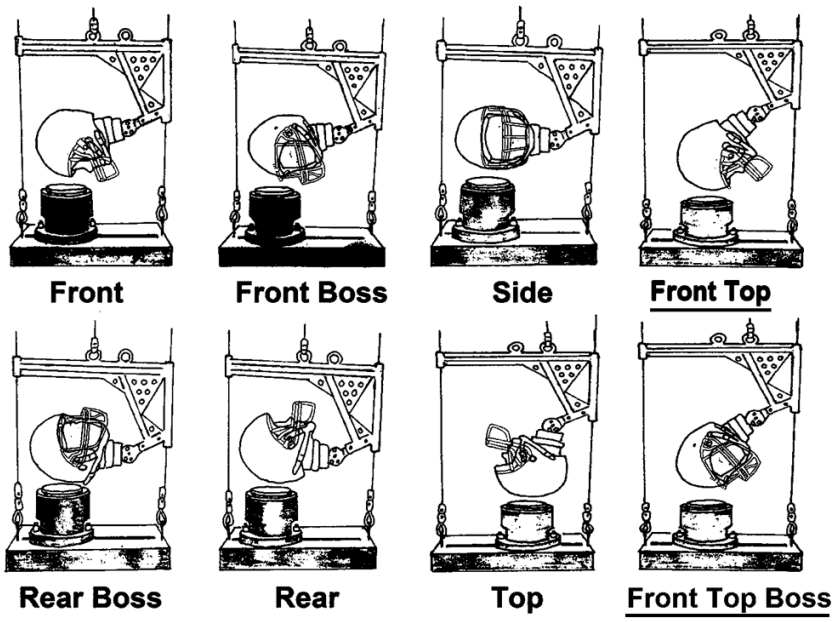

Figure 5.1 NOCSAE drop test setup showing eight impact locations; Front, Front Boss, Side, Front Top, Front Top Boss, Top, Rear, and Rear Boss.

Note: the NOCSAE standard does not include facemask attachment or Front Top and Front Top Boss impact locations, as indicated by the underlined text. (Image modified from NOCSAE DOC (ND) 002-11m12)

The NOCSAE standard SI limit has lowered over time to increase safety. Before 1997 NOCSAE [66] used a 1500 SI pass/fail criterion even though Hodgson et al. [71] in 1970 showed that SI values of greater than 1000 are dangerous to life, while SI values of 540 produced linear skull fractures in non-helmeted cadaveric impact tests. Since 1997 the general pass/fail limit of 1200 SI has been established [66]. In 2011 an amendment [17] has been made to include a pass/fail value of 300 SI for the lowest velocity impacts (3.46 m/s).

5.1.4 Helmet Descriptions

In order to accurately examine each helmet system, we quantified the primary energy absorption mechanisms, facemask-shell joints, and chin strap systems. The

Rawlings Quantum Plus, Riddell 360, Schutt Ion 4D, and Xenith X2 helmets are compared in this study, since they represent some of the newest innovations in football helmet technology. Each helmet tested in this study was an adult size large in a new condition prior to testing with a running-back style facemask coupled to a polycarbonate shell. While facemask designs typically vary by manufacturer, facemasks were selected for each helmet that offered a mid-range of facial protection.

The Rawlings Quantum Plus Helmet has a standard four-point facemask attachment, a standard four-point chin strap attachment, and a dual-material liner where Thermoplastic Urethane (TPU) padding is stacked on top of foam [72]. The TPU padding consists of five interconnected sections closest to the shell. TPU pads are air-filled with nylon spacer material inserts to maintain the pads' design shape. The foam is closest to the head, stacked on top of TPU pads [73].

The Riddell 360 Helmet has a modified facemask attachment, standard four-point chin strap attachment, and a foam liner [74]. Its modified facemask attachment is a four-point side mount with rubber grommets at the shell holes. Modified plastic connectors and quick-release bolts are also incorporated into the design. The Riddell 360 Helmet's liner is primarily composed of vinyl nitrile foam with a removable skull-cap like insert for the player's head. The liner design also incorporates more contact surface area to the front of the player's head than a traditional helmet liner design.

The Schutt Ion 4D Helmet a modified facemask attachment, an optional modified chin strap attachment, and a TPU liner in the form of engineered chambers [75, 76]. The modified facemask attachment of the Ion 4D is integrated into the helmet shell at one point on each side with a shock absorbing wedge and is attached to the top of the helmet

shell at two points using traditional facemask connectors [76]. The chin strap attachment includes two options: a standard four-point chin strap attachment and a modified four-point chin strap attachment. The modified chin strap attachment has the standard rear buckle attachment, while the top strap attachments are threaded though slots in the facemask and buckled in front and below the ear holes [76]. The Ion 4D helmet liner uses TPU padding in the form of engineered chambers. The Ion's liner design has various geometrical configurations of thin-walled TPU oriented perpendicular to the players head and the helmet shell.

The Xenith X2 Helmet has a standard four-point facemask attachment, a modified chin strap attachment, and a dampener-type liner system [77]. Its modified chin strap attachment has rear chin strap buckles that are connected to the helmet liner bonnet and then doubled back to connect to the rear of the shell. Front buckles are standardly mounted at the top-front sides of the shell. The X2 helmet's liner consists of dampener-type padding, where eighteen dampeners are connected by a polymer bonnet that fits around the head. The bonnet is then mounted to the helmet shell at four locations; the front, bottom rear, and one on each side. The dampeners are air-filled elastomeric cylinders with a pen-tip sized hole on top side adjacent to the shell. The dampeners have a thin layer of comfort foam, about 6.35 mm thick on the bottom of each cylinder, adjacent to the players head [77].

The Rawlings Quantum Plus, Riddell 360, Schutt Ion 4D, and Xenith X2 helmets as shown in Figure 5.2 each have synergistic design features that are difficult to quantify without understanding each component. Furthermore, these helmets would be difficult to rank without testing procedures that accounted for the entire response of each system.

The removal of the facemask during a NOCSAE drop test would adversely affect the response of each helmet system and in some cases not even account for these modified helmet design features. In the present study, these four helmets are used to assess the effect of adding the facemasks to the standard test method with the aim of trying to more accurately simulate real-play conditions by testing each helmet as one system.

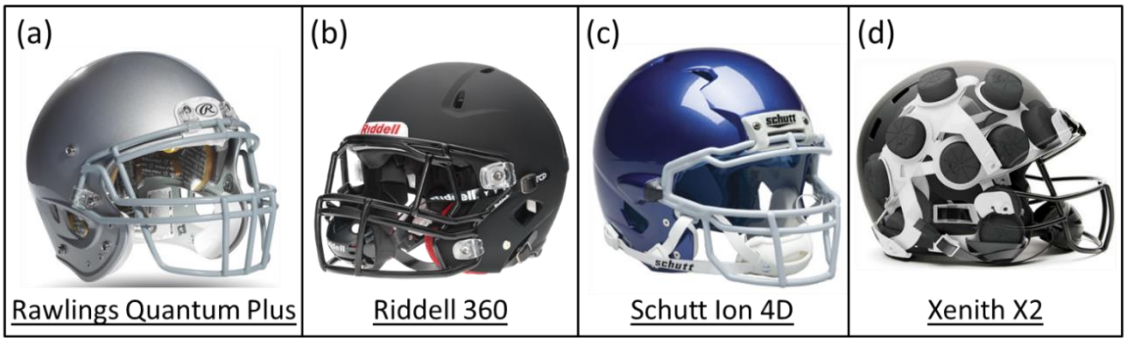

Figure 5.2 The four football helmet types used for impact testing showing; (a) Rawlings Quantum Plus [25], (b) Riddell 360 [34], (c) Schutt Ion 4D [35] and (d) Xenith X2 [30].

5.2 Methods

The NOCSAE standard drop test was modified with an aim of comparing individual football helmets and testing methods. The modifications to the drop tests included these differences:

1. A twenty four hour interval was used between each drop series to ensure helmet liner recovery that would minimize the preload.
2. An additional series of tests were conducted with the facemask connected to the helmet to more accurately replicate its constraints in more realistic playing conditions.

3. Two more drop orientations were included to quantify the facemask/shell joint response (Front Top and Front Top Boss).
4. The Head Injury Criterion (HIC) was added for analysis to more accurately account for the duration of resultant acceleration.
5. Maximum resultant acceleration was added for comparative analysis.
6. Three successive drop tests were performed for each impact scenario.
7. Time between successive impacts was 90 ± 15 seconds.
8. Helmets were tested at a 4.88 m/s impact velocity for all locations.

5.2.1 Procedure

The drop testing procedure required proper fitting of the helmet onto the large NOCSAE headform that was dropped in free fall onto a 12.7 millimeter (mm) thick Modular Elastomer Programmer (MEP) test pad attached to an anvil. The desired impact location was achieved by adjusting the headform's orientation and ensuring proper anvil positioning. Three consecutive drops were performed with a time interval of 90 ± 15 seconds for each helmet configuration in the NOCSAE standard locations: Front, Front Boss, Side, Rear, Rear Boss, and Top. Two additional drop locations were performed for each helmet configuration at what was deemed "Front Top" and "Front Top Boss" are shown in Figure 5.1.

Getting the proper helmet to headform fit was critical for the drop test procedures. Fitting of the desired helmet onto the headform required the correct size helmet and a properly adjusted chin strap fastened at all four locations. Helmet fitting was conducted according to the manufacturer's fitting instructions and NOCSAE procedures [76, 78-81]. The helmet and chin strap fit was checked prior to every drop test. Exchanging helmets

required slipping helmets on and off the headform while the headform remained attached to the drop carriage. Also care was taken to ensure that the test configuration was not altered during the exchange of helmets. All of the metrics that were employed to assess the relative safety were the peak accelerations, resultant accelerations, Severity Index (SI), and HIC values for each helmet system. The SI is based on the following equation,

$$SI = \int_0^T a(t)^{2.5}\, dt \tag{5.1}$$

where *a(t)* is the translational acceleration of the Center of Gravity (CG) of the head, and *T* is the acceleration duration [16, 17]. SI was calculated according to NOCSAE standards, where the calculation is limited by a 4 G threshold along the resultant acceleration curve. The HIC values were calculated by the following equation,

$$HIC = \left[(t_2 - t_1)\left\{\frac{1}{(t_2 - t_1)}\int_{t_1}^{t_2} a(t)dt\right\}^{2.5}\right]_{max} \tag{5.2}$$

where *a(t)* is the translational acceleration of the CG of the head, and t_1 and t_2 are the initial and final times, respectively, of the interval at which HIC attains a maximum value. All HIC values calculated in this study were HIC_{36}, where the duration of the time interval is limited to 36 milliseconds.

5.2.2 Instrumentation

A PCB Piezotronics Model 353B17 triaxial accelerometer (Depew, NY, USA) was securely attached at the headform's CG. The accelerometer was connected to Diversified Technical Systems, Inc. (Seal Beach, CA, USA) Tiny Data Acquisition Systems 2 (TDAS2) data acquisition (DAQ) module through a current source controller. Data from the DAQ module was processed by a Windows PC using TDAS software. The headform frame was attached to an electromagnetic release, controlled by a toggle

switch. The mechanical release switch was connected to the hardware trigger for the DAQ module. Upon testing, the switch was activated, simultaneously releasing the electromagnet and triggering a timed data acquisition of 0.040 seconds before activation and 1.15 seconds after activation. Calibration routines were conducted according to NOCSAE test standards. Instrument calibration was performed before any tests were conducted. The headform acceleration data was digitally collected at a rate of 16,512 samples per second with a 3300 Hz anti-alias filter. Calibration required drops of the desired test height onto a 76.2 mm thick Calibration MEP Pad. Three calibrations were consecutively performed and a fourth drop with the prior calibration data was conducted to check for consistency. Recalibration routines were conducted prior to change in impact velocity or impact orientation.

5.2.3 Data and Statistical Analysis

Data analysis was conducted by comparing acceleration-time plots and HIC, SI, and acceleration values between "with facemasks" and "without facemasks" cases (configurations) for each helmet type, impact velocity (related to drop height), and impact location. Mean differences and relative mean differences were calculated for comparison of HIC, SI, and acceleration values in respect to the NOCSAE standard ("without facemasks") configuration. Statistical analysis was piloted by an Analysis of Variance (ANOVA) method using least squares regression to fit general linear models. A four-way cross-class ANOVA was computed using impact velocity, facemask configuration, impact location and helmet type as classes, HIC, SI and Acceleration (G's) as dependent variables and mean squared error. The ANOVA employed a difference in least squares means procedure and type III sum of squares F-tests. These F-tests were used to evaluate

the significance of interactions between classes and for determining *p*-values. A 0.05 level of significance ($\alpha = 0.05$), an equal means null hypothesis ($\mu_1 = \mu_2$), and a difference between means alternative hypothesis ($\mu_1 \neq \mu_2$) were used for all statistical analysis. Significant four factor interactions ($p < 0.05$) were observed between impact velocity, facemask configuration, impact location and helmet type classes. Of these interactions, impact velocity was found to be the most significant followed by impact location, helmet type and facemask configuration, respectively. The model for ANOVA was then sliced in three groups; 1) helmet type, 2) impact location, 3) helmet type and impact location. A comparison between facemask configurations was thus allowed for each of these groups at each impact velocity using relative standard error and relative mean differences. The significance level of interactions, by ANOVA F-tests, can be found in Table A1 of the Appendix. All statistical analysis was performed using SAS 9.4 (SAS Institute, Cary, NC, USA).

5.2.4 Helmet Weights and Dimensions

The helmet shell plus liner and chinstrap, and the facemask plus attachment hardware (including bolts and connectors) were weighed then summed to give the total weight of each helmet. Also, a series of standardized dimensions were measured to define the helmet shells' length, width and height, and the length of the shell plus facemask. Measurements were obtained using CT scans of each helmet with the headform, as it was attached during drop testing. Length, width and height measurements were taken using points projected from the CG of the headform to points coinciding with the Frankfurt, Coronal, and Midsagittal anatomical planes, on the helmet shell and facemask. Width measurements were defined as a vector from the headform CG to a point on the side edge

of the helmet along an axis defined by the intersection of the Frankfort and Coronal planes. In the same manner, height and length measurements were taken along the Midsagittal plane. For example, height was measured from the headform CG to the top of the helmet shell along the axis of the Midsagittal-Coronal planes. The length measurements were taken from the headform CG to a point along the axis of the Midsagittal-Frankfort planes. "Shell Length" was measured in a direction towards the rear of the helmet while "Facemask Length" was measured in a direction towards the front of the helmet.

5.3 Results

Table 5.1 shows the weights of the helmet components and dimensions of the helmet shell and facemask (attached to shell) for each helmet tested. The average total weight of the helmets (including facemasks) was 1.89 ± 0.07 kg, where the facemask weighted 0.47 ± 0.08 kg and the shell, pads and chinstrap weighted 1.42 ± 0.08 kg. The facemask and its attachment hardware accounted for 33% (± 7) of the total helmet weight. Helmet size measurements were made as distances from the headform CG to the furthest points on the helmet (shell or facemask) coinciding with Frankfort, Coronal, and Midsagittal anatomical planes. The average dimensions of helmet shells were 15.2 ± 0.6 cm in length, 12.1 ± 0.5 cm in width and 16.2 ± 0.5 cm in height. The average facemask length (from the headform CG) was 17.5 ± 0.2 cm.

Table 5.1 Weights of the helmet "shell plus pads and chinstrap" and "facemask plus attachment hardware", and dimensions of the shell and facemask (attached to shell) for each helmet tested.

		Weight (kg)			Shell (cm)			Facemask (cm)
Helmet	Facemask	Shell + Pads + Chinstrap	Facemask + Hardware	Total	Length	Width	Height	Length
Rawlings QP	SO2R	1.45	0.52	1.97	16.0	12.1	16.8	17.5
Riddell 360	2BDCLW	1.45	0.49	1.94	15.1	11.6	16.3	17.8
Schutt Ion 4D	ROPO	1.49	0.35	1.84	14.6	12.8	16.1	17.2
Xenith X2	XRN22	1.30	0.52	1.82	14.9	11.9	15.6	17.5
	Avg	**1.42**	**0.47**	**1.89**	**15.2**	**12.1**	**16.2**	**17.5**
	sd	0.08	0.08	0.07	0.6	0.5	0.5	0.2

Note: Dimensions were measured as distances from the headform CG to points coinciding with Frankfort, Coronal and Midsagittal anatomical planes.

A total of 384 drop tests were recorded considering four helmet types with two facemask configurations, two impact velocities and eight impact locations. HIC, SI, and peak resultant acceleration (G's) values were calculated for three consecutive drops (90±15 seconds). Average HIC, SI, and acceleration results were plotted against impact location for the two impact velocities. Drop test results for helmet configurations "with facemasks" and "without facemasks" are shown in Figure 5.3; HIC versus impact location of 5.46 m/s (a) and 4.88 m/s (b) impact velocities, SI versus impact location of 5.46 m/s (c) and 4.88 m/s (d) impact velocities, and Peak G versus impact location of 5.46 m/s (e) and 4.88 m/s (f) impact velocities. In these plots, the results for each helmet in the NOCSAE standard configuration, "without facemask", is shown adjacent to the results of the same helmet "with facemasks". Error bars are displayed as maximum and minimum recorded values rather than standard deviations. Preliminary inspection of Figure 5.3 results indicated that there was substantial difference between facemask configurations for many of these three consecutive drop tests. It was also observed that the results were strongly dependent on helmet type, impact location and impact velocity.

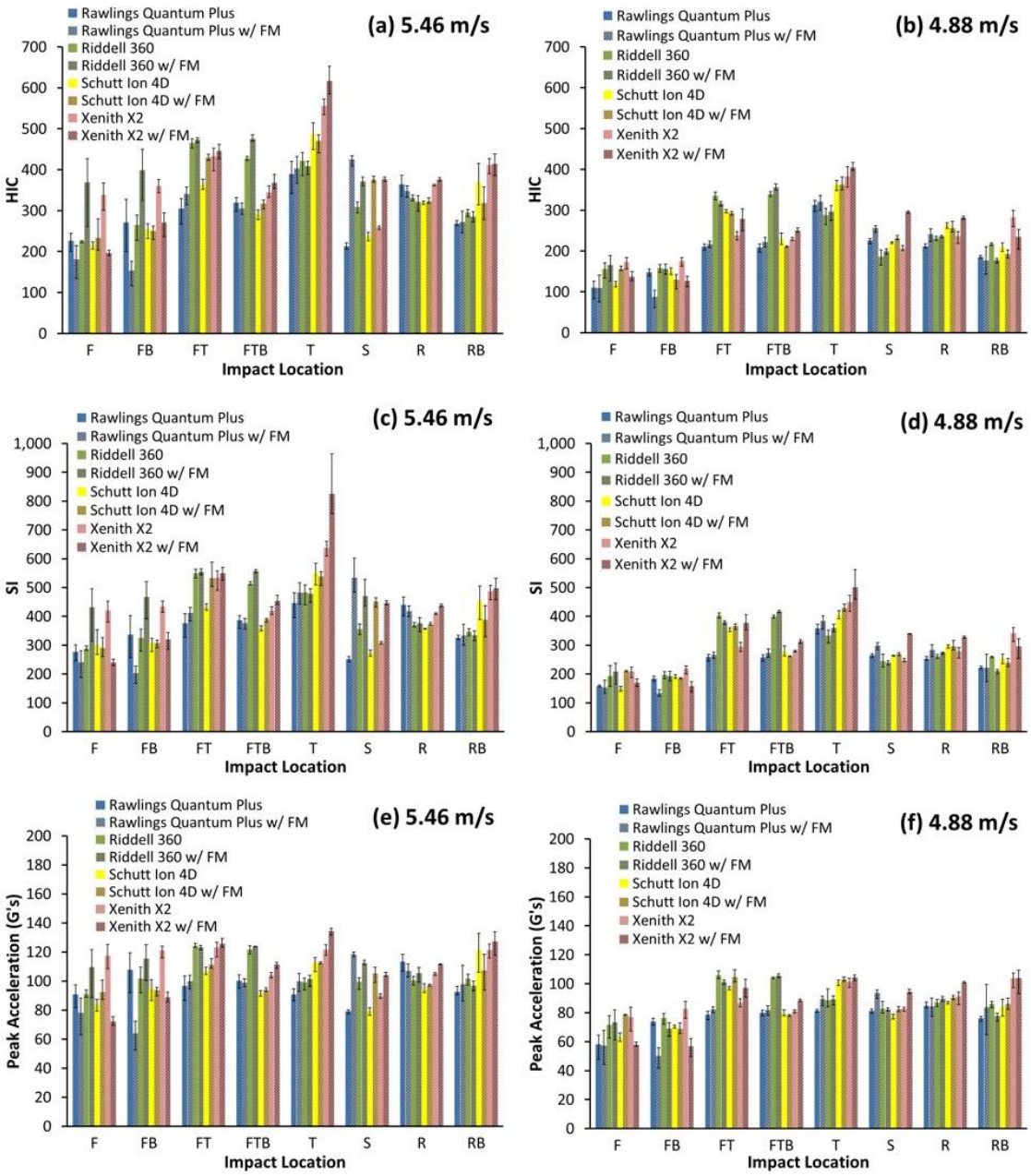

Figure 5.3 Drop test results for helmet configurations "with facemasks" (w/ FM) and "without facemasks".

(a), (c), and (e) show impact velocity results of 5.46 m/s, and (b), (d), and (f) show results for 4.88 m/s. Also (a) and (b) show HIC versus impact location; (c) and (d) show SI versus impact location; and (e) and (f) show peak acceleration versus impact location.

ANOVA F-tests diagnosed significant four-factor interactions ($p < 0.05$) between class variables. The largest of these variations were due to change in impact velocity

followed by impact location, helmet type, and facemask configuration, respectively (Appendix). ANOVA and mean difference procedures revealed significance between facemask configuration results. Table 5.2 shows a comparison of the signed Mean Difference (MD) and *p*-values in HIC, SI, and acceleration (G's) between facemask configurations for each helmet type, impact location and impact velocity, using standard error. MD is presented as signed values to indicate direction in reference to the NOCSAE Standard, "without facemasks", configuration. Statistically significant MD was observed ($p<0.05$), as indicated in bold font, most of which showed an increase in measured value (HIC, SI, and acceleration) for when the facemask was attached (positive direction). It was also observed in Table 5.2 that many significant MD's showed a negative direction, indicating a decrease in measured value for when the facemask was included.

Table 5.2 Comparison of the signed Mean Difference (MD) and P-values in HIC, SI, and acceleration (G's) for each helmet and each impact location when the facemask was attached in reference to the NOCSAE Standard, "without facemasks", configuration for 5.46 and 4.88 meters per second impact velocities.

		Rawlings QP				Riddell 360				Schutt Ion 4D				Xenith X2			
		5.46 m/s		4.88 m/s		5.46 m/s		4.88 m/s		5.46 m/s		4.88 m/s		5.46 m/s		4.88 m/s	
		MD	*p*-value	MD	*p*-value	MD	*p*-value	MD	*p*-value	MD	*p*-value	MD	*p*-value	MD	*p*-value	MD	*p*-value
F	HIC	-45.84	0.010	-0.60	0.973	143.91	<.001	10.53	0.552	17.34	0.327	36.07	0.042	-141.82	<.001	-36.12	0.042
	SI	-31.08	0.157	0.15	0.995	137.51	<.001	19.84	0.366	28.12	0.200	60.77	0.006	-173.14	<.001	-41.71	0.058
	G's	-12.74	0.006	-0.57	0.902	18.39	<.001	1.87	0.683	8.59	0.062	15.09	0.001	-45.42	<.001	-18.88	<.001
FB	HIC	-116.73	<.001	-51.54	0.004	133.93	<.001	-2.46	0.890	-3.32	0.851	-10.17	0.565	-89.23	<.001	-48.94	0.006
	SI	-131.35	<.001	-59.57	0.007	137.69	<.001	-9.90	0.652	-0.07	0.998	-1.58	0.943	-108.12	<.001	-58.45	0.008
	G's	-43.71	<.001	-20.81	<.001	13.84	0.003	-7.37	0.109	-0.88	0.847	-0.40	0.931	-32.34	<.001	-25.81	<.001
FT	HIC	35.54	0.045	6.10	0.730	8.35	0.637	-18.38	0.299	67.06	<.001	-5.14	0.771	12.13	0.493	40.64	0.022
	SI	37.09	0.092	-0.75	0.973	2.94	0.893	-31.04	0.158	79.47	<.001	7.29	0.740	20.81	0.343	89.38	<.001
	G's	3.62	0.430	3.53	0.441	-1.13	0.805	-4.41	0.337	4.65	0.311	7.71	0.094	2.60	0.571	10.45	0.023
FTB	HIC	-13.70	0.439	13.32	0.451	47.30	0.008	17.19	0.331	25.97	0.143	-17.94	0.311	23.00	0.194	21.39	0.227
	SI	-11.19	0.610	14.77	0.501	51.07	0.021	17.66	0.421	29.36	0.181	-16.72	0.446	34.21	0.120	31.74	0.149
	G's	-1.34	0.770	1.86	0.685	2.13	0.642	1.42	0.758	2.23	0.627	-0.97	0.832	7.40	0.107	7.52	0.102
T	HIC	13.60	0.442	8.47	0.632	-12.93	0.465	7.97	0.652	-16.20	0.360	0.47	0.979	61.00	<.001	21.37	0.227
	SI	34.53	0.116	24.44	0.266	-8.86	0.686	14.12	0.520	-14.18	0.518	13.50	0.538	85.12	<.001	20.55	0.349
	G's	9.13	0.047	8.19	0.075	2.34	0.610	0.76	0.868	-0.28	0.951	1.91	0.677	12.62	0.006	3.10	0.500
S	HIC	212.26	<.001	30.61	0.084	63.50	<.001	13.02	0.462	138.77	<.001	11.52	0.515	117.61	<.001	89.80	<.001
	SI	283.35	<.001	32.99	0.133	115.01	<.001	-5.66	0.796	177.97	<.001	6.11	0.781	138.44	<.001	91.90	<.001
	G's	39.32	<.001	12.50	0.007	13.16	0.004	-0.48	0.917	25.90	<.001	4.94	0.282	14.47	0.002	11.65	0.012
R	HIC	-16.55	0.350	29.73	0.094	-9.09	0.607	4.65	0.793	3.16	0.858	-7.52	0.670	13.90	0.432	44.27	0.013
	SI	-21.11	0.336	31.16	0.156	5.83	0.790	11.32	0.606	15.84	0.470	-0.29	0.989	28.27	0.198	49.01	0.026
	G's	-6.17	0.179	-0.13	0.977	5.02	0.274	2.69	0.558	3.14	0.493	3.28	0.474	6.60	0.151	9.61	0.037
RB	HIC	3.33	0.851	-8.20	0.643	-9.34	0.597	-38.65	0.030	-49.78	0.005	-16.62	0.348	2.53	0.886	-48.22	0.007
	SI	9.03	0.681	-1.71	0.938	-13.04	0.552	-44.41	0.044	-64.70	0.003	-10.93	0.618	10.45	0.634	-43.28	0.049
	G's	5.47	0.233	7.79	0.090	-4.78	0.298	-8.18	0.075	-13.95	0.003	1.98	0.667	5.98	0.193	0.11	0.981

*SE HIC = 12.49, SE SI =15.49, SE G's = 3.24

Note: Standard error was used for all HIC, SI and acceleration values*

Table 5.3 shows a comparison of the Relative Mean Difference (RMD) in HIC, SI, and acceleration values between facemask configurations for each helmet type at each impact velocity. RMD and relative standard error are presented as a percentage and calculated for each helmet type as an average across all impact locations (independent of impact location). For each helmet type, the higher impact velocity (5.46m/s) generally led to a larger RMD. The exception to this observation was seen with the Xenith X2 helmet in respect to HIC and SI. The highest RMD was observed for the Rawlings Quantum Plus helmet at the 5.46m/s impact velocity while the lowest RMD was observed for the Riddell 360 helmet at the 4.88m/s impact velocity.

Table 5.3 Comparison of the Relative Mean Difference (RMD) in HIC, SI, and Acceleration values for each helmet type when the facemask was attached in reference to the "without facemasks" configuration for 5.46 and 4.88 meters per second impact velocities.

Helmet	Impact Velocity (m/s)	HIC	SI	G's
		RMD	RMD	RMD
Rawlings Quantum Plus	5.46	23.52% (± 4.41)	24.16% (± 4.61)	16.34% (± 3.40)
	4.88	9.92% (± 6.73)	8.97% (± 6.96)	8.98% (± 4.28)
Riddell 360	5.46	19.61% (± 3.86)	17.73% (± 4.07)	7.72% (± 3.12)
	4.88	6.06% (± 5.69)	7.15% (± 5.95)	3.98% (± 3.75)
Schutt Ion 4D	5.46	14.12% (± 4.19)	15.57% (± 4.44)	8.21% (± 3.36)
	4.88	7.81% (± 6.01)	7.60% (± 6.28)	5.99% (± 4.01)
Xenith X2	5.46	17.12% (± 3.40)	18.37% (± 3.57)	14.03% (± 2.90)
	4.88	19.99% (± 5.50)	20.48% (± 5.75)	13.11% (± 3.71)

Note: RMD and relative standard error are presented as a percentage and calculated with respect to all tested impact locations.

RMD was also employed as a means of comparing the effect of the facemask attachment for each impact location. Table 5.4 presents a comparison of RMD in HIC, SI, and Acceleration values between facemask configurations for each impact location and each impact velocity. RMD and relative standard error are presented as a percentage and calculated independent of helmet type. In respect to impact location, the highest RMD was seen in the Side impact location, followed by Front and Front Boss impact locations, respectively. The lowest RMD were observed in the Top impact location.

Table 5.4 Comparison of the Relative Mean Difference (RMD) in HIC, SI, and Acceleration values for each impact location when the facemask was attached in reference to the NOCSAE Standard, "without facemasks", configuration for 5.46 and 4.88 meters per second impact velocities.

Location	Impact Velocity (m/s)	HIC	SI	G's
		RMD	RMD	RMD
F	5.46	33.54% (± 5.13)	28.31% (± 5.27)	20.77% (± 3.43)
	4.88	14.55% (± 9.24)	18.26% (± 9.49)	12.99% (± 4.86)
FB	5.46	29.92% (± 4.42)	27.16% (± 4.60)	20.44% (± 3.07)
	4.88	17.71% (± 7.91)	16.65% (± 8.07)	17.40% (± 4.28)
FT	5.46	8.69% (± 3.28)	8.3% (± 3.41)	2.78% (± 2.91)
	4.88	6.78% (± 4.76)	10.58% (± 5.02)	7.16% (± 3.56)
FTB	5.46	7.73% (± 3.68)	7.42% (± 3.82)	3.16% (± 3.13)
	4.88	7.16% (± 5.15)	7.02% (± 5.36)	3.55% (± 3.82)
T	5.46	5.22% (± 2.75)	6.4% (± 2.99)	5.76% (± 3.09)
	4.88	2.79% (± 3.76)	4.76% (± 4.07)	3.97% (± 3.51)
S	5.46	56.01% (± 5.00)	63.79% (± 5.30)	27.91% (± 3.76)
	4.88	17.35% (± 5.99)	13.54% (± 6.07)	9.11% (± 4.00)
R	5.46	3.03% (± 3.64)	9.40% (± 5.33)	4.43% (± 3.96)
	4.88	9.40% (± 5.33)	8.58% (± 5.71)	4.39% (± 3.71)
RB	5.46	4.63% (± 3.83)	11.81% (± 5.72)	5.84% (± 4.03)
	4.88	11.81% (± 5.72)	9.01% (± 6.09)	5.55% (± 3.75)

Note: RMD and relative standard error are presented as a percentage and calculated with respect to all helmet types tested.

Figure 5.4 presents NOCSAE drop test results of Rawlings Quantum Plus helmet "with facemask" versus "without facemask" at a 5.46 m/s Side impact. For all of these consecutive drop tests, a 50% increase in maximum resultant acceleration was observed when helmets were tested "with facemasks", as compared to the NOCSAE standard configuration. Figure 5.5 presents NOCSAE drop test results of Xenith X2 Helmet "with facemask" and "without facemask" at a 4.88 m/s impact velocity and a Top impact location. A change in acceleration-time profile was observed with a 40 G valley present in impacts "without facemask". This type of trend was also very pronounced in the higher velocity impacts for the Xenith X2 helmet. Figure 5.6 displays the NOCSAE drop test results of Rawlings Quantum Plus, Riddell 360, Schutt Ion 4D, and Xenith X2 Helmets

"with facemasks" at a 5.46 m/s impact velocity and a Front Top impact location. This new impact location has shown to have some of the highest peak acceleration values and a variety in acceleration-time history profiles across each helmet tested.

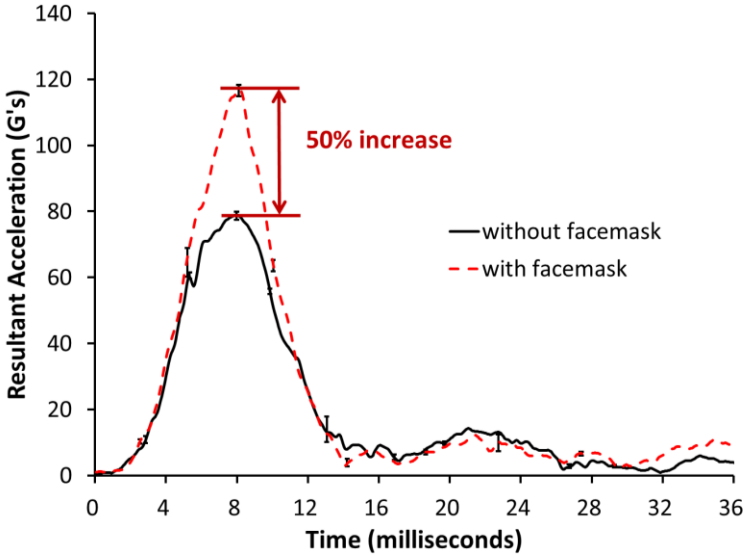

Figure 5.4 NOCSAE Drop Test (side impact) results comparing a Rawlings Quantum Plus Helmet "with facemask" and "without facemask" at an impact velocity of 5.46 meters per second showing a 50% increase in acceleration (G level) when compared to the standard ("with facemasks") case.

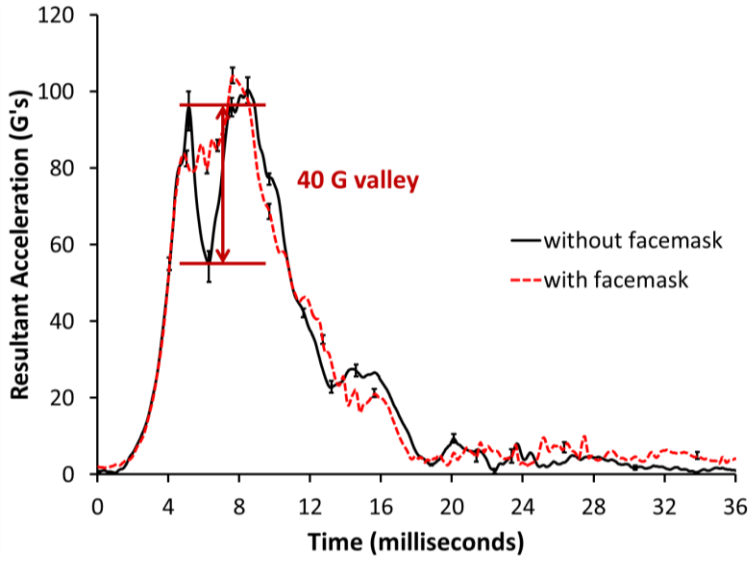

Figure 5.5 NOCSAE drop test (head top) acceleration-time history comparing the Xenith X2 helmet "with facemask" and "without facemask" at an impact velocity of 4.88 m/s.

Note: A 40 G drop in acceleration is present in the "without facemask" configuration.

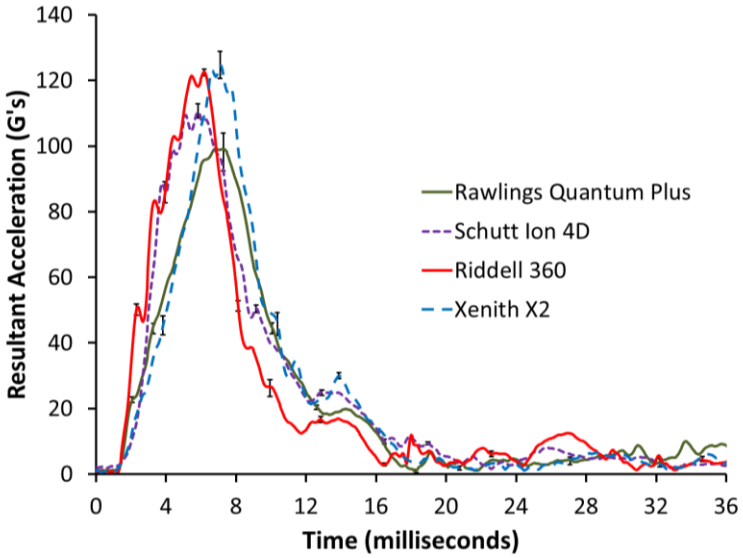

Figure 5.6 NOCSAE drop test (Front Top) results of Rawlings Quantum Plus, Riddell 360, Schutt Ion 4D, and Xenith X2 helmets "with facemasks" at a 5.46 meters per second, showing this new proposed impact location to have some of the highest peak acceleration values and a difference in acceleration-time history profiles across each helmet tested.

The limitations of this study include the following: (1) Drop tests were not conducted at 4.23 m/s and 3.46 m/s impact velocities, (2) The sample size was limited to one of each helmet, (3) The NOCSAE Standard drop test method cannot measure angular acceleration, (4) Tests were only performed under ambient temperature, (5) The size of all tested helmets was adult large.

5.4 Discussion

5.4.1 Helmets "With Facemasks" Versus "Without Facemasks"

Analysis of NOCSAE drop test results reveal significant differences ($p < 0.05$) for helmets "with facemasks", as compared to helmets in the NOCSAE Standard "without facemask" configuration. Comparison of the mean difference between facemask configurations for each helmet type, impact location and impact velocity (Table 5.2), shows statistical significance in 41% of all impacts for one or more measured values (HIC, SI and acceleration). The majority (62%) of these significant mean differences displayed an increase in measured value for when the facemask was attached (positive direction). It was also observed that many (38%) significant mean differences showed a negative direction, indicating a decrease in measured value for when the facemask was attached.

Significant helmet dependent variations were observed across impact locations and impact velocities. When the facemask was included, some helmets showed an increase in HIC, SI, and acceleration values at certain impact locations, while the same helmet showed a decrease in these values at other locations. In some cases, these trends tended to reduce the magnitude of a generalized difference in helmet response between facemask configurations. For instance, the 5.46 m/s drop test results of Xenith X2 helmet

(Figure 5.3) showed a decrease in HIC, SI, and acceleration values when the facemask was attached, for the Front and Front Boss impacts while other impact locations showed an increase in these values. These responses were helmet dependent and varied across impact location and impact velocity. Thus, generalized average values are not truly indicative of the individual helmet response with respect to change in impact velocity or impact location. For this reason Relative Mean Difference (RMD) was employed as a metric for comparison between facemask configurations. Calculated in respect to the "without facemasks" configuration, relative mean differences were used to analyze results in three groups; 1) Helmet Type, 2) Helmet Type versus Impact Location, and 3) Impact Location.

Since the NOCSAE standard SI limit has changed over time to increase safety, as discussed in the introduction these results comparing impacts "with facemasks" and "without facemasks" suggests another change is warranted. Although the current SI level of 1200 has not been reached in any of the experiments here, there was a significant SI level difference. For example, the Top impact on the Xenith X2 helmet showed an SI level increase of 85 (from 635 to 720) when the facemask was added. In this case, both levels were above a SI limit of 540, which is related to linear skull fracture. Another example is the Side impact of the Rawlings Quantum Plus helmet showed and SI level increase of 283 (from 251 to 534) when the facemask was added.

5.4.2 Helmet Type

When examining the interaction between facemask configuration and helmet type, the Rawlings Quantum Plus and the Xenith X2 helmets were generally the most affected by facemask attachment. Comparisons of relative mean differences between

facemask configurations for each helmet (Table 3) clearly show that the highest RMD values were seen in the Rawlings Quantum Plus helmet. Rankings of RMD reveal (Table A4) that the Rawlings Quantum Plus followed by the Xenith X2, Schutt Ion 4D and Riddell 360 helmets, respectfully, were most affected by facemask attachment.

In respect to HIC, SI and acceleration, inspection of Table 5.3 reveals that the Rawlings Quantum Plus helmet had the highest RMD for all 5.46 m/s impacts while the Xenith X2 had the highest RMD in all 4.88 m/s impacts. It was also observed that the higher impact velocity (5.46m/s) commonly led to a larger RMD. The exception to this observation was seen with the Xenith X2 helmet in respect to HIC and SI. The Xenith X2 helmet showed fairly similar RMD values for both impact velocities (5.46m/s and 4.88m/s), as compared to the Rawlings Quantum Plus, Riddell 360 and Schutt Ion 4D helmets. For this reason, the Xenith X2 had nearly twice the number of significant mean differences than any other helmet (Table 5.2). 60% of all Xenith X2 impacts were found to have a significant difference for when the facemask was attached. In reference to Table 5.2, all helmets were found to have significant MD while significance varied across helmet type impact location and impact velocity. In general, helmets with standard four-point facemask attachment, the Rawlings Quantum Plus and Xenith X2, were more affected by the facemask attachment than helmets with modified facemasks, the Schutt Ion 4D and Riddell 360. This implies that the standard four-point facemask attachment adds more of a stiffening kinematic constraint to the helmet shell than the modified facemasks.

5.4.3 Helmet Type Versus Impact Location

The Rawlings Quantum Plus, Riddell 360, Schutt Ion 4D and, Xenith X2 helmets each showed varying responses with respect to change to impact location and impact velocity when the facemask was attached. The variations between helmet responses could be attributed to the unique design features of each helmet tested, which include different liners, chinstrap attachments and faceguard attachment systems. Both helmets with standard four-point facemask attachment, Xenith X2 and Rawlings Quantum Plus, saw a large decrease in HIC, SI, and acceleration values (Table 5.2) when the facemask was attached at the Front and Front Boss impact locations. Xenith X2 showed the greatest decrease in HIC, SI, and acceleration values, 42%, 43% and 39%, respectively, in the Front impact location, when the facemask was attached (Table 5.2). Comparatively, the Rawlings Quantum Plus helmet saw a 20%, 13% and 14% decrease in HIC, SI, and acceleration for the same configuration. This decrease could possibly be credited to the modified chinstrap of the Xenith X2 helmet in conjunction with the constraints of the facemask attachment.

The attachment of the facemask during a helmet impact constrained the overall response of each helmet system tested and added a minor inertia effect. The facemask accounted for 33% (±7) of the total weight of the helmet systems tested. The facemask effect can change the helmet performance up to 50%, with respect to peak acceleration. As depicted in Figure 5.4, the 5.46 m/s drop tests of the Rawlings Quantum Plus helmet at a Side impact location shows a 50% increase in maximum resultant acceleration when the facemask was included. Correspondingly, the HIC increased by 100% and the SI

increased by 113% (Tables 5.2) when the facemask was added to the Rawlings Quantum Plus helmet for these series of drop tests.

A moderate change in acceleration-time profile arose when comparing tests "with facemasks" to tests "without facemasks", which is illustrated in Figure 5.5. Drop test results for the Xenith X2 helmet at a Top impact location and 4.88 m/s impact velocity show a 40 G dip, or valley, in acceleration when the facemask was not included. Due to the additional constraint that the facemask brings to the helmet shell, the acceleration dip was nonexistent for the same impact when the facemask was attached to the shell. More specifically, when the facemask was not included, the polycarbonate shell near the impact point could flex more and thus absorb more energy. When the facemask was included, the polycarbonate shell would not flex as much. On average, the HIC increased by 6%, the SI increased by 5% and the peak G increased by 3% (Tables 5.2) when the facemask was added to the Xenith X2 helmet for this drop setting. Similarly, this trend was shown to be very pronounced at the higher velocity impacts for the Xenith X2 helmet. In general, this type of change in acceleration profile could be responsible for increased HIC and SI values in the case that peak acceleration values would remain the same.

5.4.4 Impact Location

When examining the interaction between facemask configuration and impact location, the Side, Front, and Front Boss were, in general, the impact locations most affected by facemask attachment. The Side followed by the Front and Front Boss impact locations, respectively, resulted in the highest relative mean difference (Table 5.4) for each impact velocity and orientation tested. Thus these locations were the most affected by facemask attachment with respect to HIC, SI, and acceleration for all helmets tested.

While a significant mean difference ($p<0.05$) in HIC, SI, and/or acceleration was seen across each impact location for at least one helmet type (Table 5.2), all helmets saw significant mean differences in the Side and Front impact locations, when the facemasks were attached. When the facemask was added to 5.46 m/s Side drops, the HIC, SI, and acceleration values increased on average by 53.5%, 58.5% and 25.1%, respectively for all helmets. With respect to impact location, the Side impact experienced the largest increase in average HIC, SI, and acceleration values for 5.46 m/s drop tests. The Side impact was the third most dangerous for drops "with facemasks". Conversely, the Side impact was the least dangerous for drops "without facemasks".

Our results indicate that the NOCSAE Standard drop test methods should be modified to include facemasks during certification testing and include two more impact locations. Initial testing determined that the Front Top and Front Top Boss were better suited impact sites since they would impact the helmet shell rather than the facemask. During testing, the Riddell 360 and Rawlings Quantum Plus helmets experienced facemask damage at the Front and Front Boss locations, respectively. The facemask deformation was due to top bar of each facemask impacting the anvil, resultantly causing a stress concentration above the material's yield point. The facemasks were replaced and the helmets were inspected for further damage. The NOCSAE standard test method for football faceguards allows facemask replacement between individual drop tests and does not constitute this type of plastic deformation as a failure mechanism unless it makes contact with the facial region of the headform. As a result of this facemask failure, the Front Top, and Front Top Boss impact locations are proposed to replace the existing Front and Front Boss locations to accommodate for helmets "with facemasks". Our

results show that the Front Top and Front Top Boss impact locations generally yielded higher HIC, SI, and accelerations compared to the Front and Front Boss impact locations (Figure 5.3). An example of results for a Front Top impact location at a 5.46 m/s impact velocity "with facemasks" is presented in Figure 5.6. The replacement of these impact locations are further emphasized by the fact that our Front Top and Front Top Boss impact locations are identical to the Front and (Right) Front Boss impact locations of the NOCSAE standard for Lacrosse Helmets, which also include the faceguard for drop tests. These sites would be more realistic by allowing direct shell-liner impacts while still including the constraints of the facemask component.

5.4.5 Modified Helmet Test Method

We propose that facemasks should be included in the NOCSAE football helmet certification procedure. The results of this study show that it is important to test football helmets "with facemasks" as to simulate more realistic impact conditions. In order to change NOCSAE drop test procedure to include facemasks, some basic considerations must be addressed. These considerations are as follows;

1. An independent NOCSAE facemask integrity test would still be needed for facemask certification, unless the two test standards could be unified.
2. Front and Front Boss impact locations may need to be changed to match the Front Top and Front Top Boss impact locations.
3. The baseline model of a given football helmet should be certified with the baseline model facemask and advertised as so.
4. Any further change in facemask type should require further certification with the respective helmet model and size.

5. The results of individual helmet-facemask certifications should be advertised to increase player awareness.

Optionally, a merger could be made between NOCSAE football helmet and NOCSAE faceguard test standards. Since the facemask certification test impacts on the faceguard using a 3.2 mm thick MEP test pad while the helmet certification uses a 12.7 mm thick MEP test pad, the unification of these two test procedures would call for a MEP pad change for faceguard impact locations. Furthermore, the current Front and Front Boss impact locations could be tested as additional faceguard impact locations, with the 3.2 mm MEP and all other current NOCSAE faceguard standard test procedures. Front Top and Front Top Boss impacts could be tested with the 12.7 mm MEP test pad with all other NOCSAE football helmet standard test procedures.

Each helmet manufacturer typically has many models of facemasks from which the designs are normally specified for a given player's position. Some helmet manufactures also have facemask material options, which could bring additional weight variability within each facemask design. Similarly, many of the current facemask models are designed to fit multiple sizes of football helmets. Cosmetics have also recently become an additional vital factor in facemask weight variability. Heavier grill-type facemask designs, with more facemask bars, are becoming increasingly more dominant in football. These heavier faceguards shift the center of gravity of the athletes head and add an extra moment arm inducing a more deleterious torque during oblique helmet to helmet impacts. Thus, certifying each helmet model and size with each facemask option would more accurately define a helmet's impact attenuation capability by accounting for these variations. Finally advertising the results of these facemask-helmet certifications would

increase player awareness of their headgear as well as promote helmet manufacturer's design criteria to account for these various facemask options.

5.5 Summary and Conclusion

This study investigated the influence of the facemask component on football helmets during modified NOCSAE standard drop tests. Drop tests were performed on Rawlings Quantum Plus, Riddell 360, Schutt Ion 4D, and Xenith X2 helmets at eight impact locations and two impact velocities of 5.46 m/s and 4.88 m/s. During the testing process, NOCSAE standards were modified by adding the respective facemask for each helmet. Relative mean differences in HIC, SI, and maximum acceleration values of these helmets "with facemasks" and "without facemasks" allot the following conclusions to be drawn from the current investigation:

1. By including the facemask attached to the helmet, the peak acceleration measured at the center of gravity of the head increased by up to 50% (p <.001).
2. The Rawlings Quantum Plus, Riddell 360, Schutt Ion 4D, and Xenith X2 helmets each showed varying responses at different impact locations and impact velocities when the facemask was attached.
3. In general, the Side, Front, and Front Boss locations were most affected locations for impacts when the facemasks were attached.
4. NOCSAE Standard football helmet test procedures should be modified to accommodate for facemask attachment during testing.

The data collected from the NOCSAE standard drop tower show the helmet's energy absorption capability, and thus the headform acceleration was influenced by the facemask's placement. The current study postulates that certification testing of football

helmets should include the facemask and different impact conditions. To further account for the above changes two new impact locations, Front Top and Front Top Boss, must also be adopted. Comparative drop test results lead to the conclusion that in many cases the current NOCSAE standard test methods overestimate the helmet performance when compared to real playing conditions ("with facemasks"). The addition of the facemask during the NOCSAE Standard drop test procedure would more accurately simulate in-use conditions by testing the helmet as one system, therefore allowing the test method to account for evolution in helmet design. The present modified helmet certification tests by means of systematic testing procedures can serve as the origin of improved football helmet design criteria and increased player safety.

CHAPTER VI

FINITE ELEMENT ANALYSIS OF NOCSAE HEADFORM AND HUMAN HEAD

6.1 Introduction

This goal of this chapter was to use Finite Element Analysis (FEA) to create a linkage between helmet test standards, brain-injury metrics, and the mechanical response of the human brain. FEA simulations of National Operating Committee on Standards for Athletic Equipment (NOCSAE) drop impact tests were conducted on a helmeted NOCSAE headform model and a helmeted human head model. Correlations were made between both models relating localized brain response to global head acceleration. FEA simulations were experimentally validated by twin-wire drop tests of the helmeted NOCSAE headform using correlations for validation of the human head model.

6.1.1 Brain Injury Mechanisms

Brain injuries are classified into two main categories: diffuse injuries or focal injuries. Diffuse injuries range from a mild concussion (no loss of consciousness) to a cerebral concussion (immediate loss of consciousness) to axonal injury in the subcortical white matter [82]. Aside from diffuse injuries, focal injuries occur locally as either a hematoma or a contusion. Coup contusions typically occur in the brain adjacent to the skull at the impact site. Contre-coup contusions occur in the brain at the site opposite of the impact.

The dynamic mechanisms causing brain injuries are multifarious. There are two types of dynamic loading: contact or non-contact, each of which results in a different head response [82]. In this study only contact loading is investigated, since it is almost always the loading case in contact sports. Rapid contact loading produces stress waves that transmit through the brain by either linear accelerations or rotational effects. The dynamic mechanisms causing these brain injuries include deformation, relative motion, pressure waves, and pressure gradients. Coup contusions are typically induced by large compressive pressures while contre-coup contusions are dominated by hydrostatic tension (or negative pressure) [82] which pulls the material in a deleterious manner in three orthogonal directions [83]. The mechanical damage state of any solid material is a function of the hydrostatic tension in a hyperbolic manner and is a function of the maximum shear strain in a multiplicative manner [84]. As such, one might expect that if the contre-coup brain region exhibits the greatest tensile pressure, it would have the greatest mechanical damage there; however, we note that the maximum shear strain is also a variable, but not as strong as the greatest tensile pressure.

Several studies [59, 85-89] have used Finite Element Analysis (FEA) to examine brain deformations during dynamic impacts, though none of these have investigated the linkage between helmet test standards, brain-injury metrics, and the tensile pressure and shear strain of the human brain. Zhang *et al*. [86, 87], King *et al*. [59], and Viano *et al*. [89] studied brain deformation responses using dynamic inputs from reconstructed on-field impacts with the Wayne State University Head Injury Model (WSUHIM). Zhang *et al.* [87] and King *et al.* [59] found that a concentration of large principal strains were located in the midbrain, upper brain stem, and diencephalon for certain injury cases.

Viano *et al.* [89] demonstrated a migration of strain during impact and showed that the strain concentration in the midbrain correlated with memory and cognitive problems. Zhang *et al.* [86] demonstrated that large compressive intracranial pressures were initially at the site of impact (coup location) and the pressure gradient progressed to the opposite side (contre-coup site) with high tensile pressures. Their results showed that the largest shear stress magnitudes were located in the midbrain. These studies suggest that the brain's deformation should be correlated with the dynamic head impact. As depicted in Figure 6.1, the present study examines the relationship between the NOCSAE helmet test standards, brain-injury metrics, and brain response by utilizing FEA and NOCSAE drop tests.

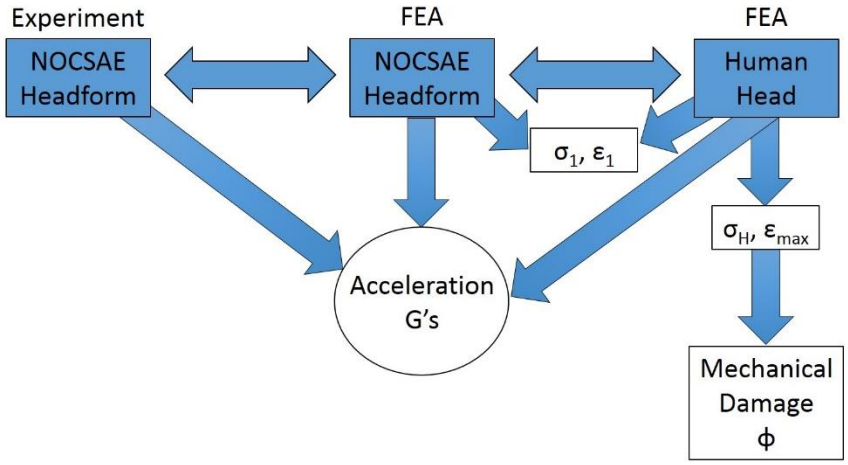

Figure 6.1 Flow chart showing the relationship between the NOCSAE headform experimental tests and Finite Element Analysis (FEA) of the NOCSAE headform and the human head.

Note: Each experiment and simulation are linked by the dynamic response (acceleration) while the NOCSAE headform human head simulations are linked by the mechanical response. The dynamic response and mechanical damage in the brain can be correlated.

6.1.2 Material Modeling of Brain Tissue

If accurate, material modeling of brain tissue can provide the safest most effective means for understanding concussion. While theoretically it would be ideal to conduct *in-vivo* studies to measure the local stresses and strains in the brain, technology and ethics limit these *in-vivo* studies. Knowing the material properties of the brain, determined from cadaveric tests and mechanical testing, a link between these properties and physiological outcomes can be made. In order to link the physiological outcome (e.g. brain damage) to concussion, it is important that the material behavior of the brain is accurately captured. Historically, the majority of brain material models have been elastic or visco-hyperelastic; however, Prabhu et al [90, 91] recently introduced an elastic, viscoelastic, viscoplastic, strain rate dependent internal state variable that captured several aspects of a brain's deformation. Prabhu *et al*. [90, 91] used Split-Hopkinson Pressure Bar (SPHB) experiments on porcine brain to calibrate the aforementioned MSU TP 1.1 material model and capture the elastic and inelastic material response of the brain undergoing high rate impacts. The model differs from the common spring-dashpot representation typically used to explain mechanical behavior in polymers, and instead uses physics based Internal State Variables (ISVs) to describe the current energetic state of the material. In the ISV model, a hierarchical multiscale approach was used to link deformation mechanisms at different length scales. The current study employed this mechano-physiological constitutive model material model (MSU TP 1.1) for FEA of the brain.

6.2 Methods

Three-dimensional FEA of a helmeted-human head and a helmeted-NOCSAE headform under NOCSAE drop test conditions were studied and experimentally validated. The FEA simulated impact conditions of the NOCSAE football helmet test standards, and were validated by NOCSAE drop tests using a twin-wire test device.

6.2.1 Impact Testing

Impact testing was performed using a twin-wire drop impactor device equipped with a size large NOCSAE headform. The NOCSAE headform is a synthetic head model designed to mimic the human head. The NOCSAE headform consists of an elastic outer layer, dense polymer layer, and a glycerin filled inner layer that simulates the skin, bone, and brain cavity, respectively [66]. The headform is instrumented with triaxial accelerometers at the center of gravity. The drop testing procedure required proper fitting of the helmet (if required) onto the large NOCSAE headform that was dropped in free fall onto a 25.4 millimeter (mm) thick Modular Elastomer Programmer (MEP) test pad attached to the anvil. The desired impact location was achieved by adjusting the headform's orientation and ensuring proper anvil positioning. The impact velocity was measured using a flag-gate velociometer in accordance to NOCSAE standards [17, 92, 93]. Three consecutive drops were performed with a time interval of 90 ± 15 seconds for Top and Front Top impact locations.

"Experimental calibration" drops were performed by impacting the unhelmeted NOCSAE headform onto the MEP test pad at an impact velocity of 3.46 m/s and a Top impact location. The acceleration trace, peak G, SI, and HIC were compared to that of a FE simulation performed under the same conditions. The calibration impact velocity was

chosen as it was the highest that could be comfortably performed without incurring damage to the headform. Typically NOCSAE "experimental calibration" drops are conducted using a 3" thick calibration MEP, while helmeted test drops are conducted using a lower durometer, 0.5" thick MEP test pad. In this study, the helmet impact tests and headform "calibration" drops were both performed on a 1" thick MEP test pad. The MEP deformation during impact was experimentally measured using carbon transfer paper. The carbon transfer paper was laid over a standard sheet of printer paper and set on top of the MEP prior to the calibration drops. The contact area between the headform and the MEP and the depth of penetration were measured. The amount of deformation of the MEP was inferred knowing the thickness and material properties of the headform scalp and assuming minimal deflection of the headform skull. The top impact location was chosen for headform validation impacts since it induces minimal angular momentum transfer into the wires of the twin-wire drop assembly.

The metrics employed to assess the dynamic response of the headform and human head were the peak resultant accelerations (G's), Severity Index (SI), and Head Injury Criterion (HIC) values. The SI is based on the following equation,

$$SI = \int_0^T a(t)^{2.5}\, dt \tag{6.1}$$

where *a(t)* is the translational acceleration of the Center of Gravity (CG) of the head, and *T* is the acceleration duration [18, 12]. SI was calculated according to NOCSAE standards, where the calculation is limited by a 4 G threshold along the resultant acceleration curve. The HIC values were calculated by the following equation,

$$HIC = \left[(t_2 - t_1)\left\{\frac{1}{(t_2 - t_1)}\int_{t_1}^{t_2} a(t)dt\right\}^{2.5}\right]_{max} \tag{6.2}$$

where *a(t)* is the translational acceleration of the CG of the head, and t_1 and t_2 are the initial and final times, respectively, of the interval at which HIC attains a maximum value. All HIC values calculated in this study were HIC_{36}, where the duration of the time interval is limited to 36 milliseconds.

6.2.2 Finite Element Analysis

FEA was conducted in ABAQUS explicit (Dassault Systèmes, Waltham, MA, USA) to model a helmeted NOCSAE headform and helmeted human head during impact conditions of twin-wire drop tests. Three-dimensional Finite Element meshes of the NOCSAE headform, football helmet, and a human head were developed using Computed Tomography (CT) and Magnetic Resonance Tomography (MRT). Both the NOCSAE headform and human heads were scanned wearing the same helmet type correctly positioned in the same manner as it would be for a drop test. Geometrical descriptions were obtained using ScanIP software package (Simpleware, Exeter, UK) and the tomography images. These images from scans were converted into masks which were divided into sections for each material.

The human head model consists of four material (tissue) layers; the brain, cerebrospinal fluid, skull, and surrounding tissue. The NOCSAE headform model consists of the simulated brain (glycerin), brain plastic surrounding the brain, skull (dense polymer), and surrounding tissue (elastic urethane). The material layers of each of these models are depicted in Figure 6.2. In addition to these head models, the default helmet for this investigation comprises a viscoelastic (polymeric) foam liner, a Glass Reinforced Polypropylene (GRPP) composite shell, and a magnesium facemask.

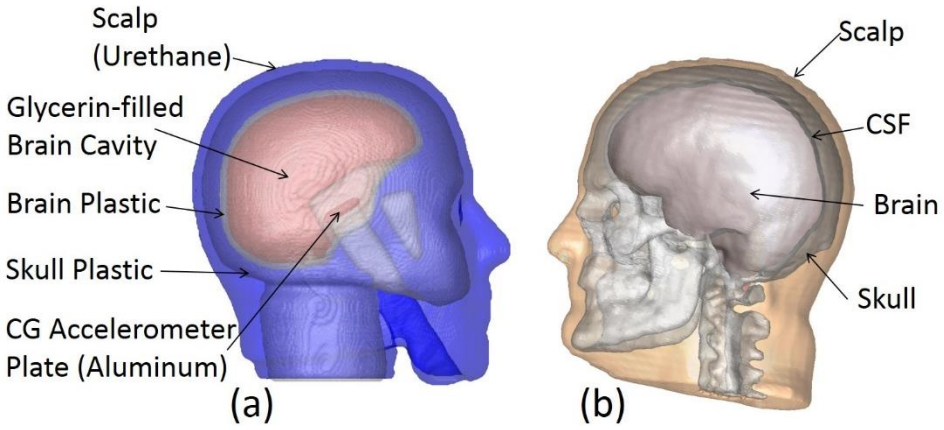

Figure 6.2 NOCSAE Headform (a) and Human Head (b) Finite Element models showing the material layers of each.

The human head with the helmet, the NOCSAE headform with the helmet, and the MEP were modeled as solid three dimensional, deformable structures. Symmetry was not used due to the asymmetrical loading conditions during oblique impacts. While not used in this study, these oblique impact locations are commonly used during NOCSAE helmet testing. All models were meshed with linear reduced integration hexagonal (C3D8R) and tetrahedral (C3D4) elements.

All materials were represented as homogeneous and isotropic. The material models and material properties are defined in Table 6.1. The material properties of the helmet, NOCSAE headform, and MEP test pad were experimentally obtained. The material parameters were calibrated by uniaxial compressive tests that were conducted on the cylindrical specimens of all aforementioned materials at a strain rate of 0.1/second. Densities and Poisson's ratios of these materials also were experimentally determined. The human head materials properties were obtained from the previous work of Prahbu et al. [90, 91] and from other literature [94-97]. The respective material models were

calibrated to experimental stress-strain data with its associated uncertainty and were verified by single-element FEA compression simulations of each material. Figure 6.3 shows the engineering stress-strain behavior of the NOCSAE headform, MEP, and helmet material model calibrations. Here, the material model calibration results are shown in engineering stress and engineering strain, since they are the required inputs into the respective constitutive models in ABAQUS. The uncertainty bands represent random experimental uncertainty with 95% confidence for three tests (n = 3) of each material. The brain material model was calibrated to experimental stress-strain data [90, 91] of porcine brain tissue at a strain-rate of 50 per second (see Appendix).

Table 6.1 Material characteristics used in the human head, NOCSAE headform, and football helmet models.

FE Model	Material		Material Model	Density ρ (tonne/mm^3)	Young's Modulus *E (Mpa)*	Poisson's ratio ν
Human Head	Scalp [94]		Linear Elastic	1.20E-09	16.7	0.42
	Skull Cortical Bone	[95, 96]	Linear Elastic-Plastic	1.80E-09	10000	0.22
	Skull Cancellous Bone	[95, 96]	Linear Elastic-Plastic	1.00E-09	390	0.19
	CSF		Linear Elastic	1.04E-09 [97]	0.299	0.496
	Brain		MSU TP 1.1	1.04E-09	-	-
NOCSAE Headform	Scalp	Polyurethane (PU)	Visco-hyperelastic	1.05E-09	-	0.48 [98]
	Skull	HDPE	Elastic-Viscoelastic	1.12E-09	-	0.425 [99]
	Inner Skull	Blow molded HDPE	Elastic-Viscoelastic	9.30E-10	-	0.425 [99]
	Brain Cavity	Glycerin	Linear Elastic	1.26E-09	26.1	0.499
	Accelerometer Plate	AL 6000 Series [100]	Linear Elastic	2.71E-09	69000	0.33
Rush Football Helmet	Facemask	AZ61 [101]	Linear Elastic	1.80E-09	45000	0.35
	Shell	GFRPP Composite	Linear Elastic	1.50E-09	-	0.272
	Liner	PU Foam Composite	Elastic-Viscoelastic	1.58E-10	-	-
Impact Surface	MEP Test Pad	Polyurethane	Elastic-Viscoelastic	1.05E-09	-	0.48

Note: GFRPP = Glass Reinforced Polypropylene.

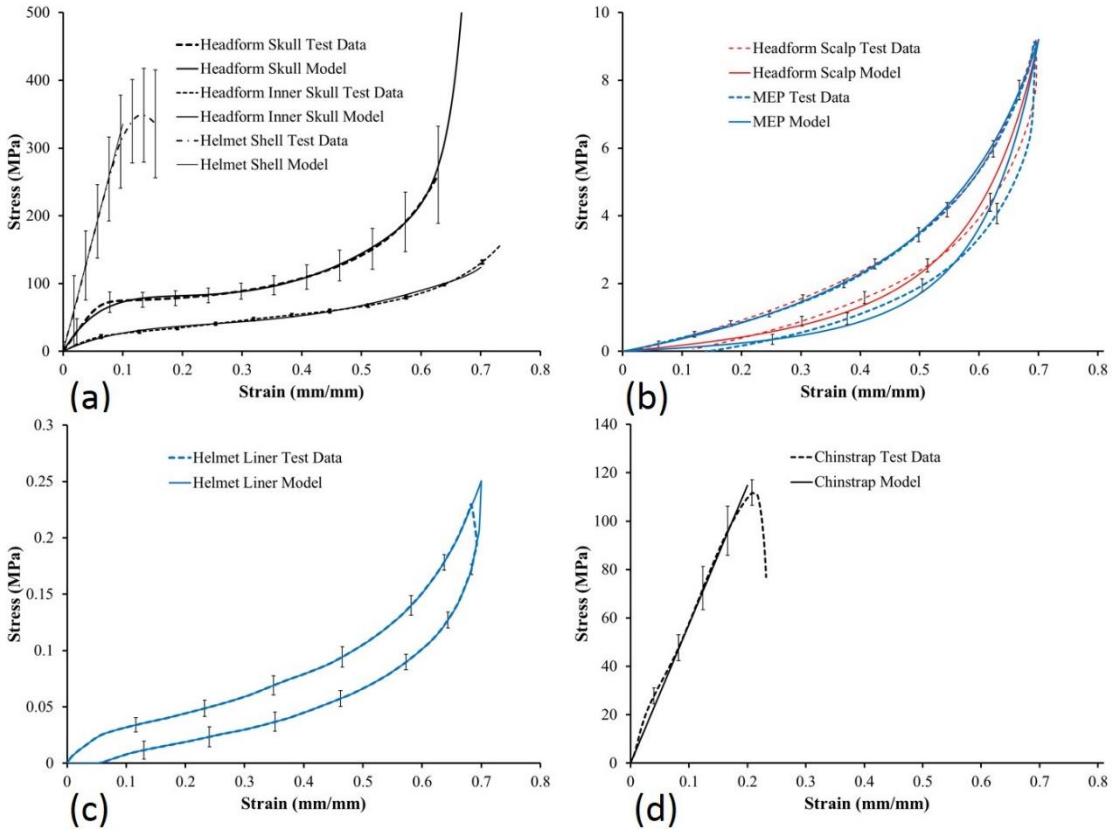

Figure 6.3 Stress-strain behavior comparing constitutive model calibrations of the NOCSAE headform, MEP, and helmet materials with experimental data.

The engineering stress-strain response is shown with uncertainty bands for (a) headform Skull (skull plastic), inner skull (brain plastic), and helmet shell, (b) headform scalp and MEP, (c) helmet liner, and (d) chinstrap test data and material models. The uncertainty bands represent experimental uncertainty with a 95% confidence interval (n = 3).

The propagation of error in the experiments was quantified using uncertainty. Uncertainties were assumed to adhere to a normal distribution with a 95% confidence interval. The main sources of uncertainties for the experiments conducted in this study include: random uncertainty due to sample-to-sample variations and microstructural incongruities; random uncertainties in the Instron 5869 test device and the NOCSAE drop tower; and systematic uncertainty (bias) due to measurement errors in the digital calipers, load cell (Instron), extensometer (Instron), accelerometers (NOCSAE drop tower), flag-

gate velociometer (NOCSAE drop tower), and digital weighing scale used for the density measurements. These random uncertainties are the result of precision limitations and the repeatability of test data. In contrast, systematic uncertainties are based on inaccuracies in the measurement and remain constant throughout each test. For the FEA simulations, other sources of uncertainty include numerical errors, model calibration errors, and errors related to the NOCSAE drop tower assembly.

6.2.2.1 The Football Helmet Model

The helmet used in this study was modeled using a Rush helmet [102] as the default. The football helmet model was created containing three components: the shell, the energy absorbing liner, and the facemask. Though not included in NOCSAE standard testing, the facemask was added to more accurately represent on-field impacts, as shown by Rush *et al.* [60]. The helmet liner consisted of polyurethane foam composite. The helmet shell was a glass reinforced composite (GFPP) with a polypropylene matrix. The facemask consisted of a magnesium alloy that mounted flush to the composite helmet shell. Material properties were characterized by mechanical testing. The helmet shell-facemask and liner-facemask intersections were constrained by tie constraints on the surface of the intersecting components. Frictional penalty interactions (tangential) were assigned to the liner-head intersections with a 0.1 coefficient of friction. This lower end coefficient value [103, 104] was selected because best matched test conditions where talcum powder was used to reduce friction in the liner-head interface during experiments. A "hard contact" property was assigned to the liner-head interactions in the normal direction. The facemask and the shell materials were modeled using linear elasticity in which moduli were determined from experimental compression tests. The liner was

modeled using the “Low Density Foam” material option in ABAQUS by fitting hysteretic compressive and tensile test data.

The four-point chinstrap retention system was included in the FEA model by using wire features to create a set of axial connector sections as depicted in Figure 6.4. The point load was dispersed by using kinematic constraints. Node sets were created for each of the four chinstrap-helmet mount locations with kinematic constraints on respective node sets of the chinstrap. The force-deflection relationship of the chinstrap (Figure 6.3d) was obtained by quasi-static tension tests from which a linear force-deflection relationship was applied to the connector section.

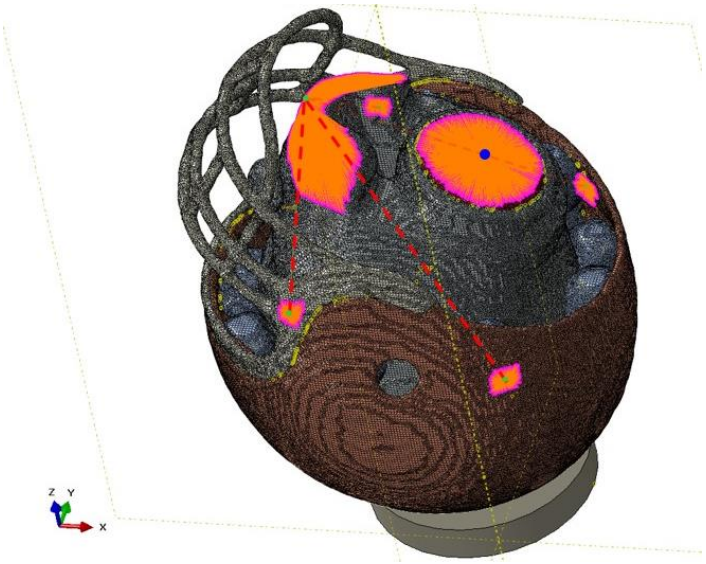

Figure 6.4 Helmeted NOCSAE headform model showing kinematic constraints of the four-point chinstrap retention system (and headform collar surface).

Four axial connectors (dashed red line) tied the chinstrap to the four chinstrap-helmet mount locations. Point loads of the chinstrap (green) and headform collar (blue) were kinematically constrained to local node sets.

6.2.2.2 The NOCSAE Headform Model

In this study, the large NOCSAE headform was modeled from CT imaging scans with the helmet attached. Material samples were obtained by performing a craniotomy on a decommissioned NOCSAE headform and extracting cylindrical samples by using a hole-saw bit and drill press. The headform scalp (urethane) was modeled in ABAQUS as a Hyperelastic material with Mullen's effect to quantify the viscoelastic hysteretic nature of the material. Lubricated cylindrical samples of headform urethane were tested in cyclic compression, input into the material model and best fit to an Ogden N=3 strain energy function (Figure 6.3b). Samples of the headform skull plastic and brain plastic were monotonically compressed until failure, and similarly best fit into an Ogden N=2, and Ogden N=3 Hyperelastic model, respectively. The aluminum accelerometer plate was assumed to be Al 6000 series and assigned material properties from the literature [100]. All headform material sections were constrained by tie constraints on the surface of the intersecting components. The NOCSAE headform coupler, located in the neck region, was fused (or merged) with the headform plastic skull. The NOCSAE headform sinus cavity, shown anterior to the CG accelerometer plate (Figure 6.2a), was also defined in the geometry.

6.2.2.3 The Human Head Model

The scanned human head mesh was originally smaller in size than the large NOCSAE headform, so scaling was used to eliminate the size factor variable. The human head size increased 5.25% to fit the NOCSAE headform dimensions as accurately as possible. This increase in the human head size was obtained by employing +CAD Software (Simpleware, Exeter, UK), from which it was scaled for mask generation. Once

the masks were generated, they were imported into the ScanIP model where they were rotated and translated into the three-dimensional helmet mesh by alignment with the existing NOCSAE headform mask. Nearest neighbor interpolation was used for all mesh manipulations. The scaled human head mesh fit within 1 pixel (1 mm) of the NOCSAE headform model, as measured from locations on the anterior-posterior (front to back), and lateral-medial (sides) directions. In order to compensate for the difference in head mesh and headform mesh curvature, the liner was dilated until contact was made with human head mesh. Cervical vertebrae of the FEA mesh were fused since the scope of this study was to compare the human head and NOCSAE headform during linear impacts via the NOCSAE standard drop tests. The cortical and cancellous bone regions of the skull were segmented and assigned their respective properties [95, 96] . Bone was modeled as a linear elastic-plastic material in ABAQUS. Due to image resolution limitations, the brain was geometrically defined as a single section using average properties of gray and white matter [*c.f.,* Prabhu *et al* [90, 91]]. The brain constitutive material model (MSU TP 1.1) was input in ABAQUS as a user defined VUMAT. The CSF was modeled as a linear elastic material. The CSF's Young's modulus was calculated from the Bulk modulus [97] and assigning a very high Poisson's ratio due to the incompressible nature of the fluid. The scalp was modeled as a linear elastic material with properties obtained from literature [94]. Tie constraints were assigned to the surface of the intersecting components for all human head material sections.

6.2.2.4 Modeling the Twin-wire Test Device

The NOCSAE twin-wire drop arm assembly was modeled as an inertia point located on a point coinciding with the middle of the headform collar assembly. This point

was dispersed by using a kinematic constraint on the collar/neck surface. The drop arm assembly was modeled using SolidWorks software (Dassault Systèmes, Waltham, MA, USA). The density of aluminum was 2.71 g/cc [105], and the drop arm assembly had a total mass of 2.3 kilograms. Inertia properties were calculated and translated to a point coinciding with the middle of the headform collar assembly and a corresponding point on the C7 cervical vertebrae of the human head model, as depicted in Figures 6.5 and 6.6. The point load was dispersed by using applying kinematic constraints to node sets at the free end of the headform collar and human head neck.

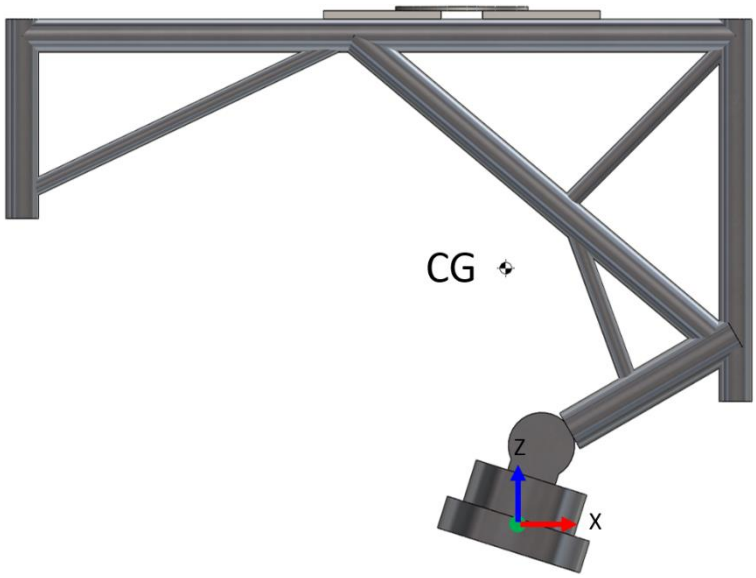

Figure 6.5 CAD model of NOCSAE twin-wire drop arm assembly showing the calculated center of gravity (CG) and the origin at headform collar attachment location.

Note: Moment of inertia was calculated with respect to the origin.

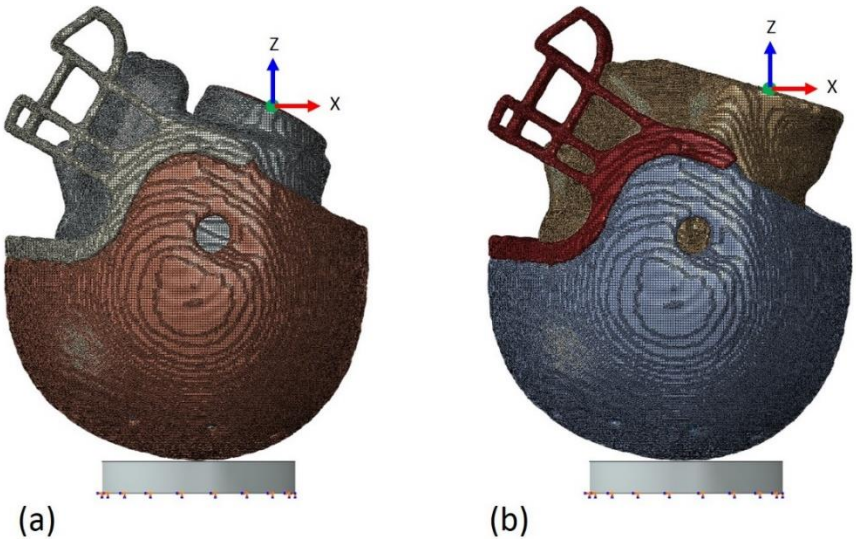

Figure 6.6 NOCSAE headform (a) and human head (b) finite element models at top impact location orientation showing the origin of where the drop arm point mass/inertia was added.

The MEP impact surface was modeled in ABAQUS as a Hyperelastic material with Mullen's effect to quantify the viscoelastic hysteretic nature of the material. Lubricated cylindrical samples of the MEP test pad were tested in cyclic compression, inputted into the material model, and used to calibrate an Ogden N=3 strain energy function. Encastere boundary conditions were applied to the opposite side of impact of the MEP. "Hard contact" and frictional penalty properties were assigned for all contact surfaces with the MEP. A 0.2 coefficient of friction was applied for tangential contact properties.

6.2.2.5 Loads and Boundary Conditions

In the initial step of the simulations, the headform/headform helmet combination were given an initial velocity by adding them to a predefined field and were placed 1 mm away from the MEP impact surface. The models were rotated into the impact location

position and translated to a position within 1 mm of contact with the MEP. A predefined velocity field was applied to the helmeted head in the negative Z direction (00-1 direction), while the MEP pad remained stationary by the encastere boundary conditions at the anvil location. While experimental tests were conducted at 3.46 and 5.46 m/s, the prescribed velocity field in the simulations were adjusted to account for the 12.5 mm distance from the end of the flag-gate velociometer trigger to headform/helmet contact with the MEP. The impact location angles were measured using an inclinometer and an angle protractor, and the MEP contact distance was measured using a depth gauge. Boundary conditions allowing no rotational displacement were applied to node sets at the free end of the headform collar and human head neck. This boundary condition was aimed to simulate flexure in the wires of the twin-wire device during impact by allowing translational displacements in all directions while not overconstraining the assembly.

6.2.2.6 Data Analysis

Data analysis was conducted by comparing the acceleration-time plots, HIC, SI, and peak acceleration values between experiments and simulations for six impact cases. The impact cases were the following: Case 1) 3.46 m/s top impact without helmet, Case 2) 3.46 m/s top impact with helmet, Case 3) 3.46 m/s Front Top impact without helmet, Case 4) 3.46 m/s Front Top impact with helmet, Case 5) 5.46 m/s Top impact with helmet, and Case 6) 5.46 m/s Front Top impact with helmet. The average HIC, SI, and acceleration values of three consecutive drops were calculated for each experimental test series. The intracranial mechanical response variables were calculated for all simulations. The maximum principle shear stresses and the maximum principle strains, the coup

pressure (compressive) and the contre-coup pressures (tensile) were extracted by use of a Python code.

The probability of a concussion was calculated for all available dynamic mechanical response variables and compared to the six impact cases. Table 6.2 [85] displays a summary of proposed dynamic-based and brain-deformation brain injury thresholds. Assuming an injury case is one that exceeds these dynamic thresholds, namely peak acceleration, HIC, and SI, important observations are made in this study regarding these injury criteria, pass/fail limits of helmet test standards, and relations between the NOCSAE headform and the human head. The most conservative concussion probability limits were used that were available for all criteria. The 50% concussion probabilities for peak acceleration, HIC, and SI from Newman *et al.* [40, 106], principal shear stress and principle strain from Zhang *et al*. [86], and the peak pressures from Kleiven *et al.* [88], were combined and compared to experiment and simulation results. In this study, a "concussion case" was assumed if values for peak acceleration, HIC, SI, intracranial pressures, principal shear stresses, and/or principle strains exceeded these limits. Specifically, Newman et al. [40, 106] indicated that a 50% probability of concussion would occur at accelerations above 77 G's, HIC values above 239.8, and/or SI values above 291.2. Kleiven et al. [88] stated that a 50% probability of concussion would occur at tensile pressures below -55 KPa, and/or compressive pressures above 68.5 KPa. Zhang et al. [86] claimed that a 50% probability of concussion would occur with intracranial and shear stresses above 7.8 KPa and/or principal strains above 0.19.

Table 6.2 Dynamic-based and brain deformation-based probabilistic thresholds for concussion.

	Probability	Peak G	HIC	SI	P_{tens} (kPa)	P_{comp} (kPa)	$\tau_{1\,max}$ (kPa)	$\varepsilon_{1\,max}$	VMS (kPa)	SR (s^{-1})	SSR (s^{-1})
Newman et al. [40, 106]	50%	77	239.8	291.2	-	-	-	-	-	-	-
	95%	115	485.2	558.9	-	-	-	-	-	-	-
Pellman et al. [34]	Nominal	-	250	300	-	-	-	-	-	-	-
King et al. [59]	25%	57	136	-	-	-	-	-	-	46	14
	50%	79.3	235	-	-	-	-	-	-	60	19
	75%	98.4	333	-	-	-	-	-	-	80	24
Zhang et al. [86]	25%	66	151	-	-41	61	6	0.14	-	-	-
	50%	82	240	-	-	-	7.8	0.19	-	-	-
	80%	106	369	-	-	-	10	0.24	-	-	-
Broglio et al. [107]	Nominal	96.1	-	-	-	-	-	-	-	-	-
Zhang et al. [87]	25%	-	-	-	-	-	-	0.25	-	46	14
	50%	-	-	-	-	-	-	0.37	-	60	19
	75%	-	-	-	-	-	-	0.49	-	80	24
Kleiven et al. [88]	50%	-	-	-	-55	68.5	-	0.21	8.4	-	-

From left to right, peak linear acceleration (G's), Head Injury Criterion (HIC), and Severity Index (SI) dynamic thresholds, and maximum values of intracranial tensile pressure, compressive pressure, principle shear stress, principle strain, Von Mises stress, strain rate, and the product of strain and strain rate [85].

6.3 Results and Discussion

The helmet and head FEA models were calibrated with uncertainty using stress-strain data for each material. Table 6.1 and Figure 6.3 describes the material properties used in the NOCSAE drop FEA simulations. Table 6.1 shows the material characteristics of the human head, NOCSAE headform, football helmet, and MEP impact surface models with material descriptions, the material (constitutive) model, density, Young's Modulus, and Poisson's ratio used for the FEA simulations. Human head material properties were determined from the literature (Table 6.1) and from previous work by Prabhu *et al*. [90, 91] while the NOCSAE headform, football helmet, and MEP properties were experimentally determined. Figure 6.3 depicts results of these quasi-static mechanical tests showing the stress-strain behavior of these mechanical tests with uncertainty compared to constitutive model calibrations of the (a) headform skull (skull plastic), inner skull (brain plastic), and helmet shell, (b) headform scalp and MEP, (c)

helmet liner, and (d) chinstrap materials. The uncertainty bands represent the systematic errors in the stress levels with 95% confidence. Material model calibration (Figure 6.3) showed that the constitutive material models were well correlated to the experimental data and fit well within the uncertainty bands. The stress-strain behavior of the headform scalp (polyurethane) and the MEP test pad were nearly identical indicating that they were of similar durometer.

Table 6.3 displays the physical structure and finite element composition of the human head, NOCSAE headform, and football helmet models. Weights and volumes of the model sections are portrayed with totals for the human head, helmeted human head, headform, and helmeted headform. The NOCSAE headform model and the human head model showed physical differences. Mass properties of the human head and NOCSAE headform (Table 6.3) show that the human head model was 1.17 Kg heavier than the NOCSAE headform. The total weight of the human head was 7.20 Kg, while the total weight of the NOCSAE headform was 6.03 Kg. The head-size of both models were very similar. The human head was scaled to fit the headform within a 1 mm diameter in the Anterior-Posterior, and Lateral-Medial directions, leaving the differences in liner material minimal between helmeted-head models.

Table 6.3 Human head, NOCSAE headform, and football helmet physical structure and Finite Element models.

FE Model	Material	# of Elements	# Hex Elements	# Tet Elements	Mass (Kg)	Volume (cm^3)
Human Head	Scalp	1141267	174456	966811	3.23	2688.06
	Skull Cortical Bone	696987	62522	634465	1.85	1026.44
	Skull Cancellous Bone	50781	38467	12314	0.33	326.49
	CSF	318144	9878	308266	0.29	279.99
	Brain	309811	56252	253559	1.50	1444.45
	Head Total	2516990	341575	2175415	7.20	5765.43
Rush Football Helmet	Facemask	131405	6562	124843	0.25	139.30
	Shell	807338	49349	757989	1.48	989.15
	Liner	868990	145423	723567	0.32	2041.54
	Helmeted Head Total	4634534	599161	4035373	9.25	8935.42
NOCSAE Headform	Scalp	855707	115450	740257	1.74	1658.03
	Skull	784604	167966	616638	2.82	2516.52
	Inner Skull	258762	18335	240427	0.27	287.75
	Brain Cavity	233080	47546	185534	1.18	938.69
	Accelerometer Plate	3821	660	3161	0.02	6.61
	Headform Total	2135974	349957	1786017	6.03	5407.61
Rush Football Helmet	Facemask	130686	6742	123944	0.25	138.94
	Shell	814591	51792	762799	1.52	1014.27
	Liner	825898	140483	685415	0.30	1924.43
	Helmeted Headform Total	3910970	549634	3361336	8.10	8485.26
Impact Surface	MEP Test Pad	2716	2716	0	0.49	463.33

Note: All elements are solid elements.

Figures 6.5 and 6.6 define the loading and boundary conditions of the twin-wire tests device. Figure 6.5 illustrates the created CAD model of NOCSAE twin-wire drop arm assembly and indicates the locations of the calculated Center of Gravity (CG) and the origin at headform collar attachment location (indicated by the triad). Total weight of the twin-wire drop arm assembly was 2.3 Kg. Figure 6.6 shows the corresponding origin point on the headform and human head models, which the point mass/MOI of the drop arm was applied. Both helmeted models are shown in Figure 6.6 oriented in a Top impact location with a distance of 1 mm from the MEP at the initial step of the simulations.

Figure 6.7 shows resultant acceleration-time history of experimental validation for the "without helmet" cases. Here, time-shifted acceleration traces of NOCSAE headform experiment (with uncertainty at 95% confidence level) and simulation are depicted with a

comparison to human head simulation for 3.46 m/s Top impacts (Figure 6.7a) and Front Top impacts (Figure 6.7b). In Figure 6.7a, the Top impact location showed the best fit for the headform simulation within the uncertainty bands of the headform experiment. Similar magnitudes of peak acceleration were observed for both the headform experiment and headform simulation while the experiment resulted in a slightly shorter impact duration (pulse width). The human head simulation shows a very similar acceleration response to that of the headform simulation for this impact location. The acceleration response for the headform experiment shows post-impact sinusoidal residual noise at a frequency of 200 Hz, presumably due to a resonance in the twin-wire test device. Becker *et al*. [108] studied guided fall impact devices showing that a matching residual in the accelerometer trace is due to a 200 Hz resonance in the twin-wire drop-arm. This residual noise is observed in the FEA simulations because the twin-wire drop-arm was modeled as a point mass rather than a geometric description. In Figure 6.7b, the acceleration response of the headform experiment and headform simulation shows a similar shape but a different magnitude and pulse width for the Front Top impact location. Here, the headform experiment shows a greater acceleration magnitude and shorter pulse width than either the headform or head simulations. The headform and human head simulations show similar magnitudes in the peak acceleration while the human head shows rotations due to differences in skull geometry and bending in the neck fissures.

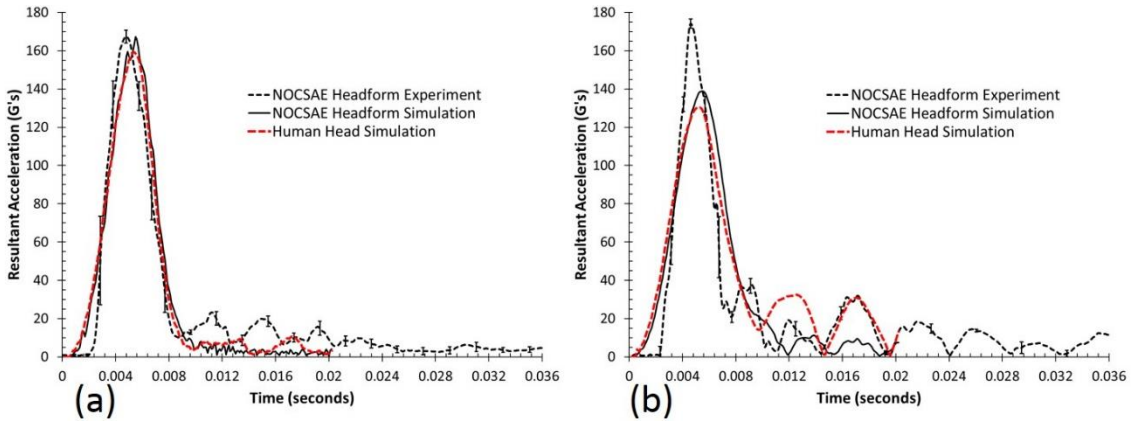

Figure 6.7 Experimental validation (without helmet) of NOCSAE headform model and comparison of human head model showing the CG resultant acceleration-time history with uncertainty of each at a 3.46 m/s Top impact (a) and Front Top impact (b).

Note: The uncertainty bands represent experimental uncertainty with a 95% confidence interval (n = 3).

Figure 6.8 displays validation simulation results showing pressure distributions of the NOCSAE headform during the 3.46 m/s Top impact without the helmet, as shown from a mid-sagittal cut view. Similarly, Figure 6.9 displays the pressure distributions for the human head model during the 3.46 m/s Top impact validation simulation. Here, the human head model experienced lower pressures as compared to the NOCSAE headform simulation in Figure 6.8. The highest pressures are observed for the headform and the human head at the simulation times of four milliseconds (t = 4 ms) and six milliseconds (t = 6 ms). These times correspond to the times of peak acceleration, as shown in Figure 6.7a.

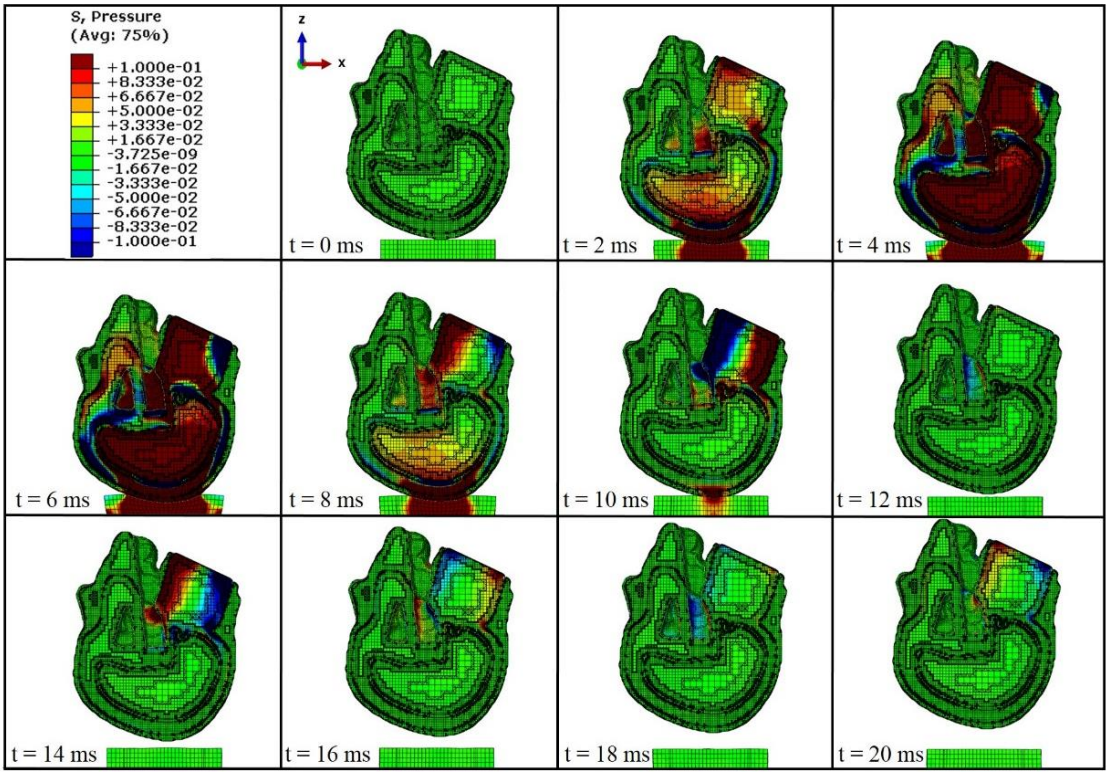

Figure 6.8 Validation simulation results showing pressure distribution of the NOCSAE headform model (mid-sagittal view) during a 3.46 m/s Top impact without the helmet.

Note: Pressure distributions are shown in MPa for two millisecond intervals during the twenty millisecond simulation.

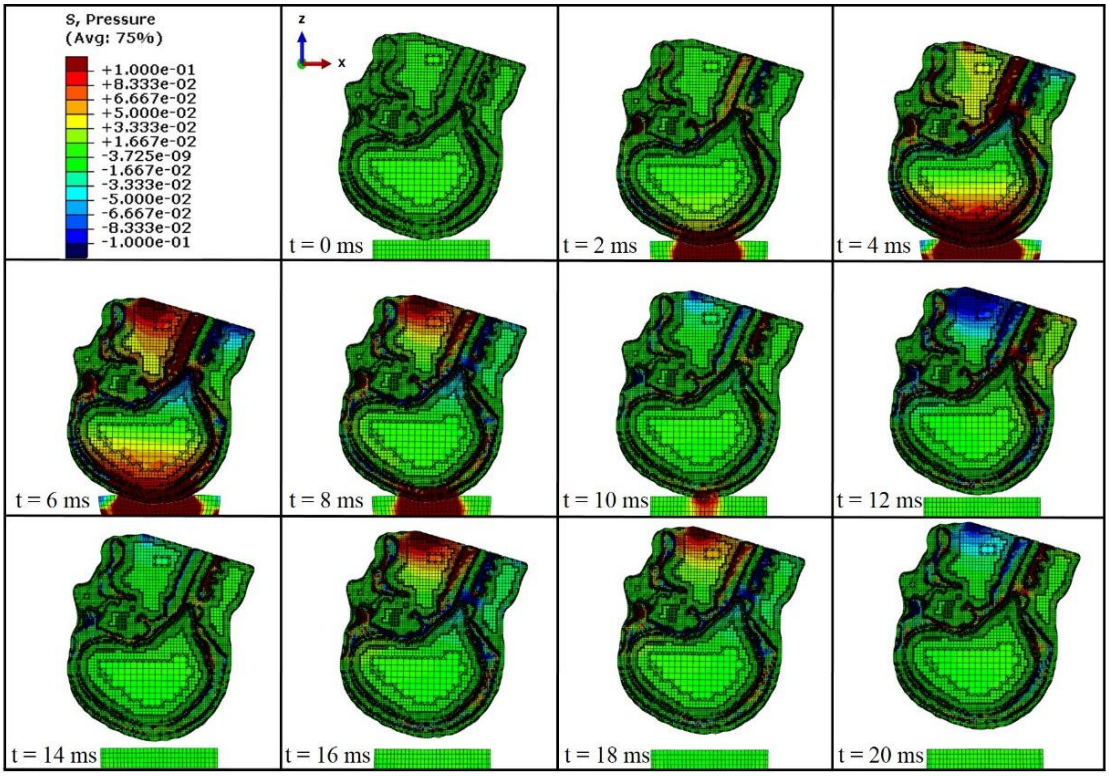

Figure 6.9 Validation simulation results showing pressure distribution of the human head (mid-sagittal view) during a 3.46 m/s Top impact without the helmet.

Note: Pressure distributions are shown in MPa for two millisecond intervals during the twenty millisecond simulation.

Figure 6.10 displays the intracranial pressure distributions of the human brain during the 3.46 m/s Top impact validation simulation without the helmet. Here, the pressure distributions in the human brain are displayed on a scale bounded by 25% concussion probabilities for tensile pressure and compressive pressures [86]. Compressive pressures above this probabilistic threshold are displayed in dark red, while tensile pressures above this threshold are displayed in dark blue. At the simulation time of four milliseconds (t = 4 ms), the human brain experienced the greatest compressive pressures at the site of impact (shown in dark red), between the frontal and parietal lobes. At six milliseconds (t = 6 ms), the greatest tensile pressures (dark blue) were observed in

the brain stem and cerebellum. A concussion-level impact to the cerebellum would result in loss of balance and coordination while the brainstem is responsible for controlling autonomic functions, such as breathing, heart rate and temperature regulation. After the CG acceleration pulse (after t = 10 ms), the tensile pressure propagated to the frontal lobe at t = 12 ms, then to the brain stem, cerebellum and occipital lobe at t = 16 ms.

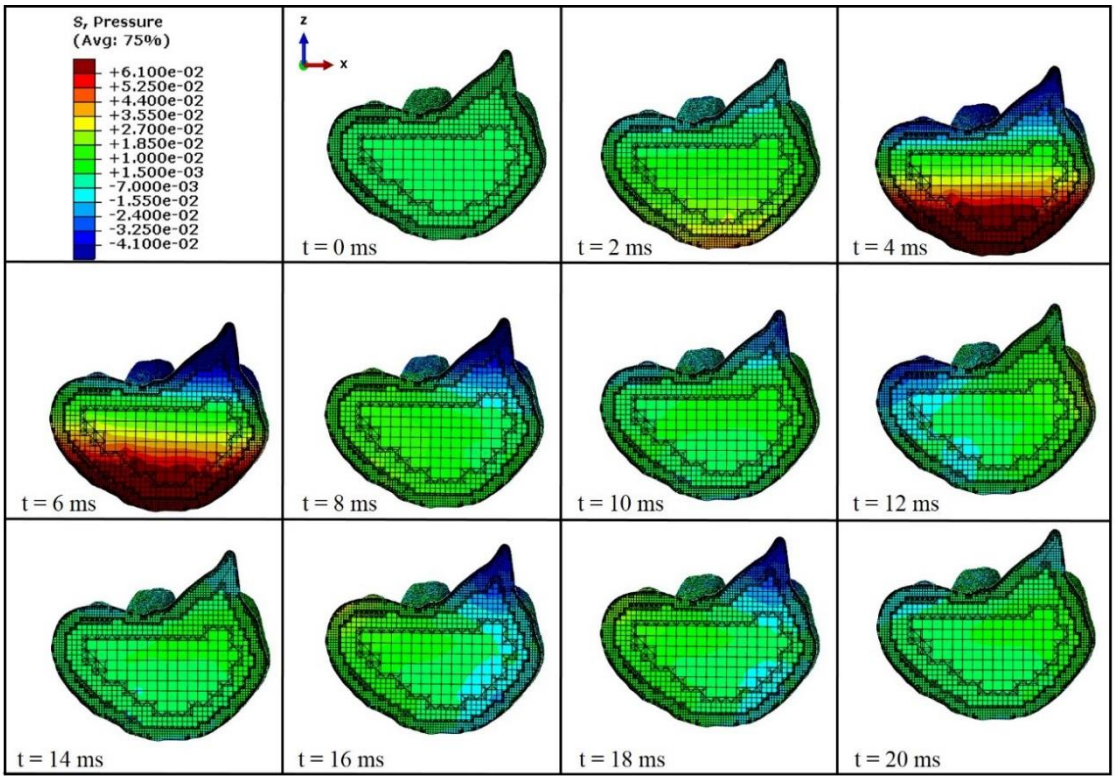

Figure 6.10 Intracranial pressure distribution of the human brain (mid-sagittal view) during a 3.46 m/s Top impact without the helmet.

Note: Pressure distributions are shown in MPa for two millisecond intervals during the twenty millisecond simulation.

Figure 6.11 and Figure 6.12 show pressure distributions of the NOCSAE headform and human head, respectively, during the 3.46 m/s Front Top impact simulation without the helmet. Again, greater pressures the human head (Figure 6.12) experienced

lower pressures as compared to the NOCSAE headform (Figure 6.11) simulation. In Figure 6.11, the effects of the boundary conditions and drop arm assembly mass can be observed with bending pressures at the headform collar (neck) location. From four milliseconds to eight milliseconds, high compressive pressures are observed at the rear (posterior) of the headform collar while high tensile pressures are observed at the front (anterior) of the collar. These pressures are indicative of bending forces in the anterior-posterior direction in which collar deformations would result in headform rotation about the (+) Y axis. Oscillations in these bending forces are observed after impact from simulation times of ten to twenty milliseconds. In Figure 6.12, a similar bending response is seen for the human head at this Front Top impact location. In contrast, the human head experienced more rotation by bending of the neck due to the geometric and material differences between it and the NOCSAE headform.

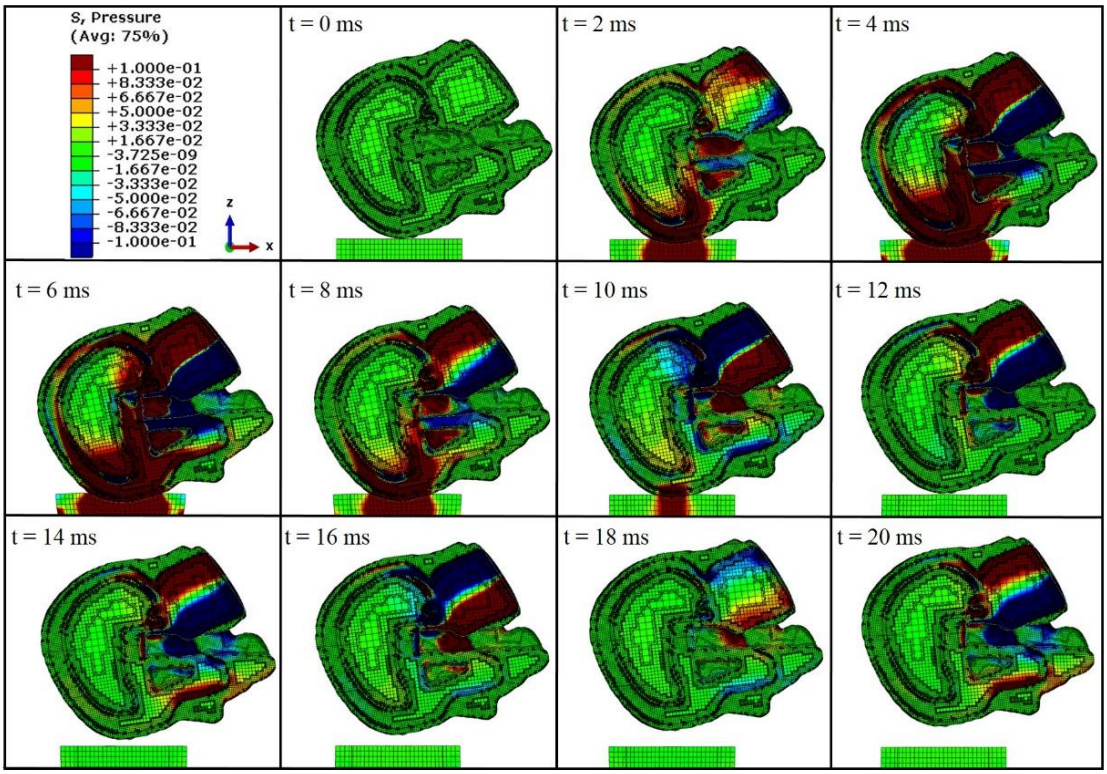

Figure 6.11 Validation simulation results showing pressure distribution of the NOCSAE headform model (mid-sagittal view) during a 3.46 m/s Front Top impact without the helmet.

Note: Pressure distributions are shown in MPa for two millisecond intervals during the twenty millisecond simulation.

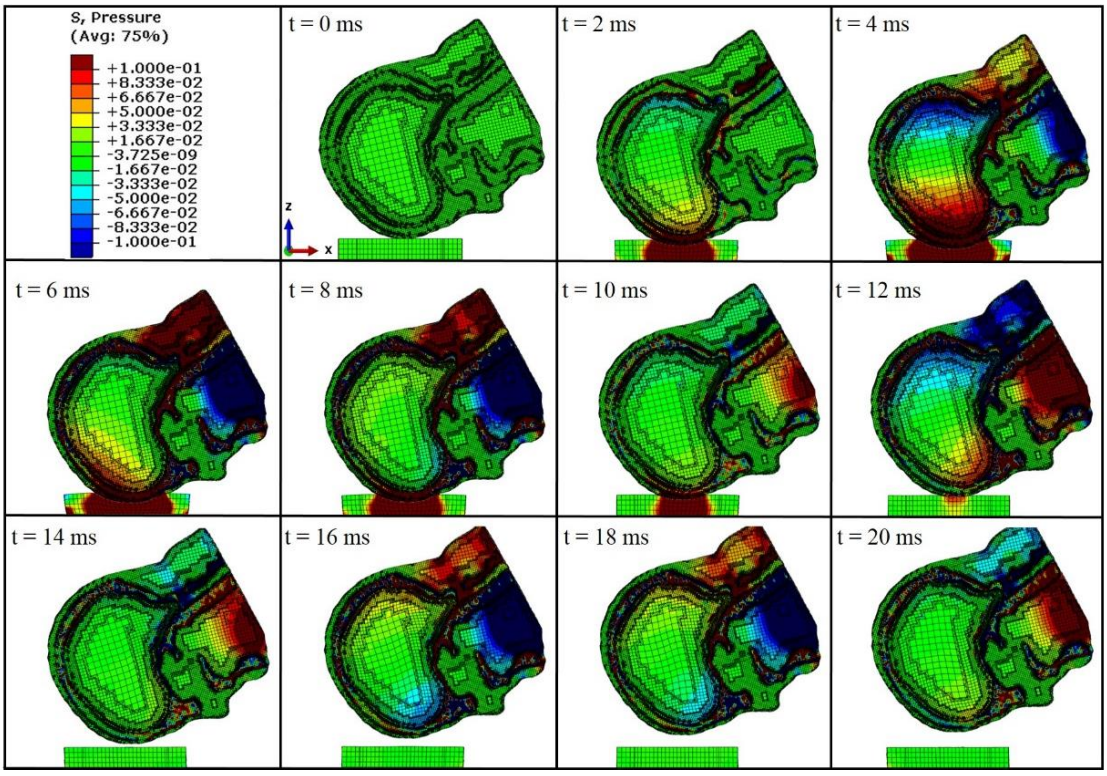

Figure 6.12 Validation simulation results showing pressure distribution of the human head (mid-sagittal view) during a 3.46 m/s Front Top impact without the helmet.

Note: Pressure distributions are shown in MPa for two millisecond intervals during the twenty millisecond simulation.

Figure 6.13 displays the intracranial pressure distributions of the human brain during the 3.46 m/s Front Top impact validation simulation without the helmet. At four milliseconds, the human brain experienced the greatest compressive pressures in the frontal lobe at the site of impact in the coup location. At this time, high tensile pressures are seen in the occipital lobe at the contre-coup location. After the peak CG acceleration pulse (after t = 8 ms), the tensile pressure propagated to the frontal lobe at t = 8 ms, then back to the occipital lobe at t = 12 ms with the greatest tensile pressures well after the initial impulse. A concussion-level event in the occipital lobe would result in blurry

vision or temporary loss of sight. Further oscillation of intracranial pressure occurs between fourteen and twenty milliseconds, with the highest shear stresses in the midbrain at eighteen milliseconds (t = 18 ms).

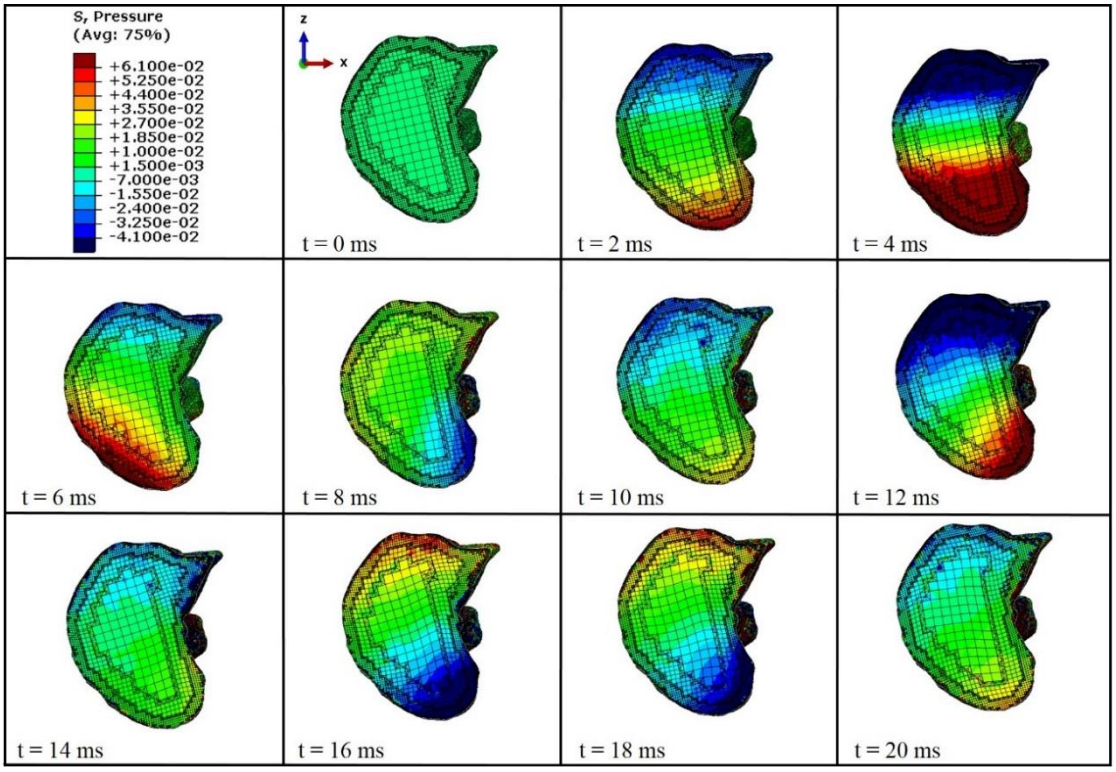

Figure 6.13 Intracranial pressure distribution of the human brain (mid-sagittal view) during a 3.46 m/s Front Top impact without the helmet.

Note: Pressure distributions are shown in MPa for two millisecond intervals during the twenty millisecond simulation.

Figure 6.14 depicts resultant acceleration-time history results for the "with helmet" cases for 3.46 m/s impacts. For the Top impact (Figure 6.14a), the acceleration trace for the headform simulation and human head simulation show a similar shape with magnitudes slightly higher than the headform experiment. The acceleration profiles for Front Top impacts (Figure 6.14b) shows a similar shape for the headform and human

head simulations with magnitudes close to that of the headform experiment. A double-peak shown in the acceleration trace of headform and human head simulations for both impact locations that was not exhibited in the headform experiments. This double-peak was only observed in 3.46 m/s helmeted simulations and is presumably due the phasic interaction between the liner and the helmet shell models at these low impact velocities.

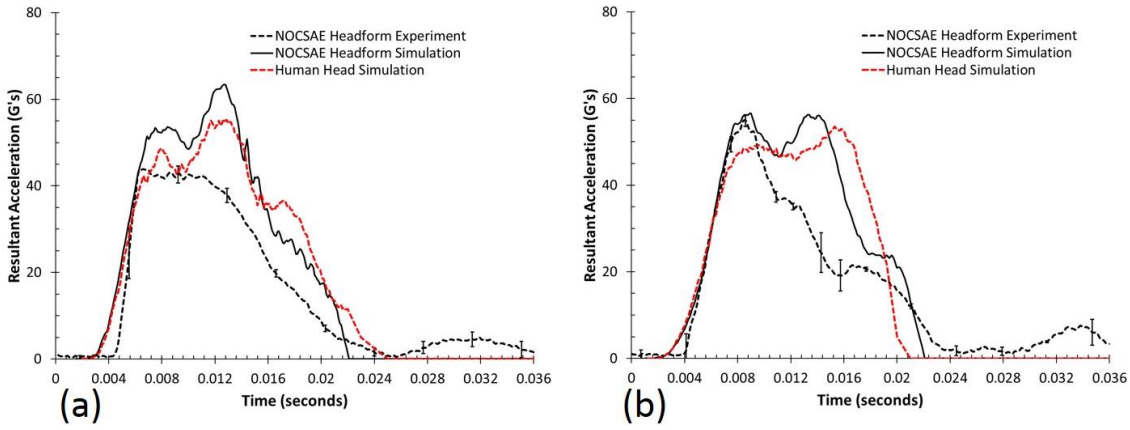

Figure 6.14 Experimental validation of helmeted NOCSAE headform model and comparison of helmeted human head model showing the CG resultant acceleration-time history with uncertainty of each at a 3.46 m/s Top impact (a) and Front Top impact (b).

Note: Time-shifted acceleration traces are shown for the NOCSAE headform and human head simulations.

Figure 6.15 displays resultant acceleration-time histories for the "with helmet" cases at a 5.46 m/s Top impact (Figure 6.15a) and Front Top impact (Figure 6.15b). In Figure 6.15a, the NOCSAE headform and human head show a similar trend in CG acceleration response. From Point 1 to Point 2, the acceleration-time profiles show a plateau region similar to the plateau region of the foam stress-strain behavior. Here, the difference between the human head and NOCSAE headform simulations is approximately 9 G's, where the difference between validation impacts is approximately 8

G's. From Point 2 to Point 3 in Figure 6.15a, the liner has compressed in to the densification region. In Figure 6.15b, the Front Top the helmeted NOCSAE headform experiment and the helmeted NOCSAE headform simulation show similar shapes of the acceleration-time histories. For this impact, the simulations shows a 22 G increase in peak acceleration as compared to the experiment. The acceleration trace of the human head response shows a different shape with a lower peak acceleration and increased impact duration as compared to the NOCSAE headform simulation.

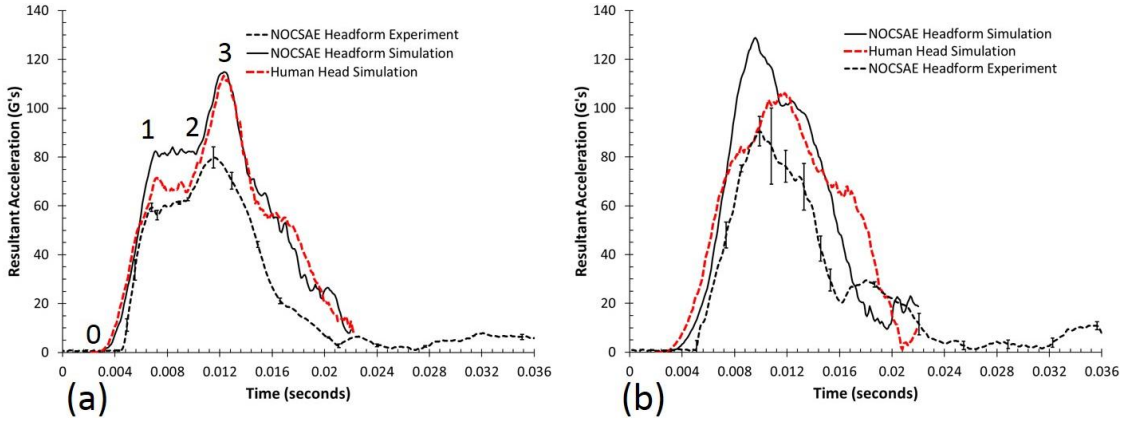

Figure 6.15 Acceleration-time history of helmeted NOCSAE headform model and helmeted human head model at a 5.46 m/s Top impact (a) and Front Top impact (b).

The uncertainty bands represent experimental uncertainty with a 95% confidence interval (n = 3). Note: Time-shifted acceleration traces are shown for the NOCSAE headform and human head simulations.

Figure 6.16 shows the pressure distributions of the human head with the helmet during the 5.46 m/s Top impact simulation. Here, the foam liner deformed with strain-levels in its densification region between the simulation times of four milliseconds to eight milliseconds (corresponding to Points 1 to 2 in Figure 6.15a). At the simulation time of ten milliseconds, the greatest compressive pressure occurs in the human head and

brain at the site of impact when the foam liner reached the maximum deformation (corresponding to point 3 Figure 6.15a). The greatest intracranial tensile pressure occurred in the brainstem and cerebellum at twelve milliseconds.

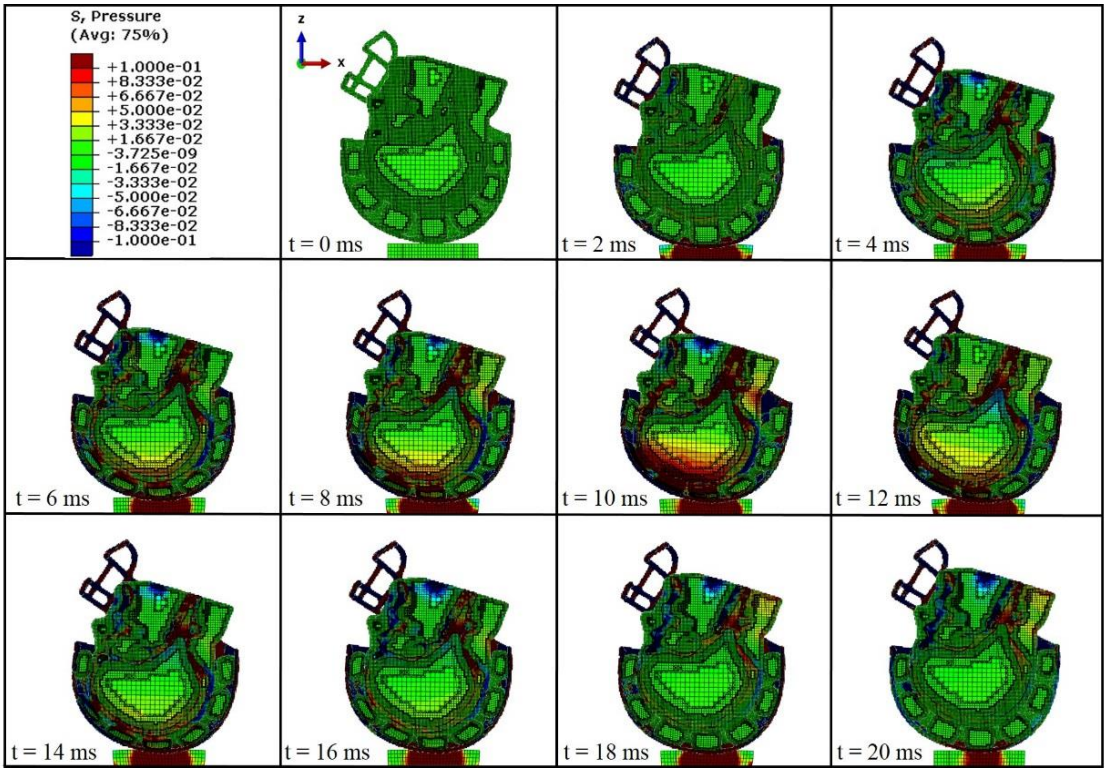

Figure 6.16 Pressure distribution of the human head with helmet (mid-sagittal view) during a 5.46 m/s Top impact.

Note: Pressure distributions are shown in MPa for two millisecond intervals during the twenty millisecond simulation.

In Figure 6.17, the pressure distributions of the human head with the helmet during the 5.46 m/s Front Top impact simulation are shown. A prolonged liner deformation, an earlier onset of liner densification, and more rotations can be observed for this impact location. This is due to the noncentricity of this particular impact location and the geometry of the impacted locations on the head and helmet shell. Due to

differences in the curvature of the human head and the helmet shell, there is less contact area for the Front Top impact location as compared to the Top impact location. As a result, less of the liner is in contact with the head to do work and an earlier densification occurs.

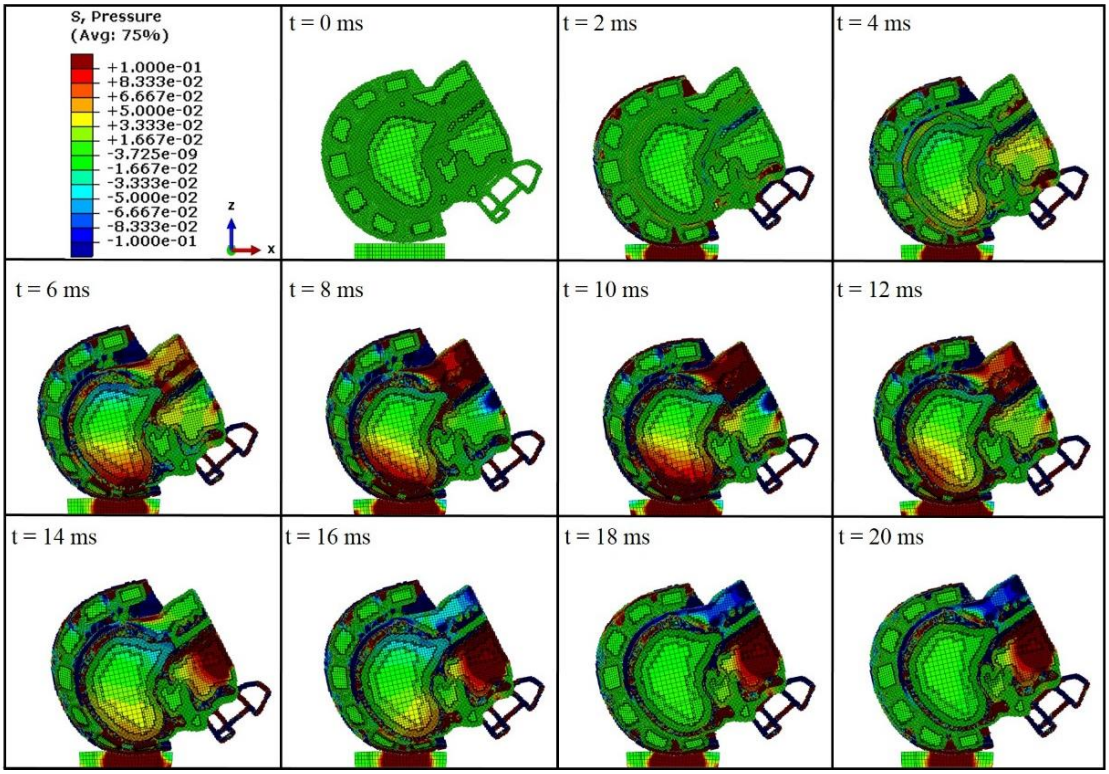

Figure 6.17 Pressure distribution of the human head with helmet (mid-sagittal view) during a 5.46 m/s Front Top impact.

Note: Pressure distributions are shown in MPa for two millisecond intervals during the twenty millisecond simulation.

Pressure-time histories of the human brain showed that compressive pressure at the coup location closely relates to acceleration at the head's center of gravity, as shown in Figure 6.18. Figure 6.18a displays the pressure-time response of the human head models with and without the helmet. When comparing the pressure-time response of

these models, the average coup pressure shows a similar trend to the measured CG acceleration response. When the human head is impacted without the helmet, the average impulsive force (and intracranial pressure) is higher and the impact duration is shorter compared to the helmeted human head impact at the same velocity. Figure 6.18b shows the greatest pressure versus resultant acceleration for at the coup and contre-coup locations. Here, the compressive pressures (at the coup site) and tensile pressures (at the contre-coup site) show a near-linear relationship when plotted against resultant acceleration. The slopes for the coup and contre-coup locations appear very similar for impacts with and without a helmet.

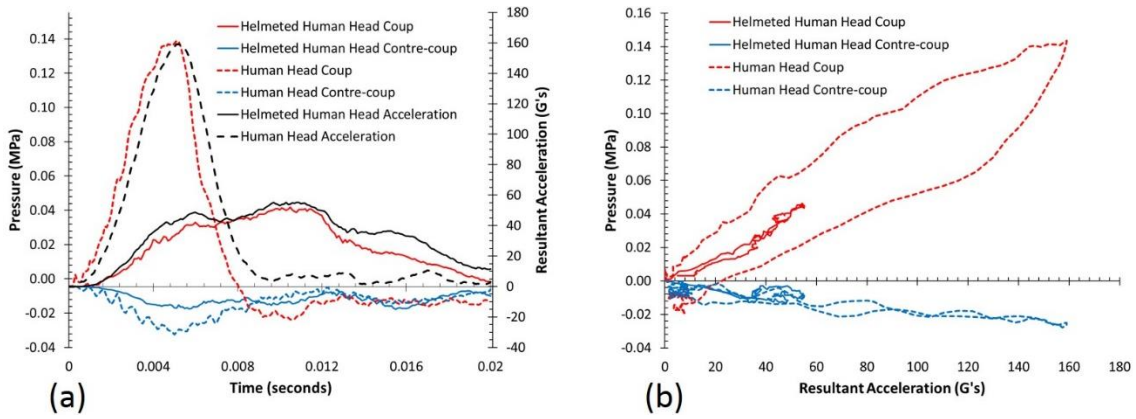

Figure 6.18 Pressure-time response at the Coup and Contre-coup locations of the human head model with and without a helmet at a 3.46 m/s Top impact.

Figure 6.18b reveals that the slope is -200 Pa/G level in the Top impact location for the tensile pressure. Since the tensile pressure is the most deleterious damage metric to the brain [see Prabhu *et al*., [91]], this relationship is important because most of the current damage metrics (SI and HIC) are based upon the acceleration and not the tensile

pressure. If one were to establish this relationship with the other impact locations, then there could be an assessment of the brain damage better than when just using the peak acceleration.

Figure 6.19 displays intracranial pressure-time histories of the human head model simulations with helmet. Here, coup and contre-coup pressures are shown at (a) a 5.46 m/s Top impact, (b) a 5.46 m/s Front Top impact, (c) a 3.46 m/s Top impact, and (d) a 3.46 m/s Front Top impact. For each impact velocity, the Front Top impact location was observed to have the highest compressive and tensile pressures. Note that the pressures are displayed on different scales for the 5.46 m/s and 3.46 m/s impacts.

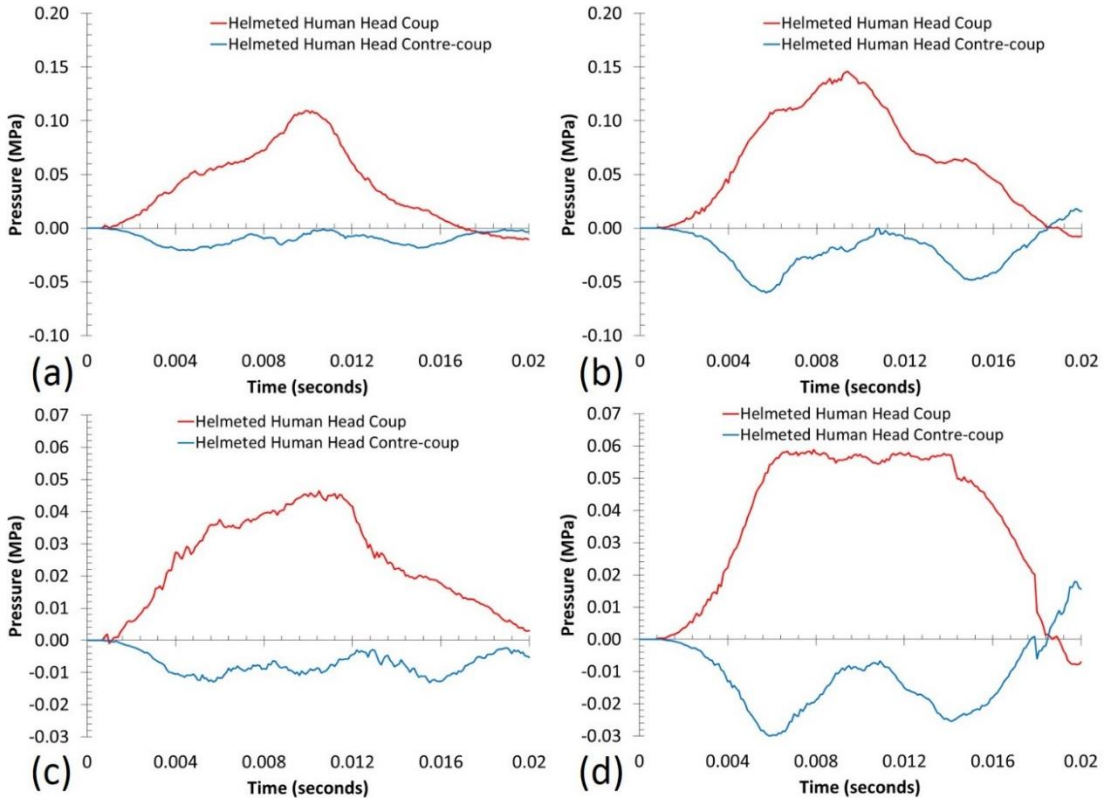

Figure 6.19 Pressure-time response at the Coup and Contre-coup locations of the helmeted human head model showing intracranial pressures at (a) a 5.46 m/s Top impact, (b) a 5.46 m/s Front Top impact, (c) a 3.46 m/s Top impact, and (d) a 3.46 m/s Front Top impact.

Note: The scales (a) and (b) are on higher pressure levels than (c) and (d).

Table 6.4 shows simulation and experimental validation results of global dynamic and intracranial mechanical responses. Here, the dynamic response variables of peak acceleration, HIC, and SI are shown comparatively for all of the simulations and experiments. These results are compared to the most conservative 50% concussion probabilities from Table 6.2, and the NOCSAE football helmet certification criteria. In Table 6.4, the values shown in bold font indicate if a result exceeds these thresholds. For Cases 2 and 4, the peak G, HIC, and SI, results for all 3.46 m/s helmeted impacts are below their limits and we will assume these as "non concussion cases" based upon the

50% concussion probabilities from Newman et al. [40, 106]. Notice here that values for shear stresses in the human brain exceed their theoretical concussion probability. Cases 1, 3, 5, and 6 would be considered "concussion cases" based their values of Peak G, HIC, and SI, exceeding the dynamic thresholds. NOCSAE certification limits were not exceeded in any helmeted impact. For the human brain, tensile pressure, and principal shear stress thresholds were not exceeded in all "concussion cases" while the principal strain thresholds were not exceeded in any event. In every "concussion case" the threshold for peak compressive pressure was exceeded along with the dynamic thresholds. Based on these results, peak coup pressure correlated best with peak acceleration, HIC, and SI limits for the human head. Additionally, the NOCSAE headform experiments and NOCSAE headform simulations were best correlated with peak acceleration then by HIC, and SI, respectively.

Table 6.4 Simulation and experimental validation results of the NOCSAE headform, human head with and without a helmet at a 3.46 m/s impact velocity and of the NOCSAE headform and human head with helmet at 5.46 m/s.

Case		Location	Velocity (m/s)	Peak G	HIC	SI	$P_{tens\ cc}$ (Kpa)	$P_{comp\ c}$ (KPa)	$\tau_{1\ max}$ (KPa)	$\varepsilon_{1\ max}$
1	Headform Experiment	Top	3.46	**171.23**	**783.17**	**873.29**	-	-	-	-
	Headform Simulation	Top	3.46	**167.33**	**484.14**	**535.17**	-5.75	**566.39**	**123.44**	0.010
	Human Head Simulation	Top	3.46	**159.11**	**455.37**	**498.77**	-31.79	**149.02**	**10.75**	0.033
2	Headform Experiment w/ Helmet	Top	3.46	43.85	91.89	100.58	-	-	-	-
	Headform Simulation w/ Helmet	Top	3.46	63.45	117.24	131.39	-14.14	**86.85**	**15.2**	0.009
	Human Head Simulation w/ Helmet	Top	3.46	55.18	100.07	108.65	-16.37	48.02	**9.02**	0.007
3	Headform Experiment	FT	3.46	**174.19**	**635.05**	**738.95**	-	-	-	-
	Headform Simulation	FT	3.46	**138.84**	**354.73**	**399.84**	**-57.37**	**354.57**	**46.35**	0.026
	Human Head Simulation	FT	3.46	**130.32**	**310.45**	**364.20**	**-95.89**	**210.74**	2.38	0.142
4	Headform Experiment w/ Helmet	FT	3.46	55.00	87.30	108.82	-	-	-	-
	Headform Simulation w/ Helmet	FT	3.46	56.59	110.40	122.04	-14.14	**89.88**	13.99	0.013
	Human Head Simulation w/ Helmet	FT	3.46	53.55	111.04	115.94	-33.4	62.85	**8.66**	0.010
5	Headform Experiment w/ Helmet	Top	5.46	**79.81**	**304.91**	**330.50**	-	-	-	-
	Headform Simulation w/ Helmet	Top	5.46	**114.89**	**406.43**	**455.47**	**-87.65**	**168.07**	**32.65**	0.020
	Human Head Simulation w/ Helmet	Top	5.46	**113.38**	**339.29**	**391.16**	-24.9	**109.35**	**8.99**	0.017
6	Headform Experiment w/ Helmet	FT	5.46	**90.54**	**328.80**	**378.60**	-	-	-	-
	Headform Simulation w/ Helmet	FT	5.46	**128.81**	**517.17**	**568.49**	24.66	**201.88**	**37.19**	0.028
	Human Head Simulation w/ Helmet	FT	5.46	**106.21**	**414.51**	**452.87**	**-60.11**	**145.92**	**9.49**	0.045
50% Concussion Probability [40, 86, 88]				77	239.8	291.2	-55	68.5	7.8	0.19
NOCSAE Certification (Pass/Fail) [109]		If V = 3.46 m/s				300				
		Else if V > 3.46 m/s				1200				

Note: Peak Acceleration, HIC, SI are shown comparatively to experimental tests. Mechanical response variables of the simulations were measured inside the brain.

In general, the headform model had a greater peak acceleration, HIC, SI values than the human head model due to inherent differences in material and geometry. This observation held true for all impact cases with and without the helmet. While both similar in size, the human head model was 1.17 Kg heavier than the NOCSAE headform model. Consequently, the difference in dynamic response was not due to any additional energy input. There was, however, a difference in loading path and material properties that explain differences in the dynamic response of the NOCSAE headform and the human head models. The NOCSAE headform generally provided a stiffer material response and absorbed less strain energy than the human head. As a result, greater stresses and smaller deformations in the headform led to greater accelerations and shorter impulse durations,

as compared to the human head. Consequentially, this difference in impulse duration would explain why HIC, and SI values were greater for the NOCSAE headform.

With respect to maximum intracranial stresses and strains, (Table 6.4) the NOCSAE headform was more conservative than the human head. The NOCSAE headform had great principal shear stresses, tensile pressures, and compressive pressures in its simulated brain as compared to the human brain. In contrast, the human brain experienced greater maximum principle strains. Since brain damage is a function of hydrostatic tensile stress and shear strain, the implications of these results need to be further examined to determine how closely the NOCSAE headform represents the human head. Compared to the simulated brain of the NOCSAE headform, the human brain is going to deform and have more strain energy. This difference in strain energy would inherently mean that the NOCSAE headform would have higher average impulsive forces (higher accelerations) compared to the human head.

Table 6.5 summarizes the results from the Top and Front Top impact locations showing the greatest tensile pressure locations and maximum shear stresses. Cocks and Ashby [46] showed that the tensile pressure clearly is the most deleterious stress state that nucleates and grows damage in a solid material. In fact, Cocks and Ashby [84] showed that the mechanical damage is a hyperbolic relationship with respect to the tensile pressure, which is extremely nonlinear. Also, the maximum shear strain is key when head rotations are prevalent. As such, a shearing mode can induce greater damage in certain boundary value problems. Hence, we show in Table 6.5 not only the greatest tensile pressures and their associated locations but the greatest shear strains as well.

Table 6.5 Human head simulation results with a helmet at 3.46 m/s and 5.46 m/s impact velocities showing; peak acceleration, maximum intracranial tensile pressures ($P_{tens\ max}$), with associated shear strains (γ_1), locations, and impulses, and maximum shear strains ($\gamma_{1\ max}$), with associated tensile pressures (P_{tens}), locations, and impulses.

Case		Impact Location	Velocity (m/s)	Peak G	$P_{tens\ max}$ (KPa)	I (N*s)	Location	γ_1	P_{tens} (KPa)	I (N*s)	Location	$\gamma_{1\ max}$
2	Human Head w/ Helmet	Top	3.46	55.18	-70.91	2.30 E-3	Brain Stem	0.008	-56.9	2.18 E-3	Brain Stem	0.012
4	Human Head w/ Helmet	FT	3.46	53.55	-61.2	2.5 E-4	Brain Stem	0.002	-8.5	6.9 E-4	Frontal Lobe	0.020
5	Human Head w/ Helmet	Top	5.46	113.38	-110.76	3.03 E-3	Brain Stem	0.003	-53.9	1.66 E-3	Brain Stem	0.033
6	Human Head w/ Helmet	FT	5.46	106.21	-92.13	3.00 E-3	Brain Stem	0.015	-9.0	7.21 E-3	Frontal Lobe	0.073

The most deleterious tensile pressures and their associated impulses occurred at the brain stem for both the Top and the Front Top impact locations. Also, the brain stem and frontal lobe exhibited the maximum shear strains. Clearly, these results do not bode well for the brain stem. Note also from Table 6.5 that these predicted damage locations arose at the two different velocities at impact as well.

6.4 Summary and Conclusions

This study investigated the dynamic response of the NOCSAE headform versus a human head during football helmet standard impact tests. The liner helmet and head FEA models were calibrated and experimentally validated. Model calibration was conducted with uncertainty using stress-strain data for each material. Validation of the helmet, liner, and headform were conducted by experimental NOCSAE drop tests. The results of the current study allow the following conclusions to be made:

1) The main conclusion here is that we were able to tie together the NOCSAE standard testing to the tensile pressure and shear strain within the brain. The tensile pressure and shear strain are the mechanical stress and strain states that affect mechanical damage the greatest. As an

example, the peak tensile pressure was quantified as a function of the peak acceleration of the CG for the Top impact location.

2) NOCSAE headform experiments and NOCSAE headform simulations were best correlated with peak acceleration.
3) For the human head, compressive pressure at the coup site correlated best with linear acceleration-based probabilistic thresholds for concussion (peak acceleration, HIC, and SI).
4) Based on the human brain response, a helmet test with a "concussive magnitude" impact can pass the NOCSAE certification requirements.
5) The helmeted NOCSAE headform and human head show a similar trend related to the CG acceleration behavior, which is dictated by the helmet liner. The acceleration-time profiles for 5.46 m/s Top impacts show a plateau and a densification region similar to the foam's stress-strain behavior.

CHAPTER VII

SUMMARY AND CONCLUSIONS

In this work, an optimal design process for a polymeric American football helmet liner for concussion prevention was created utilizing experiments and Finite Element Analysis. Structure-property relations were quantified for an open-cell polyurethane foam by employing microscopy methods, and varying strain rate experiments (monotonic and hysteric). These varying strain rate experiments were used to quantify the mechanical response of a baseline helmet liner, modern football helmet liners (Rawlings, Riddell, Schutt, and Xenith) and new possible polymeric foam liner materials. These materials were characterized at low strain rates (0.001-0.1/sec; Instron), intermediate strain rates (100-120/sec; NOCSAE drop tower) and high strain rates (500-1200/sec; Hopkinson bar). The shell-facemask response of modern football helmets was explored and advancements to helmet test standards were proposed. NOCSAE drop tests were used to perform experimental design optimization of novel football helmet liner. Finite Element Analysis of NOCSAE drop tests were conducted on a helmeted NOCSAE headform model and a helmeted human head model. These simulations were experimentally validated and created a linkage between helmet test standards, brain-injury metrics, and the mechanical response of the human brain. Based on results in this study, the following conclusions can be made:

1. The strain-rate dependence of an open-cell polyurethane foam was quantified at high strain-rates (1200-600/s) and low strain-rates (0.1-0.001/s).
2. The coupling between the helmet liner and the helmet shell may be as important as the liner properties themselves. A helmet liners local compressive response does not truly represent its global impact performance.
3. An optimal liner material should be designed to maximize deformation upon impact up to the densification region. This liner design criteria would maximize the amount of strain energy during impact while minimizing stress on the head.
4. The boundary value problem for a helmet hit is a load controlled not strain controlled engineering problem.
5. The foams local material system is distinguished by the global geometric effect and location in the helmet system.
6. The NOCSAE football helmet standard tests need to include the facemask
7. Based on Design of Experiments optimization the total length, followed area fraction, density, and encapsulate thickness were found to be the most contributing factors for the liner on peak acceleration, HIC, and SI values.
8. The optimum liner design for the baseline helmet is found to have a foam density of 84.5 kg/m3, a 1.5" pad thickness, a 75% area ratio, and a 25 mil encapsulate thickness.
9. We were able to tie together the NOCSAE standard testing to the tensile pressure and shear strain within the brain. The tensile pressure and shear strain are the mechanical stress and strain states that affect mechanical damage the greatest. As

an example, the peak tensile pressure was quantified as a function of the peak acceleration of the CG for the Top impact location.

10. NOCSAE headform experiments and NOCSAE headform Finite Element simulations were best correlated with peak acceleration.
11. Finite Element Analysis of the human head showed that compressive pressure at the coup site correlated best with linear acceleration-based probabilistic thresholds for concussion (peak acceleration, HIC, and SI).
12. Based on the human brain response in Finite Element simulations, a helmet test with a "concussive magnitude" impact can pass the NOCSAE certification requirements.
13. The helmeted NOCSAE headform and human head show a similar trend related to the CG acceleration behavior, which is dictated by the helmet liner. The acceleration-time profiles for 5.46 m/s Top impacts show a plateau and a densification region similar to the foam's stress-strain behavior.

CHAPTER VIII

FUTURE WORK

Future work of this research should include conducting Finite Element simulations of the NOCSAE headform and human head models at other impact locations, and additional boundary conditions. The effects of angular momentum and correlation between these two models should be investigated. There could be a relationship between the angular rotation and impact location if one were to move from top to front top to side. If this is true then the NOCSAE headform is really good at simulating linear acceleration response but not angular acceleration response.

In other finite element simulations, the use of the linear impactor test device and the Hybrid III dummy neck should be investigated and modeled at other impact scenarios. The linear impactor tests is becoming a frequent test method for helmet impacts and the impact response of the NOCSAE headform and Hybrid III neck under these conditions should be investigated and compared the human head via finite element analysis.

Future Finite Element simulations should be conducted on the human head model to investigate the effect of repeated impacts to the brain. These simulations should use the MSU TP1.1 Internal State Variable (ISV) brain model to investigate the short-term and long-term effects of multiple head impacts as a means of further understanding Chronic Traumatic Encephalopathy and Second Impact Syndrome. There are scenarios in football

where a player can experience numerous head impacts within a single play. These types of impacts could be dangerous because a second impact may occur before the helmet liner has had time to fully recover. Hence, the liner may be preloaded and a second impact prior to full liner recovery would result in lower energy absorption and higher head accelerations. Once developed, an ISV foam model should be used to examine the protective capability of helmet liners subject to multiple impacts within a few seconds of each other.

Further investigations should be conducted on maximum liner thickness with slightly larger helmet shells. Also, correlations between increases in angular acceleration, increase in torque on the neck and the tradeoffs of increased liner thickness should be investigated in the future using the linear impactor test device and hybrid III dummy neck.

Future studies should investigate the mechanical response of liner materials and helmet systems over a range of temperatures. In the present study, experiments of liner materials and helmet systems were conducted at 72°F ± 5°F (22.2°C ±2.8°C). Moreover, a unified NOCSAE football helmet and faceguard drop test procedure was proposed which would necessitate additional environmental conditioning procedures. Current NOCSAE helmet certification tests require high temperature impacts, in which helmets are conditioned at 100°F ± 5°F (49°C ± 2.6°C). For facemask certification, NOCSAE requires helmets to be conditioned in a high temperature environment at 120°F ± 5°F (49°C ± 2.6°C) and a low temperature environment at -20° ± 5°F (-29°C ± 2.6°C) prior to testing. Future studies should investigate a temperature range that should include the

required NOCSAE hot and cold conditioned environments for helmet and facemask testing.

Future studies should investigate the mechanical response of liner materials and helmet systems at additional strain-rates. For football helmet impacts, the liner component is subject to strain-rates of approximately 50/s to 200/s. This intermediate strain-rate range lies between the strain-rate ranges for the quasi-static Instron and high-rate Hopkinson bar test devices. Thus, the capability for strain-controlled mechanical testing of foam was limited at MSU by these test devices. In the present study, impact testing via material and NOCSAE drop towers was used to quantify performance characteristics of polymeric foam materials under these intermediate strain-rates. Future studies should use an intermediate strain-rate Hopkinson bars to quantify the mechanical response of polymeric foams under strain-controlled mechanical testing environments. These mechanical tests should be used to enhance the accuracy polymeric foam material models and Finite Element Simulations of helmet impacts.

Regardless of what injury metric is used for determining concussion-level events, the measurable global variables remain limited, namely linear and angular acceleration. In future work we are adding an additional parameter to globally measurable values, the wave. Measuring the shock wave speed in impact testing can be obtained from strategically placing audio devices around the headform. In FEA simulations the wave speed can be calculated. From which the modulus is calculated for each helmet component by using ultrasound along with compressive tests. We also will explore a model to explain neuronal injury secondary to concussion and provide an explanatory method for quantifying acceleration-deceleration forces and how they relate to the

magnitude of mTBI. Global linear and angular accelerations are obtained from accelerometers which have limited sampling rates in the range of 10- 20 kHz. During an impact the shock wave may reach speeds of x. Thus accelerometers would not be able to measure the initial damage determined from the stress wave. The damaging effects of the wave phenomena have been previously assumed to be negligible. The previous school of thought is that the brain can withstand very high G's if the duration is only for a few milliseconds. These assumptions were obtained from Dr. Voight Hodgeon's research at Wayne State University in 1960's. Thus we will investigate how the wave phenomena may affect concussion on a multi-scale level, and stating that the three parts of impact mechanics relating to injury metrics should include: 1) wave phenomena, which has previously been neglected for mTBI, 2). Momentum, and 3) Energy.

REFERENCES

1. Langlois, J.A., W. Rutland-Brown, and M.M. Wald. *The Epidemiology and Impact of Traumatic Brain Injury: A Brief Overview*. 2006. Lippincott Williams & Wilkins.

2. Broglio, S.P., et al., *Head impacts during high school football: a biomechanical assessment.* Journal of Athletic Training, 2009. **44**(4): p. 342-349.

3. Broglio, S.P., et al., *Estimation of head impact exposure in high school football: Implications for regulating contact practices.* American Journal of Sports Medicine, 2013. **41**(12): p. 2877-2884.

4. Costanza, A., et al., *Review: Contact sport-related chronic traumatic encephalopathy in the elderly: clinical expression and structural substrates.* Neuropathology & Applied Neurobiology, 2011. **37**(6): p. 570-584.

5. Prevention, C.f.D.C.a., *Nonfatal Traumatic Brain Injuries Related to Sports and Recreation Activities Among Persons Aged <=19 Years - United States, 2001-2009.* Morbidity and Mortality Weekly Report, 2011. **60**(39).

6. *History of the NFL football helmet*. 2012; Available from: http://www.nfl.com/news/story/0ap1000000095139/article/history-of-the-nfl-football-helmet.

7. Riddell. *Making History Since 1929*. 2012 30 May 2012]; Available from: http://www.riddell.com/innovation/history/.

8. Juan Menandro Gozales, R.M., *The Head Impact Telemetry System: The Future of Concussion Safety*. 2012, University of Pittsburgh: Swanson School of Engineering. p. 1-8.

9. Gurdjian, E.S., J.E. Webster, and H.R. Lissner, *Studies on skull fracture with particular reference to engineering factors.* The American Journal of Surgery, 1949. **78**(5): p. 736-742.

10. Gurdjian, E.S., J.E. Webster, and H.R. Lissner, *The mechanism of skull fracture.* Radiology, 1950. **54**(3): p. 313-339.

11. Newman, J.A., *The Evolution of Helmet Performance Standards*, in *Accidental Injury: Biomechanics and Prevention*, N. Yoganandan, Editor. 2015, Springer.

12. Bronzino, J.D., ed. *The Biomedical Engineering Handbook 1*. Second Edition ed. 2000, Springer.

13. Lissner, H.R., *Experimental Studies on the Relation Between Acceleration and Intracranial Pressure Changes in Man`*. Surgery, Gynecology and Obsterics, 1960. **III**: p. 329-338.

14. Gurdjian, E.S.e.a., *Concussion - Mechanism and Pathology.* Proceedings of the Seventh Strapp Car Crash Conference, 1963.

15. Patrick, L.M.e.a., *Survival by Design - Head Protection.* The Seventh Strapp Car Crash Conference, 1963.

16. Gadd, C.W., *Use of a weighted-impulse criterion for estimating injury hazard.* SAE Technical Papers, 1966.

17. NOCSAE, *Standard Performance Specification for Newly Maufactured Football Helmets.* 2011. **Paper No. 002-11m11a**.

18. Digges, K.H. *Injury Measurements and Criteria*. 1999. NATO.

19. Versace, J., *A review of the Severity Index.* SAE Technical Papers, 1971.

20. Reilly, P., Bullock, R. , *Head Injury Pathophysiology & Management*. Second Edition ed. 2005: CRC Press.

21. Hodgson, V.R. and L.M. Thomas, *Effect of long-duration impact on head.* SAE Technical Papers, 1972.

22. Henn, H.-W., *Crash Tests and the Head Injury Criterion.* Teaching Mathematics and its Applications 1998. **17**(4).

23. Greenwald, R.M., Gwin, Joseph T., Chu, Jeffery J., *Head Impact Severity Measures for Evaluating Mild Traumatic Brain Injury Risk Exposure.* Neurosurgery, 2008. **62**(4): p. 789-798.

24. Ommaya, A.K., A.E. Hirsch, and J.L. Martinez, *The role of whiplash in cerebral concussion.* SAE Technical Papers, 1966.

25. Ommaya, A.K. and T.A. Gennarelli, *Cerebral concussion and traumatic unconsciousness. Correlation of experimental and clinical observations on blunt head injuries.* Brain, 1974. **97**(4): p. 633-654.

26. Ommaya, A.K., S.D. Rockoff, and M. Baldwin, *EXPERIMENTAL CONCUSSION; A FIRST REPORT.* Journal of neurosurgery, 1964. **21**: p. 249-265.

27. Ommaya, A.K. and A.E. Hirsch, *Tolerances for cerebral concussion from head impact and whiplash in primates.* Journal of Biomechanics, 1971. **4**(1): p. 13-21.

28. Löwenhielm, P., *Mathematical simulation of gliding contusions.* Journal of Biomechanics, 1975. **8**(6): p. 351-356.

29. Hodgson, V.R., L.M. Thomas, and T.B. Khalil, *The role of impact location in reversible cerebral concussion.* SAE Technical Papers, 1983.

30. Delaney, J.S., A. Al-Kashmiri, and J.A. Correa, *Mechanisms of injury for concussions in university football, ice hockey, and soccer.* Clinical Journal of Sport Medicine, 2014. **24**(3): p. 233-237.

31. Mihalik, J.P., et al., *Measurement of head impacts in collegiate football players: An investigation of positional and event-type differences*.

32. *MEASUREMENT OF HEAD IMPACTS IN COLLEGIATE FOOTBALL PLAYERS: RELATIONSHIP BETWEEN HEAD IMPACT BIOMECHANICS AND ACUTE CLINICAL OUTCOME AFTER CONCUSSION.* Neurosurgery, 2007. **61**(6): p. 1244.

33. Broglio, S.P., et al., *Biomechanical Properties of Concussions in High School Football.* Medicine & Science in Sports & Exercise, 2010. **42**(11): p. 2064-2071.

34. Pellman, E.J., et al., *Concussion in professional football. Reconstruction of game impacts and injuries.* Neurosurgery, 2003. **53**(4): p. 799-814.

35. Pellman, E.J., et al., *Concussion in professional football: Location and direction of helmet impacts - Part 2*.

36. Rowson, S., et al., *Rotational head kinematics in football impacts: An injury risk function for concussion.* Annals of Biomedical Engineering, 2012. **40**(1): p. 1-13.

37. Peña, E., et al., *An anisotropic visco-hyperelastic model for ligaments at finite strains. Formulation and computational aspects.* International Journal of Solids and Structures, 2007. **44**(3–4): p. 760-778.

38. Rowson, S. and S.M. Duma, *Development of the STAR evaluation system for football helmets: Integrating player head impact exposure and risk of concussion.* Entwicklung des STAR-Messsystems zur Beurteilung der Schutzfunktion von Football-Helmen hinsichtlich Kopfverletzung und Gehirnerschütterung, 2011(8): p. 2130.

39. NOCSAE, *Statement from the National Operating Committee on Standards for Athletic Equipment Regarding 2013 Virginia Tech Star Rating System.* NOCSAE News, 2013.

40. Newman, J.A., N. Shewchenko, and E. Welbourne, *A proposed new biomechanical head injury assessment function - the maximum power index.* Stapp Car Crash Journal, 2000. **44**: p. 215-247.

41. Newman, J.A. *The Biomechanics of Head Trauma and Development of the Modern Helmet*. 2006.

42. Institute, B.S., *Crash Helmets*. 1869:1952.

43. Hodgson, V.R. and L.M. Thomas, *Comparison of head acceleration injury indices in cadaver skull fracture.* SAE Technical Papers, 1971.

44. Marjoux, D., et al., *Head injury prediction capability of the HIC, HIP, SIMon and ULP criteria.* Accident Analysis and Prevention, 2008. **40**(3): p. 1135-1148.

45. Gibson, L.J., Ashby, Michael F., *Cellular Solids Structure and Properties*. 2nd ed. Cambridge Solid State Science Series. 1997, Cambridge, United Kingdom: Cambridge University Press.

46. International, A., *Standard Test Methods for Flexible Cellular Materials- Slab, Bonded, and Molded Urethane Foams*. 2005.

47. Fitzgerald, C., I. Lyn, and N.J. Mills, *Airflow through polyurethane foams with near-circular cell-face holes.* Journal of Cellular Plastics, 2004. **40**(2): p. 89-110.

48. Mills, N., *Polymer Foams Handbook*. Polymer Foams Handbook. 2007.

49. Systems, D., *Summary Guide Liquid SunMate FIPS Foam-In-Place Seating*. 2001.

50. Systems, D., *SunMate Cushion Material Data Sheet*. 2008.

51. Systems, D., *Material Safety Data Sheet for SunMate Cushion Material.* 2012.

52. Antonio Greco, F.L. *The Influence of the Stress Relaxation and Creep Recovery Times on the Viscoelastic Properties of Open Cell Foams*. POLYMER ENGINEERING AND SCIENCE, 2009. DOI: 10.1002/pen.21345.

53. Zhu, H.X., N.J. Mills, and J.F. Knott, *Analysis of the high strain compression of open-cell foams.* Journal of the Mechanics and Physics of Solids, 1997. **45**(11-12): p. 1875-1904.

54. Wismans, J.G., van Dommelen, J.A. , *Characterization of polymeric foams.* Eindhoven University of Technology, 2009. **Mechanics of Materials**(July 2009).

55. Widdle Jr., R.D., Bajaj, A.K., Davies, P., *Measurement of the Poisson's ratio of flexible polyurethane foam and its influence on a uniaxial compression model.* International Journal of Engineering Science, 2007. **46**(2008): p. 31-49.

56. Zhu, H.X., N.J. Mills, and J.F. Knott, *Analysis of the high strain compression of open-cell foams.* Journal of the Mechanics and Physics of Solids, 1997. **45**(11–12): p. 1875-1904.

57. Viano, D.C., C. Withnall, and D. Halstead, *Impact performance of modern football helmets.* Annals of Biomedical Engineering, 2012. **40**(1): p. 160-174.

58. Bartsch, A., et al., *Impact test comparisons of 20th and 21st century American football helmets: Laboratory investigation.* Journal of neurosurgery, 2012. **116**(1): p. 222-233.

59. King, A.I., et al. *Is Head Injury Caused by Linear or Angular Acceleration?* 2003. International Research Council on the Biomechanics of Impact.

60. Rush, G.A., *Comparison of Shell-Facemask Responses in American Football Helmets during NOCSAE Drop Tests* Sports Engineering, submitted 2015.

61. Rush, G.A., *Personal Protective Equipment Liner*. 2015: United States.

62. Taguchi, G., and Y. Wu, *Introduction to Off-Line Quality Control.* Japan Quality Control Organization, Nagoya, Japan., 1980.

63. Taguchi, G., *Introduction to Quality Engineering.* Asian Productivity Organization, 1986. **UNIPUB, White Plains, NY.**

64. Montgomery, D.C., *Introduction to Statistical Quality Control*. Wiley.

65. Byrne, D.M., and S. Taguchi, *The Taguchi Approach to Robust Parameter Design.* 40th Annual Quality Progress Transactions 1987(December): p. 19-26.

66. NOCSAE, *NOCSEA Overview.* 2013.

67. Gwin, J.T., et al., *An investigation of the NOCSAE linear impactor test method based on in vivo measures of head impact acceleration in American football.* Journal of Biomechanical Engineering, 2010. **132**(1).

68. NOCSAE, *NOCSAE Standards and Process.* 2013.

69. NOCSAE, *Standard Method of Impact Test and Performance Requirements for Football Faceguards.* 2011. **Paper No. ND087-11M11**.

70. NOCSAE, *Standard Performance Specification for Newly Manufactured Lacrosse Helmets with Faceguard.* 2012. **NOCSAE DOC (ND) 041-11m12**.

71. Hodgson, V.R., L.M. Thomas, and P. Prasad, *Testing the validity and limitations of the severity index.* SAE Technical Papers, 1970.

72. Rawlings, *Football Catalog.* 2012.

73. Football, R. *NRG Quantum Plus Helmet*. 2014; Available from: http://www.rawlingsfootball.com/products/helmets/quantumplus.

74. Riddell. *Riddell 360 Helmet*. 2013; Available from: http://team.riddell.com/shop-riddell/helmet/riddell-360-helmet/.

75. Schutt, *2012 Football Catalog*. 2013. p. 8-11.

76. Schutt, *ION 4D Faceguard Attachment Instructions.* 2009.

77. Xenith, *X2 Technology Xenith Adaptive Head Protection*. 2011.

78. Xenith, *X2 Player's Manual.* 2011.

79. Schutt, *Schutt Helmet Fitting Instructions.* 2009.

80. Rawlings, *NRG Quantum Fit Guide.*

81. Riddell, *360 Fitting Instructions and Helmet Care.*

82. Schmitt, K.U., et al., *Trauma biomechanics an introduction to injury biomechanics*. Trauma Biomechanics: An Introduction to Injury Biomechanics. 2014: Springer-Verlag Berlin Heidelberg. 1-243.

83. Yanagida, Y., S. Fujiwara, and Y. Mizoi, *Differences in the intracranial pressure caused by a 'blow' and/or a 'fall' - An experimental study using physical models of the head and neck.* Forensic Science International, 1989. **41**(1-2): p. 135-145.

84. Cocks, A.C.F. and M.F. Ashby, *Creep Fracture by Void Growth*, in *Creep in Structures: 3rd Symposium, Leicester, UK, September 8–12, 1980*, A.R.S. Ponter and D.R. Hayhurst, Editors. 1981, Springer Berlin Heidelberg: Berlin, Heidelberg. p. 368-387.

85. Ahmadisoleymani, S.S. and J. Yang, *American Football Helmet for Preventing Concussion, a Literature Review.* Procedia Manufacturing, 2015. **3**: p. 3796-3803.

86. Zhang, L., K.H. Yang, and A.I. King, *A Proposed Injury Threshold for Mild Traumatic Brain Injury.* Journal of Biomechanical Engineering, 2004. **126**(2): p. 226-236.

87. Zhang, L., King, A.I., Viano, D.C., *A New Biomechanical Predictor For Mild Traumatic Brain Injury- A Preliminary Finding*, in *Summer Bioengineering Conference* 2003: Key Biscayne, Florida. p. 0137-0138.

88. Kleiven, S., *Predictors for traumatic brain injuries evaluated through accident reconstructions.* Stapp car crash journal, 2007. **51**: p. 81-114.

89. Viano, D.C., et al., *Concussion in professional football: Brain responses by finite element analysis: Part 9.* Neurosurgery, 2005. **57**(5): p. 891-915.

90. Prabhu, R., et al., *Coupled experiment/finite element analysis on the mechanical response of porcine brain under high strain rates.* Journal of the Mechanical Behavior of Biomedical Materials, 2011. **4**(7): p. 1067-1080.

91. Prabhu, R., *TRAUMATIC BRAIN INJURY: MODELING AND SIMULATION OF THE BRAIN AT LARGE DEFORMATION*, in *Department of Mechanical Engineering*. 2011, Mississippi State University: Mississippi State, Mississippi.

92. NOCSAE, *Laboratory Procedural Guide for Certifiying Newly Manufactured Football Helmets.* 2014. **Paper No. 003-96m14**.

93. NOCSAE, *Standard Test Method and Equipment used in Evaluating the Performance Characteristics of Protective Headgear/Equipment.* 2011. **Paper No. 001-11m13**.

94. Ganpule, S., Alai, A., Plougonven, E., *Mechanics of blast loading on the head models in the study of traumatic brain injury using experimental and computational approaches.* Biomech Model Mechanobiol 2011. **2013**.

95. Boruah, S., Henderson, Kyvory, Subit, Damien, , *Response of Human Skull Bone to Dynamic Compressive Loading.* IRCOBI Conference, 2013. **2013**.

96. Bayraktar, H.H., Morgan, Elise F., Niebur, Glen L. , *Comparison of the elastic and yield properties of human femoral trabecular and cortical bone tissue.* Journal of Biomechanics 2004. **37**.

97. Mao, H., Zhang, Liying, Jiang, Binhui, *Development of a Finite Element Human Head Model Partially Validated with Thirty Five Exerimental Cases.* Journal of Biomechanical Engineering 2013. **135**(NOVEMBER 2013).

98. *Overview of materials for Thermoset Polyurethane, Elastomer, Unreinforced*. 2015; Available from: http://www.matweb.com/.

99. *Overview of materials for High Density Polyethylene (HDPE), Injection Molded*. 2015; Available from: http://www.matweb.com/.

100. *Aluminum 6061-T6; 6061-T651*. 2015; Available from: http://www.matweb.com/.

101. *Magnesium AZ61A-F, Extruded Solid Shapes*. 2015; Available from: http://www.matweb.com/.

102. Medicine, R.S. *The Rush Helmet*. 2016; Available from: http://www.rushsportsmedicine.com/index.cfm/research-development/the-rush-helmet/.

103. Caravia, L., et al., *10th International Conference on Wear of MaterialsFriction of hydrogel and polyurethane elastic layers when sliding against each other under a mixed lubrication regime.* Wear, 1995. **181**: p. 236-240.

104. Ikeuchi, K., et al., *Water lubrication of polyurethane grafted with dimethylacrylamide for medical use.* Wear, 1993. **161**(1): p. 179-185.

105. *DATA SHEET*, in *Pudgee Cushion Material*. 2011, Dynamic Systems, Inc.

106. Newman, J., et al., *A new biomechanical assessment of mild traumatic brain injury. Part 2. Results and conclusions.* Proceedings of International Research Conference on the Biomechanics of Impacts, 2000: p. 223-233.

107. Broglio, S.P., et al., *Head Impacts During High School Football: A Biomechanical Assessment.* Journal of Athletic Training (National Athletic Trainers' Association), 2009. **44**(4): p. 342-349.

108. Becker, E.B., *Guided Fall Impact Test Devices Monorail and Twin-Wire Comparison.* Snell Memorial Foundation, 1997.

109. NOCSAE, *Standard Performance Specification for Newly Maufactured Football Helmets*. 2013.

APPENDIX A

SUPPLEMENTARY RESULTS

Table A.1 shows results of preliminary material impact testing on 41 candidate liner materials by a twin-wire drop tower equipped with a NOCSAE headform (Table A.1). A 6”x6” sheet of liner material was placed on the 3” MEP pad and impacted three consecutive times (90 ± 15 seconds) at 4.88 m/s with a size medium NOCSAE headform at the top impact location. Peak resultant acceleration was recorded and a difference in G’s was calculated from each liner experiment by subtracting it’s mean from that of the calibration impacts of the headform only (without foam). This “G difference” was then normalized by the candidate liner material thickness. While a 1 inch liner was desired, we were not able to achieve that exact size in all of the specimens, hence a linear normalization was achieved by dividing the difference in G’s by the thickness. Rankings were performed with this difference in average acceleration and was used to limit the candidate foams.

Table A.1 Preliminary impact test results of candidate liner materials showing: average peak resultant acceleration (G's) with standard deviations, material thickness (t), the difference in G's by experimental minus calibration results (G Diff), the difference in G's normalized by thickness and the rankings candidate materials.

Mfg.	Label	Cell Type	Matl.	Peak G's		t	G Diff	Norm G Diff	Rank
				Avg	SD	(in)	(exp-cal)	(exp-cal)/t	
SunMate	SM Firm	Open	PU	99.19	1.46	1.00	64.66	64.66	1
SunMate	SM Med-Firm	Open	PU	107.59	0.54	1.00	56.25	56.25	6
SunMate	SM Med	Open	PU	116.32	0.68	1.00	47.52	47.52	10
SunMate	SM Soft	Open	PU	132.80	2.02	1.00	31.05	31.05	22
SunMate	SM Extra-Soft	Open	PU	135.67	0.62	1.00	28.17	28.17	27
SunMate	SM Comfort	Open	PU	144.58	1.22	1.00	19.26	19.26	32
SunMate	SM Pudgee	Gel Foam	PU	151.19	1.02	0.50	12.65	25.30	28
SunMate	SM T50E	Open	PU	99.25	1.81	1.00	64.59	64.59	2
Bergad	BG 5062	Open	PU	120.43	2.03	1.00	43.41	43.41	13
Bergad	BG 5061	Open	PU	122.45	0.47	1.00	41.40	41.40	15
Bergad	BG 6032	Open	PU	117.95	0.75	1.00	45.90	45.90	11
Bergad	BG 6077B	Open	PU	135.58	1.29	1.00	28.27	28.27	26
Bergad	BG 5058BG	Open	PU	144.20	0.54	1.00	19.65	19.65	31
Bergad	BG 6083F	Open	PU	139.50	1.29	1.00	24.34	24.34	30
Bergad	BG 6000	Open	PU	138.83	1.24	1.00	25.01	25.01	29
Bergad	BG 4538	Open	PU	152.63	0.41	1.00	11.22	11.22	35
Bergad	BG 5068B	Open	PU	87.09	0.62	1.94	76.75	39.66	16
Bergad	BG 2512	Open	PU	156.65	0.23	1.00	7.19	7.19	37
Bergad	BG 5060	Open	PU	135.10	1.24	1.00	28.75	28.75	25
Bergad	BG 6060	Open	PU	119.38	1.70	1.00	44.46	44.46	12
Bergad	BG 6001	Open	PU	131.84	0.76	1.00	32.01	32.01	19
Bergad	BG 6078	Open	PU	132.22	0.85	1.00	31.62	31.62	20
Bergad	BG 6078	Open	PU	132.22	0.85	1.00	31.62	31.62	20
Bergad	BG 6030	Open	PU	96.48	1.56	1.20	67.36	56.14	7
SKYDEX	SKY 1	Eng Cmb	TPU	106.54	4.81	1.12	57.30	51.16	9
SKYDEX	SKY 2	Eng Cmb	TPU	92.75	1.99	1.12	71.10	63.48	4
SKYDEX	SKY 3	Eng Cmb	TPU	97.25	3.25	1.12	66.60	59.46	5
SKYDEX	SKY 4	Eng Cmb	TPU	91.98	2.48	1.12	71.86	64.16	3
Poron	XRD	Open	PU	125.45	0.14	0.72	38.39	53.32	8
-	5.5 bead foam	Closed	PP	139.82	8.33	0.57	24.02	41.81	14
-	3.2 bead foam	Closed	PP	157.72	0.14	1.00	6.13	6.13	38
DEO	PE MAT 4.0	Closed	PE	134.94	1.92	0.94	28.90	30.61	23
EN MURRAY	L-380	Closed	EVA	127.86	3.19	1.01	35.98	35.63	18
EN MURRAY	L-300	Closed	EVA	126.18	1.47	1.00	37.66	37.66	17
EN MURRAY	ultrafire	Closed	EVA	153.32	1.43	1.00	10.52	10.52	36
PAC FOAM	4# EVA CLP	Closed	EVA	134.66	1.22	1.00	29.19	29.19	24
-	P165-65	Closed	PP	158.57	2.01	1.00	5.27	5.27	39
-	SCH180-GOE	Open	-	151.02	1.24	1.00	12.82	12.82	34
-	F155-050E	Open	-	159.83	1.43	0.98	4.02	4.09	41
-	H50013N	Open	-	149.77	0.82	1.00	14.07	14.07	33
-	P170-070N	Open	-	159.25	1.43	1.00	4.59	4.59	40

Rankings are presented in descending order as the material with a rank of 1 shows the greatest normalized difference in G's.

A total of 384 drop tests were recorded considering four helmets with two configurations ("with facemasks" and "without facemasks"), two impact velocities and

eight impact locations. The Rawlings Quantum Plus, Riddell 360, Schutt Ion 4D and, Xenith X2 helmets each showed varying responses with respect to change to impact location and impact velocity when the facemask was attached. ANOVA F-tests diagnosed significant four-factor interactions ($p < 0.05$) between class variables (Table A1). The largest of these variations was due to change in impact velocity followed by impact location, helmet type, and facemask configuration, respectively. Significant differences were also observed across the dependent variables of HIC, SI, and acceleration (G's). The model for ANOVA was then compartmentalized in three groups; 1) helmet type, 2) impact location, 3) helmet type and impact location. A comparison between facemask configurations was then allowed for each of these groups at each impact velocity using relative standard errors and relative mean differences. The relative mean differences in HIC, SI, and acceleration (G's) for each helmet type and each impact location (Table A2) revealed significant influence between facemask configuration results for 5.46 and 4.88 meters per second impact velocities. Table A2 shows that the facemask responses were helmet dependent, and varied across impact location and impact velocity. Significant influence was also observed to vary between HIC, SI, and acceleration (G's).

Table A.2 Analysis of Variance table showing significant interactions between impact velocity (VEL), impact location (LOC), helmet type (TYPE), and facemask configuration (CONFIG) class variables.

		Dependent Variable											
		HIC				SI				Acceleration (G's)			
Source	DF	Type III SS	Mean Square	F Value	*P* Value	Type III SS	Mean Square	F Value	*P* Value	Type III SS	Mean Square	F Value	*P* Value
VEL	1	1253505	1253505	2680	<.0001	1736043	1736043	2412.5	<.0001	36537.9	36537.9	1159.9	<.0001
LOC	7	1534477	219211	468.7	<.0001	1906800	272400	378.5	<.0001	24637.6	3519.7	111.7	<.0001
VEL*LOC	7	22334.9	3190.7	6.8	<.0001	23890.8	3413	4.7	<.0001	2492.8	356.1	11.3	<.0001
TYPE	3	221312	73770.7	157.7	<.0001	277696.1	92565.4	128.6	<.0001	9604.7	3201.6	101.6	<.0001
VEL*TYPE	3	31511	10503.7	22.5	<.0001	38963.1	12987.7	18.1	<.0001	803.1	267.7	8.5	<.0001
LOC*TYPE	21	355799.1	16942.8	36.2	<.0001	447212.4	21295.8	29.6	<.0001	13940.4	663.8	21.1	<.0001
VEL*LOC*TYPE	21	52308	2490.9	5.3	<.0001	73754.8	3512.1	4.9	<.0001	2655.2	126.4	4	<.0001
CONFIG	1	12022.8	12022.8	25.7	<.0001	28152.8	28152.8	39.1	<.0001	127.6	127.6	4.1	0.0452
VEL*CONFIG	1	6411.8	6411.8	13.7	0.0003	10665	10665	14.8	0.0001	4.5	4.5	0.1	0.7046
LOC*CONFIG	7	94357.8	13479.7	28.8	<.0001	139170.1	19881.4	27.6	<.0001	6034.8	862.1	27.4	<.0001
VEL*LOC*CONFIG	7	26365.1	3766.4	8.1	<.0001	58575.7	8368	11.6	<.0001	990.7	141.5	4.5	<.0001
TYPE*CONFIG	3	4503.5	1501.2	3.2	0.0236	2902.4	967.5	1.3	0.2604	450	150	4.8	0.003
VEL*TYPE*CONFIG	3	10872.6	3624.2	7.8	<.0001	14891.2	4963.7	6.9	0.0002	460.8	153.6	4.9	0.0026
LOC*TYPE*CONFIG	21	106955.3	5093.1	10.9	<.0001	146081.2	6956.2	9.7	<.0001	7997.4	380.8	12.1	<.0001
VEL*LOC*TYPE*CONFIG	21	53784	2561.1	5.5	<.0001	68732.1	3273	4.6	<.0001	1614.9	76.9	2.4	0.0006

Significant differences are also seen across the dependent variables of HIC, SI, and acceleration (G's). Degrees of freedom (DF) are shown for each source of the general linear model using Type III sums of squares F tests.

Table A.3 shows significant differences ($\alpha = 0.05$) in acceleration, HIC, and SI of the source parameters subjected to NOCSAE drop tests during liner design optimization. Total length followed by area ratio, density, and diameter were the most significant of all parameters tested having the lowest P values, highest F values, and largest differences between means. ANOVA shows that the number of foam layers, encapsulate thickness, and the gas inside the foam were not significantly contributing factors compared to the variance of the other factors. The gas inside the foam, whether it was air or helium, made little contribution in peak G, HIC, or SI as compared to the other factors.

Table A.3 Statistical analysis of experimental NOCSAE drop test results showing mean differences (Diff) with Standard Deviations, Standard Error, F values, and P values for each parameter source with degrees of freedom (DF) for Acceleration, HIC, and SI dependent variables.

Source	DF	Dependent Variable														
		Acceleration (G's)					HIC					SI				
		Diff (1-2)	Std Dev	Std Err	F Value	*P* Value	Diff (1-2)	Std Dev	Std Err	F Value	*P* Value	Diff (1-2)	Std Dev	Std Err	F Value	*P* Value
Gas	41	-2.15	29.78	6.50	1.23	0.5129	12.66	141.10	30.78	1.59	0.1395	8.46	178.40	38.92	1.45	0.2394
Total Length	41	50.19	15.58	3.40	5.34	<.0001	251.30	61.39	13.40	22.03	<.0001	306.70	87.95	19.19	15.23	<.0001
Area Ratio	41	-20.99	27.84	6.07	2.17	0.0146	-54.09	138.50	30.23	2.37	0.0069	-97.83	171.40	37.40	2.62	0.0027
Diameter	41	-6.30	29.63	6.46	2.48	0.0044	-30.82	140.30	30.62	2.16	0.0153	-41.71	177.20	38.66	2.49	0.0043
Impacted Location	41	5.45	29.67	6.47	2.11	0.0187	35.63	140.00	30.56	2.00	0.0293	41.84	177.10	38.66	2.17	0.0150
TPU Thickness	41	-9.86	29.38	6.41	1.01	0.9763	-29.92	140.40	30.64	1.49	0.2074	-44.04	177.00	38.63	1.32	0.3716
# of Layers	41	-5.15	29.68	6.48	1.61	0.1310	-32.66	140.20	30.60	1.80	0.0633	-43.14	177.10	38.64	1.87	0.0485
1 Layer Density	20	16.71	24.87	7.68	2.18	0.0370	80.70	112.60	34.76	1.39	0.4636	106.00	139.50	43.05	2.08	0.1092
2 Density 1	20	2.15	33.36	10.30	2.70	0.0312	-10.38	160.90	49.65	3.09	0.0152	6.18	204.60	63.13	3.04	0.0164
Density 2	20	5.60	33.26	10.26	4.39	0.0017	14.71	160.80	49.63	3.32	0.0100	20.80	204.30	63.06	4.18	0.0024

The shaded values shown are determined to be statistically significant ($\alpha = 0.05$).

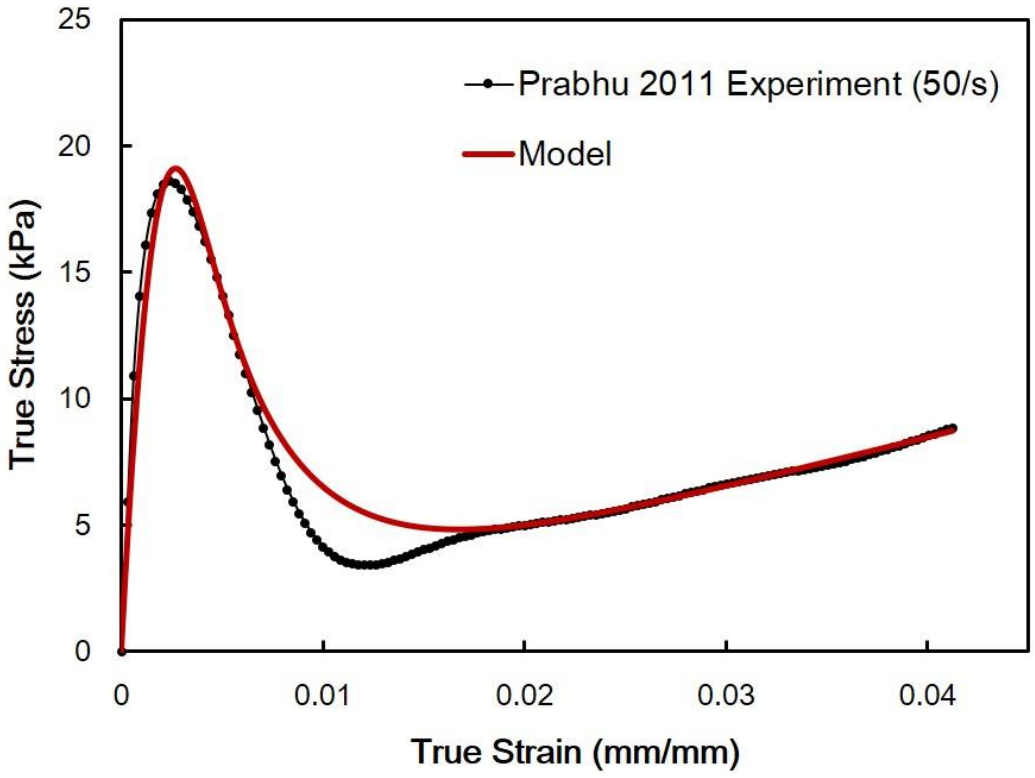

Figure A.1 Comparison of the true stress-strain behavior of brain tissue experiments from Prabhu et al. 2011 and the brain material model calibration.

Note: Experiments were conducted on porcine brain tissue by Prabhu *et al*. [90, 91], using a Split-Hopkinson Pressure Bar (SPHB). The current study employed a mechano-physiological constitutive model material model (MSU TP 1.1) for Finite Element Analysis of the brain. The MSU TP 1.1 material model was calibrated to SPHB compression experiments at a strain-rate of 50 per second.